Three-Dimensional Integrated Photonics in Transparent Substrates Enabled by Femtosecond Laser Fabrication

by

Mohan Wang

B.S., University of Pittsburgh, 2014

Submitted to the Graduate Faculty of the

Swanson School of Engineering in partial fulfillment

of the requirements for the degree of

Doctor of Philosophy

University of Pittsburgh

2020

UNIVERSITY OF PITTSBURGH

SWANSON SCHOOL OF ENGINEERING

This dissertation was presented

by

Mohan Wang

It was defended on

October 26, 2020

and approved by

Zhi-Hong Mao, Ph. D., Professor, Department of Electrical and Computer Engineering

Feng Xiong, Ph. D., Assistant Professor, Department of Electrical and Computer Engineering

Samuel Dickerson, Ph. D., Assistant Professor, Department of Electrical and Computer Engineering

Qing-Ming Wang, Ph. D., Professor, Department of Mechanical Engineering and Materials Science

Dissertation Director: Kevin P. Chen, Ph. D., Professor, Department of Electrical and Computer Engineering

Three-Dimensional Integrated Photonics in Transparent Substrates Enabled by Femtosecond Laser Fabrication

Mohan Wang, PhD

University of Pittsburgh, 2020

Unlike integrated electronic circuits that are built mostly on silicon wafers, integrated photonic devices involve a great variety of materials and platforms. The development of integrated photonic devices in both 2-D and 3-D architectures in each material and platform presents distinct fabrication challenges. The research in this dissertation explores the femtosecond laser as a versatile cross-platform manufacturing tool to fabricate 3-D photonic structures in transparent optical substrates.

This dissertation first presents the fabrication of multiplexable and distributed optical sensors in silica and sapphire optical fiber with high radius of curvature surfaces. Using a diffraction-limited oil-immersion fabrication setup, a reel-to-reel laser direct writing system was established to deposit laser energy inside optical fibers with micrometer precision. Through careful tuning of laser-matter interaction to form nanograting in fiber core, Intrinsic Fabry-Perot Interferometer arrays were fabricated with a high fringe visibility of 0.49 and low insertion loss of 0.002 dB per sensor. The temperature sensitivity, cross-talk, and spatial multiplexability of sensor arrays were investigated in detail. By continuously introducing nanograting as artificial Rayleigh scattering centers, femtosecond laser-fabricated Rayleigh scattering enhanced section could achieve an optimized propagation loss of 0.01 dB/cm with drastic improvement of the signal-to-noise ratio of over 35 dB for Optical Frequency-Domain Reflectometry-based distributed sensing.

Long-term high-temperature performance was successfully demonstrated with improved thermal stability.

This dissertation also explores the fabrication of high-density 3-D topological photonic circuits in glass substrates with flat surfaces. Inspired from solid-state physics, topological photonics has found potential applications such as quantum information processing and defect-resistant lasing devices. Through careful control of the multiphoton laser-matter interaction in the femtosecond time scale and nanometer spatial scale, we demonstrate the fabrication of high-density coupled and low-loss 3-D waveguide arrays with varying index profiles. This dissertation presents the experimental verification of lattice braiding, Thouless pumping under the presence of disorder, and the topological pumping in a higher-order system.

In sum, the dissertation studies the optics science of femtosecond laser-matter interaction and unveil the potentials of femtosecond laser as a powerful fabrication tool for 3-D photonic device fabrication for studies in optics science and for photonics applications in communication and sensing.

Table of Contents

List of Figures

Preface

To obtain a PhD degree is a life-changing experience. What I have learned during my PhD years is invaluable. I first arrived in Pittsburgh August 15, 2012 as a transfer junior and took Dr. Chen's class that fall semester. Dr. Chen would share many stories during the class, linking the dry mathematical equations to novel ideas and cool applications. I enjoyed his classes a lot. I feel wholeheartedly fortunate that I joined Dr. Chen lab for a PhD degree. I am very grateful to his tremendous support both financially and academically throughout the years. All the time I feel encouraged by his rich knowledge in the photonics area, his endless passion towards research, and his generous and sincere personality. It is also Dr. Chen who inspires me to keep pursuing the state-of-art research in photonics and helped me figure out my goal of finding a position in the academia. I could never thank Dr. Chen enough.

I am grateful to my committee members Dr. Zhi-Hong Mao, Dr. Feng Xiong, Dr. Samuel Dickerson, and Dr. Qing-Ming Wang for their precious efforts and time in serving as my Ph.D. exam committee members and carefully reviewing my dissertation. Their kind help and trust encourage me to present this work well and motivate me to keep improving the quality of my research.

I would also like to thank my colleagues and friends in the group Dr. Sheng Huang, Dr. Rongzhang Chen, Dr. Ran Zou, Dr. Aidong Yan, Dr. Shuo Li, Dr. Mohamed Zaghloul, Dr. Rongtao Cao, Dr. Zhaoqiang Peng, Dr. Hangjun Ding, Dr. Guanquan Liang, Dr. Hui Lan, Dr. Yang Yang, Dr. Hongqiao Wen, Dr. Hu Liu, Dr. Hao Zhang, Jingyu Wu, Kehao Zhao, Yuqi Li, Jieru Zhao, Zhichun Fan, Qirui Wang, Ya-Wen Huang, and Thomas Boyer, whose kind help and company make my PhD years colorful. I wish to specially express my gratitude to Dr. Sheng

Huang for all the heated debates on the femtosecond laser fabrication methods. I will always remember the consecutive day and nights tuning the laser and writing the waveguide circuits. I also wish to thank my friend Jingyu Wu for our lasting friendship and her great company. From everyone, I learned a lot.

I also wish to thank my collaborators from Pennsylvania State University for the great collaborative works. I wish to thank Dr. Mikael Rechtsman for his generous help and insightful suggestions. I also would like to thank Dr. Jiho Noh and Dr. Alexandra Cerjan for the helpful and intriguing discussions.

I wish to thank my friends in Pittsburgh. Sandy Weisberg, Maureen Barcic, Dr. Margarita Delgado Creamer, and Dr. Hesheng Bao for their kind friendship.

Finally, I wish to say thank you to my father and mother. Without their unshakable trust and support as always, I could never accomplish this PhD journey and have the courage to seek new adventures in this everchanging world.

1.0 Introduction

This dissertation focuses on the utilization of femtosecond laser direct writing technique to fabricate versatile optical devices on different transparent platforms. A femtosecond laser is a pulsed laser that has a pulse duration of 1 to 1000 femtoseconds (10^{-15} s). The ultrashort femtosecond laser pulse has a time scale much shorter than the material thermal diffusion time, which enables fast and precise deposition of energy in the nonthermal regime. Through a whole host of different nonlinear ionization effects, the femtosecond laser fabrication allows simple, fast, and flexible micromachining of photonics devices at a reduced cost. The femtosecond laser can be tightly focused inside a transparent substrate at a microscale focus, creating highly localized and accurate material modification, true 3-D photonics devices on a wide variety of transparent materials.

Femtosecond laser direct writing technique was first reported in 1996 by Davis et al [1]. Ever since then, the technology has been applied to the fabrication of numerous optical devices including integrated photonics circuit, optical data storage device, micro-fluidic medical chip, telecommunication optical interconnect, optical fiber sensor, laser oscillator, etc. These applications cover a wide range of applications including telecommunication, astronomy, optical imaging, topological photonics, environmental monitoring, bioengineering, and medical research [2]–[6]. In the femtosecond laser direct writing method, the femtosecond laser focal volume moves along a pre-programmed 3-D trajectory relatively to a transparent substrate mounted on a three-axis nano-precision stage. Permanent modification is created at the focal volume inside the transparent substrate, akin to the writing process with a pen and a paper. By designing and

programming the trajectory, complicated and versatile photonic devices can be written into the transparent substrate.

Traditionally, integrated photonic devices can be fabricated using a semiconductor-based method. Compared to the well-adopted photolithography approaches, there are many distinctive advantages of the femtosecond laser processing fabrication. First of all, femtosecond laser fabrication is fast, simple, and cost-efficient. Only a laser, a beam delivery system, and a motion stage are required to start a new design in femtosecond laser fabrication, while photolithography-based fabrication requires bulky and expensive equipment, cleanroom facilities, and large manufacturing site. Besides, the photolithography approach commonly involves multiple steps at the specialized semiconductor device fabrication facility. The test of a new design requires a new host of complicated procedures. In a sharp contrast, the prototyping of a different structural design can be conveniently done without the extra steps in femtosecond laser fabrication.

Secondly, the technique is highly flexible and versatile. The femtosecond laser wavelength is transparent to many different types of dielectric platforms, i.e., glass, crystal, polymer, bio-tissues. The flexibility allows the fabrication of devices using the material with the best fit to the application requirements. Depending on the material type, the ultrashort laser pulse can interact with these materials through different nonthermal and nonlinear mechanisms. By tuning a wide fabrication parameter window, all these interactions can be tailored to fabricate versatile materials for a wide range of applications.

Thirdly, the femtosecond laser enables the design and fabrication of true 3-D devices inside transparent substrate. The laser is able to induce a highly localized and permanent material modification in the micro-scale range at any point inside a transparent substrate. Through simple software programming to write the designed structure layer-by-layer, true 3-D and highly compact

photonics structures can be integrated on a transparent bulk chip in a single step. This opens up unprecedented opportunities that cannot be achieved through traditional methods.

Fourthly, femtosecond laser fabricated devices have demonstrated exceptional long-term stability under extreme environments, such as tense radiation, high temperature, corrosive gas, and strong electromagnetic field. While many industrial processes require the operation of devices under these otherwise challenging environments, novel manufacturing technologies are demanded for robust and safe monitoring devices. Femtosecond laser has been proven to be a powerful technology to fabricate devices that can endure harsh environments [7]–[11].

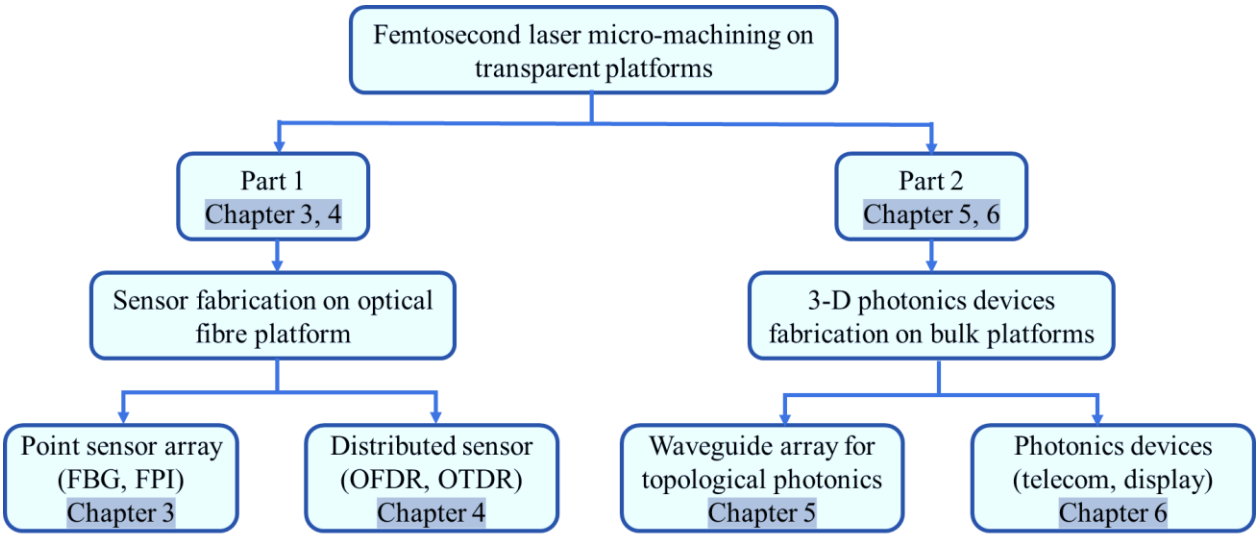

Figure 1 Flow chart of the organization of the dissertation.

The above-mentioned benefits have made femtosecond laser processing a powerful fabrication technique to address the distinct fabrication challenges of versatile optical devices for studies in optics science and industrial applications of telecommunication, sensing, etc. The objective of my PhD research work is to study the femtosecond laser as a cross-platform

manufacturing tool to fabricate novel 3-D devices on silica and sapphire substrates. Figure 1 describes the organization of this dissertation.

Chapter 1 and **Chapter 2** go over the background information for the rest of the dissertation. Chapter 1 provides a general overview of the fabrication technique and its advantages. Chapter 2 reviews the mechanisms of femtosecond laser-material interaction and the different regimes of femtosecond laser-induced modification on different dielectric platforms. As femtosecond laser fabrication involves a wide parameter space, chapter 2 also demonstrates how the fabrication parameter window can be tailored to the distinctive materials and platforms to control the various nonlinear processes at the laser focal volume.

Chapter 3 and **Chapter 4** describe the state-of-art femtosecond laser fabrication of optical fiber sensor devices on silica and sapphire optical fiber platforms with high radius of curvature surfaces. In Chapter 3, Quasi-distributed point sensors are demonstrated using the Fiber Bragg Grating (FBG) and the Fabry-Perot Interferometer (FPI) sensors. Their operation principles, characteristics, femtosecond laser fabrication procedure, multiplexing, and interrogation algorism are included in detail. In Chapter 4, Rayleigh scattering-based distributed sensor are fabricated and demodulated using the Optical Frequency Domain Reflectometry. Through tuning the fabrication conditions, fiber sensor devices which exhibits exceptional resilience under harsh environmental conditions can be fabricated with optimized performances.

Chapter 5 and **Chapter 6** describe the femtosecond inscribed high-density 3-D photonics circuits on bulk platforms. Due to the analogy between the Schrodinger equation and the paraxial Maxwell equation, the femtosecond laser-written evanescently coupled waveguide array is a powerful tool to study the optics science that is not observable through traditional methods. Chapter 5 demonstrates three projects performed with collaborative work with the Pennsylvania

State University to inscribe 3-D photonics lattices on bulk glass. These integrated structures can emulate topological photonics designs that are not accessible through traditional fabrication methods. On the other hand, the femtosecond direct writing technique enables fast and low-cost fabrication of complicated all-photonics devices which cannot be produced using the competing photolithography manufacturing technologies. Chapter 6 presents bulk devices fabricated using femtosecond laser direct writing that could be used in commercial applications such as display glass and telecommunication.

Chapter 7 presents a discussion and a summarization of the potentials of the femtosecond laser fabrication technology, following by an outlook for future research directions.

2.0 Physics Background

With the ultrashort laser pulses in the order of 10^{-15} seconds, the femtosecond laser can generate a high light intensity up to 10^{14} W/cm^2 at the laser focal volume. Energy is transferred from the extremely strong laser pulse to the transparent dielectric substrate through a wide variety of nonlinear absorptions, resulting in different material modifications that are permanent and highly localized. Chapter 2 goes over the background physics of the femtosecond laser-material interactions which are exploited for device fabrication throughout the rest of the dissertation. This chapter starts with an introduction to the femtosecond laser system setup, followed by the laser material-interaction mechanisms of the glass and crystal platforms. The last section provides a detailed analysis on the relationship between of these laser-material interaction mechanisms with the highly tunable fabrication parameter space.

2.1 Fabrication Setup

Common femtosecond laser systems include solid-state bulk laser, fiber laser, dye laser, and semiconductor lasers. The pulse duration of a femtosecond laser ranges from 10s to 100s of femtoseconds [12]. The laser used in this experiment is a solid-state Ti:sapphire regenerative laser system. Figure 2 shows the schematic of the system composed of a continuous wave diode laser pumping source (Verdi 18), a laser oscillator (Mira 900), and a regenerative amplifier (RegA 9000). The Verdi diode laser generates 12-W 532-nm laser light that is directed to both oscillator and the amplifier as the pumping source. The Mira 900 Ti:sapphire laser oscillator generates high

repetition rate (1.97 m long cavity, 76 MHz) femtosecond laser pulses (270 fs) at 800 nm. The femtosecond laser pulse is achieved using a slit-based passive mode locking system based on the optical Kerr effect. The output laser pulses act as the seed light which is fed into the RegA 9000 laser amplifier through two external mirrors.

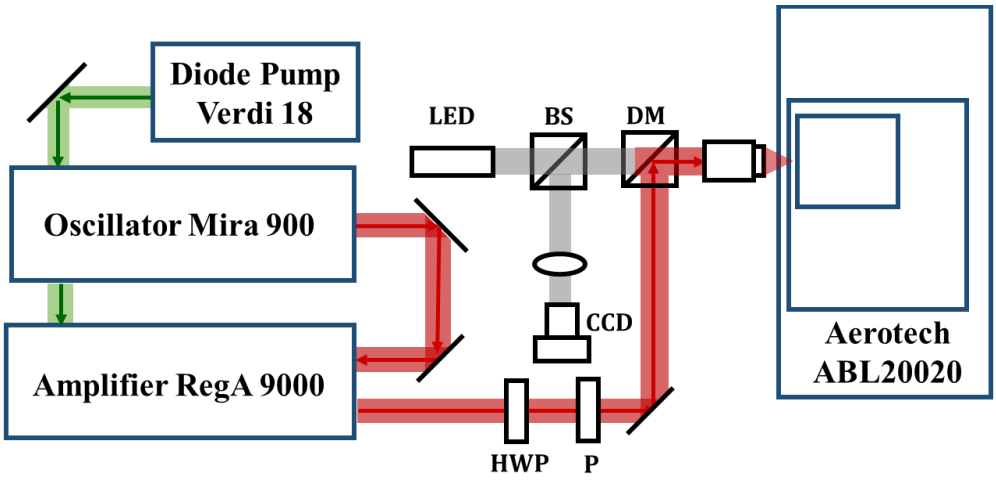

Figure 2 Schematic of the Coherent regenerative femtosecond laser system. HWP: half-wave plate; P: polarizer; DM: Dichroic mirror; and BS: beam splitter.

A Q-switch in the RegA 9000 amplifier system holds the lasing until a pulse from Mira 900 oscillator was injected. The 800-nm, 270-fs seed laser pulse is first injected into the acousto-optic cavity dumper of the laser amplifier. The pulse is amplified over 25 roundtrips and was chirped during each roundtrip. The pulse duration is expanded to be approximately 40 ps for the purposes of safe energy operations. After the laser pulse gains enough energy, a pulse compressor which consists of a single diffraction grating recovers the pulse duration to 270 fs from a total of 4 passes. The amplifier could provide 250-kHz laser pulses with the pulse energy up to 1.2 μJ. The pulse width of the femtosecond laser was measured by a home-made auto-correlator system to be

270 fs. Figure 3 shows a photo of the laser system. The laser delivers linearly polarized pulses with a beam diameter of 2 mm and M^2 <1.5.

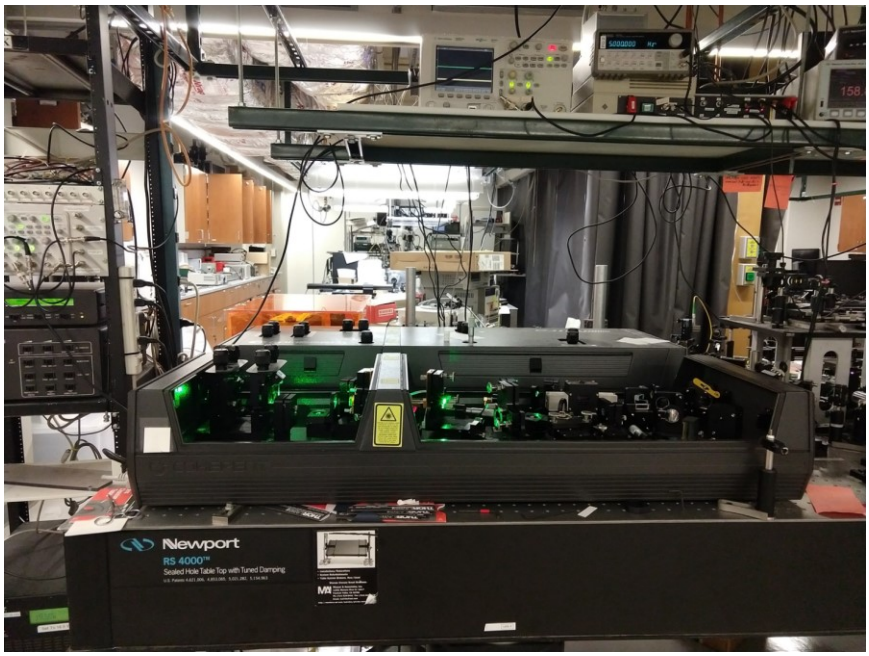

Figure 3 Photo of the regenerative Ti:sapphire laser system during maintainence, including the pump laser diode (back), oscillator (middle), and amplifier (front).

The on-target pulse energy can be tune by a half-waveplate and polarizer. During the laser inscription process, the transparent substrates are mounted on a three-axis nano-precision motion stage (Aerotech ABL20020). The laser focal spot in glass is calibrated with the assistance of a 4-f imaging system using white LED illumination light and a CCD camera. During the fabrication process, the sample is moved along a designed trajectory to perform the writing process with the laser focus spot is fixed, which is similar to the inscription with a pencil and a paper.

2.2 Laser-material Interaction Mechanisms

At a relatively low pulse energy, femtosecond laser pulses can transmit through the transparent substrate. As the pulse energy reaches a certain threshold, the femtosecond laser pulses are absorbed by the transparent material through a combination of nonlinear processes. Since the birth of femtosecond laser, the interaction between ultrafast light-material interactions has attracted much research curiosity, while debates are still open for the physics behind some of the mechanisms. The combined nonlinear processes can create different types of material modifications and are highly controllable through carefully chosen the fabrication parameters. The desirable modification types are determined by the different application needs. The fabrication of versatile devices with the optimal behavior can be achieved by tuning a wide parameter space. This section goes over some of the most discussed physics behind the femtosecond laser-material interaction to demonstrate how these physics phenomenon can be utilized to fabricate the novel devices.

2.2.1 Nonlinear Absorptions

At the femtosecond time scale and above a certain threshold, electrodynamics processes take place inside the substrate that is usually transparent in the visible and near infrared red (NIR) wavelength. The femtosecond laser intensity reaches ~10^{14} W/cm^2 at the focal volume. The laser pulse energy is transferred into the dielectric material through a combination of nonlinear ionization processes, namely, multiphoton, tunneling, and avalanche ionization. These ionization processes transform the dielectric material into an absorbing plasma with metallic properties, and

optical absorptions inside material takes place. The time scale is much shorter than the material heat diffusion time scale, and the interaction is nonthermal and highly localized.

Multiphoton ionization The single-photon energy is 1.55 eV for an 800-nm wavelength femtosecond solid-state laser or 1.20 eV for a 1030-nm wavelength femtosecond fiber laser. The bandgap energies E_g of some common dielectric material are as follows: fused silica (7.5 eV), CaF2 glass (10.2 eV), chalcogenide glass (2.2 to 2.4 eV), and sapphire (8.8 eV) [13]. It can be calculated from these numbers that more than one photon is needed to liberate an electron from the valence band. An electron would sequentially absorb the energy from k photons with the energy of $h\nu$ to overcome the bandgap energy E_g. As the femtosecond laser pulse intensity reaches the threshold intensity, multiphoton ionization takes place under the condition:

$$k h\nu > E_g \qquad (2-1)$$

Free electrons are excited to the conduction band at the laser beam focus spot. The multiphoton ionization will provide the seed electrons for the avalanche ionization process. The absorption rate of the multiphoton ionization can be described by [12]:

$$P(I) = \sigma_k I^k \qquad (2-2)$$

I is the laser intensity. The multiphoton ionization coefficient σ_k is determined by the material and the number of absorbed photons. As the intensity of the incoming light increases, the multiphoton ionization becomes stronger.

Tunneling ionization At a higher electric field amplitude, the electron's Coulomb potential energy barrier is lowered due to the high intense field. Tunneling ionization takes place, in which an electron is able to "tunnel" from the valence band to the conduction band. Compared to multiphoton ionization, the tunneling ionization is less dependent on the laser intensity than the

multiphoton ionization. Though both mechanisms exist simultaneously, the competing between the multiphoton ionization and tunneling ionization are dependent on the well-adopted Keldysh model:

$$\gamma = \frac{\omega}{e}\left[\frac{mcn\epsilon_0 E_g}{I}\right]^{\frac{1}{2}} \qquad (2-3)$$

ω is the laser light field oscillation frequency, e and m are the electron charge and reduced mass, E_g is the material bandgap, and I is the intensity at the focal volume [14]. It can be seen from the equation that the dominating mechanism is dependent on the field intensity. When the Keldysh parameter is larger than 1.5, the photoionization process is mainly a multiphoton ionization, while the tunneling ionization dominates otherwise.

Avalanche ionization When an electron is freed at the bottom of the conduction band as a result of the multiphoton ionization, it acquires kinetic energy and is accelerated. As the energy exceeds the conduction band minimum by more than the bandgap energy, the electron will liberate another electron at the valence band, forming two free electrons close to the minimum of the conduction band. The conduction band electron density N continues to grow:

$$\frac{dN}{dt} = \eta N \qquad (2-4)$$

The avalanche ionization rate η is dependent on the laser intensity:

$$\eta = \alpha I \qquad (2-5)$$

α is the avalanche ionization coefficient depending on the material. The original seed electron of avalanche ionization can come from multiphoton absorption or thermal excited electrons. As described from the equation, the process will repeat itself, and the free electron density grows

exponentially [15]–[17]. An electron plasma forms at the laser focus spot. As the plasma frequency approaches the laser frequency, the material becomes stronger absorbing.

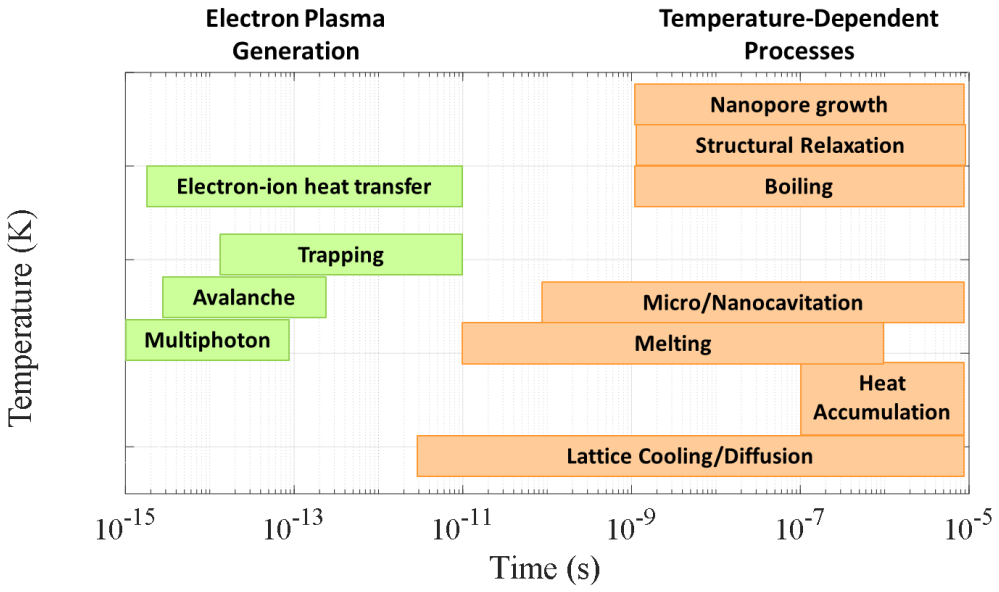

Figure 4 Laser material interaction at a function of time and the localized temperature change.

Self-focusing and Defocusing As the laser intensity increases above a certain threshold, the refractive index is dependent on the laser intensity. This nonlinearity can be described with:

$$n = n_0 + n_2 I \qquad (2-6)$$

n_0 is the refractive index under normal conditions, while n_2 is an nonlinear refractive index determined by the field intensity. The threshold of self-focusing is determined by a **critical power**:

$$P_{crit} = \frac{3.77\lambda^2}{8\pi n_0 n_2} \qquad (2-7)$$

The threshold for sapphire is 1.9 MW and silica as 2.0 MW. Self-focusing would cause the pulse to be elongated than the geometric focal volume. On the other hand, due to the generation of

an electron plasma at the focal volume, a defocusing also takes place. Self-focusing would dominate when using a low-NA (NA<0.65) objective, while the multiphoton ionization and avalanche ionization are the main processes when using a high-NA objective.

Nanograting Formation Femtosecond laser is able to induce nanoscale structures below the diffraction limit. Using linearly polarized laser pulses, these structures consist of nanocracks whose direction is aligned perpendicular to the beam propagation direction and laser polarization direction. These cracks have a sub-wavelength period and are filled with nanopores of a 5 to 20 nm radius. Recent studies have thrown light on the formation of nanograting. Multiple laser pulses arriving at the focal volume increases the local temperature and pressure. As a result, nanograting are formed as a result of glass decomposition by cavitation, as the main mechanism.

Thermal Processes At a longer timescale, thermal processes take place. The thermal diffusion coefficient of common dielectric materials is usually 10^{-3} cm^2/s, thousands of times lower than that of a metallic material. This low thermal conductivity indicates that the region under laser irradiation will cool in a time in the scale of 10s μs. At the picosecond time scale, the conduction band electrons are heated. Energy is transferred to the lattice through thermal diffusion, leading to localized unidirectional melting and distrusted regions occur at the laser focus spot.

2.2.2 Types of Modification

Fused silica is one of the most used transparent platforms. It is also the main material of optical fibers. There are generally three regimes of femtosecond laser-induced material modification in fused silica [18], [19], while these three regimes also apply to other common transparent substrate materials, such as borosilicate glass, sapphire, etc.

Type-I When the laser pulse intensity is sufficiently high that exceed the optical breakdown threshold of the material, an isotropic and permanent refractive index takes place. Stress is induced at the focal volume, resulting in local densification, that leads to local refractive index increase. A threshold intensity determines the minimum pulse intensity required to conduct a permanent modification inside a material:

$$I \propto E \cdot \frac{NA^2}{\tau\lambda^2(1-NA^2)} \qquad (2-8)$$

τ is the pulse duration, E is the pulse energy, NA is the Numerical Aperture (NA) of the focal geometry, usually, an electromagnetic field intensity of 5×10^{13} W/cm^2 needs to be equal or larger than the electric field which binds the valence band electrons in the atom of 10^9 V/m. The inscribed waveguide structure has low propagation losses and is smooth in shape. This regime is typically used to fabricate optical devices and 3-D photonics circuit inside a transparent bulk material [20], [21].

Type-II With a higher pulse intensity, self-assembled nanostructure with a sub-wavelength period can be introduced at the laser focal spot, known as nanograting. The structures usually have a period of $\lambda/2n$. The Type-II regime is characterized by its anisotropy, higher loss, and impressive thermal durability up to 1200°C [22]. Nanograting has been well studied to locally increase the chemical etching rate in femtosecond laser-assisted etching to produce micro-fluidic channels [23], [24]. This regime has also been exploited to fabricate birefringent devices. Because the structure can be written and erased, they are promising candidates for rewritable data storage applications. Nanograting formation is dependent on the laser pulse energy, pulse duration, and laser repetition rate.

Type-III As the pulse intensity continues to increase, an irreversible and disruptive change in material occurs due to the large amount of deposited energy. The lead to micro-explosion inside material and void formation. ablation and material damage. This regime has been utilized to fabricate optical memory storage devices [25]–[27].

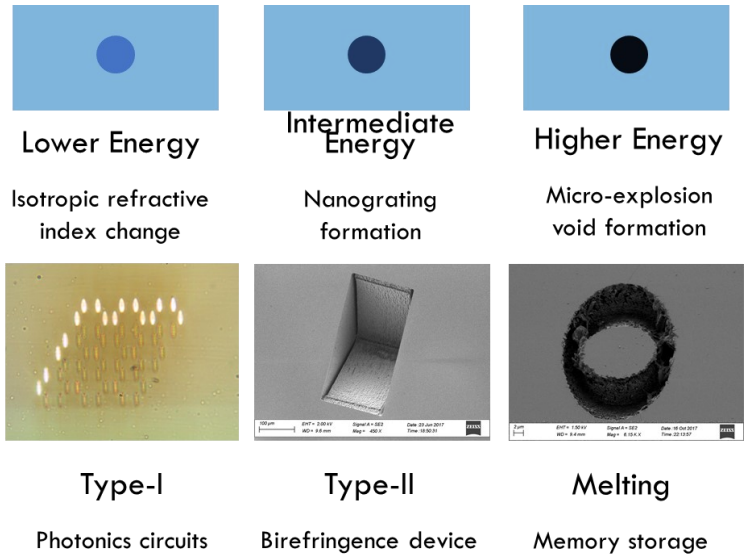

Figure 5 The three regimes of femtosecond laser induced structural change.

The most common use of the above-mentioned modifications is to fabricate optical waveguides, which is the basic unit of a photonics devices. It is composed of a light guiding structure buried in a bulk platform, surrounded by a lower index layer. In a **glass** platform, a waveguide can be formed by inscribing a track of Type-I modification. The waveguide consists of a region with positive refractive index change as compared with the surrounding the unmodified material. The spatial profile of the femtosecond laser can be extracted from the free electron density $n(t)$ at the focal volume. A simple model can be described by the rate equation [27]:

$$\frac{dN}{dt} = \alpha I(t)N(t) + \sigma_k I^k(t) \qquad (2-9)$$

α is the avalanche coefficient, σ_k is the k-photon absorption coefficient, and $I(t)$ is the temporal profile of the laser pulses presented in the following equation [14]:

$$I(t) = I_0 e^{-\left(\frac{t}{\tau_p}\right)^2} \qquad (2-10)$$

Modifications inside **crystal** require a higher energy density. The transmission behavior of waveguide in crystalline material is different than that inside a glass material. At the femtosecond laser irradiation, the atoms inside the crystal substrate are re-arranged. The change in the lattice structure leads to a lower density, and thus the stress-induced waveguide would introduce a negative refractive index change at the focal volume. While the glass waveguide is formed by inscribing the Type-I laser modification as the waveguide core, optical waveguides inside crystal is formed by inscribing the cladding structure with reduced refractive index. The guided mode is confined in the unmodified region that has higher refractive index between two tracks.

2.3 Fabrication Parameter Space

One characteristic of the femtosecond laser fabrication method is a wide parameter space, which provides great controllability over the nonlinear mechanisms and material modification regimes. All these can be tuned with fabrication parameters, such as pulse energy, pulse duration, repetition rate, laser wavelength, beam polarization, focusing volume, translation speed, and writing geometry. Meanwhile, the thresholds of the generated effects are also highly dependent on the material characteristics of the transparent platforms, such as bandgap and thermal expansion coefficient. And thus, for each different material and platform, the fabrication parameters need to be tuned to inscribe a device with optimized performances inside the transparent substrate.

Wavelength Different from an ultraviolet (UV) laser irradiation where only one photon is needed to excite the valence band electron to the conduction band, the nonlinear multiphoton absorption takes place at the near infrared red (NIR) femtosecond laser wavelength ranges. Depending on the wavelength and the material bandgap, two to four photons are needed. The electron would simultaneously absorb $khv > E_g$ photons to be liberated to the conduction band. Laser with lower wavelengths produce photons with higher energies, and thus less photons are needed for the multiphoton process to take place. The material damage threshold intensity is dependent on the wavelength, as well as the beam focus strength. Due to the diffraction limit, a smaller wavelength can generally fabricate structures with better resolution. The above-mentioned dependences make the laser wavelength a critical parameter for different applications. In fabrication, the femtosecond laser wavelength can be tuned through second and third harmonic generation from the NIR to the visible or UV wavelengths.

Pulse Duration For a pulse duration which exceeds several picoseconds, the peak intensity will be too low to trigger the nonlinear multiphoton or tunneling ionization processes due to the longer pulse duration. Even though the avalanche ionization can take place starting from free electrons in the conduction band due to material impurities, the absorption process is hard to be controlled and is subject to fluctuations. For a femtosecond laser pulse, the intensity at the focus is sufficiently high to introduce enough seed electrons through multiphoton ionization, resulting in an avalanche ionization and local material breakdown. The seed electron generation can be controlled precisely, and the process is highly tunable [19]. Besides, the femtosecond pulse duration is much shorter than the heat diffusion timescale of materials. The nonlinear absorption take place before the energy is transferred to the material lattices. Therefore, the laser-material

interaction is nonthermal, allowing optical breakdown inside the material at a much smaller scale than the thermal processes.

Repetition Rate For a femtosecond pulse with a lower repetition rate (<200 kHz), the material modification is produced almost by individual pulses, heat will be diffused between two consecutive laser pulses and mechanical relaxation will be completed. In this case, the material modification introduced by each laser pulse is independent from each other. Since the thermal diffusion time in common dielectric material is in the time scale of microseconds, the modification under this low repetition rate regime is considered nonthermal and the shape of the modified region matches the intensity distribution of the laser beam. At higher repetition rate of hundreds of kHz to MHz, the material is not completely relaxed thermally and mechanically between two pulses, a pulse-to-pulse cumulative effect needs to be taken into consideration. As more and more pulses arrive, the laser serve as a localized source of heat [24]. The structural change is dominated by heating, melting and cooling dynamics of the material and around the focal volume. After the pulse train is turned off, the heated material quenches, leading to higher density state with higher refractive index change. The cross-section of the introduced modification is more circular, and the modification zone is larger than the focal spot due to the heating effect.

Writing Speed When writing a waveguide structure, the writing speed determines the degree of the femtosecond laser pulse accumulation effects. While lowering the repetition rate can reduce the pulse overlapping effect, similar effects can also be achieved through reducing the scan speed and increasing the pulse energy [28].

Pulse Energy The thresholds of nonlinear ionization processes are determined by the pulse energy. When the pulse energy is above the nonlinear absorption threshold, material absorption takes place. Pulse energy determines the thresholds of the modification regimes discussed in

section 2.2.2. Figure 6 presents a general relationship between the three fabrication parameters and the three femtosecond laser modification regimes.

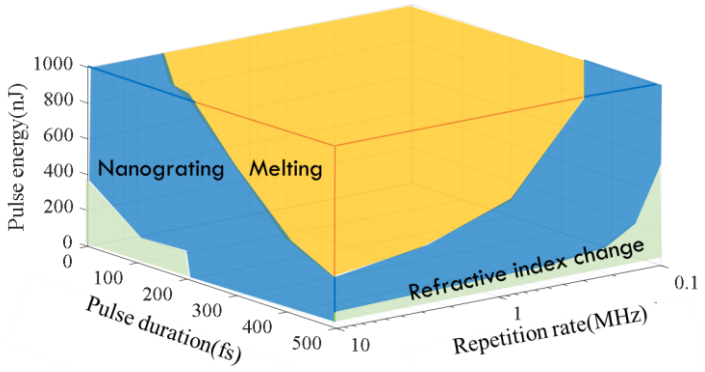

Figure 6 The femtosecond laser material modification regimes in fused silica, the schematic is plotted based on experimental data reported in [29] [30]**.**

Focusing The focal volume is characterized by the beam waists and the Rayleigh range of the laser focus. And thus, it determines the shape of the waveguide structure. The mild focusing scheme refers to a beam waist of several micrometers, while a tight focusing is usually close to the diffraction limit. The laser intensity threshold is dependent on the beam waist. A high power of several μJ is required for the mild focusing for material breakdown, while a tightly focused beam needs only a lower intensity of 10s nJ. The relationship between the deposited energy required to introduce an optical breakdown inside material and the NA of the focusing objective is dominated with the following equation:

$$E_{th} = \frac{I_{th}\tau\lambda^2}{\pi NA^2 + \frac{I_{th}\lambda^2}{P_{cr}}} \qquad (2-11)$$

P_{cr} is the critical power of the material self-focusing. It can be viewed from the equation that as the NA increases, the energy threshold decreases.

Writing geometry There are two different types of writing geometries in femtosecond laser direct writing. The transparent platform is translated along the beam propagation direction in the longitudinal writing scheme, while the sample is translated perpendicular to the beam propagation direction in transversal writing. Both methods have their advantages and disadvantages. The transversal writing scheme is more widely adopted because of its flexibility to fabricate samples with a larger size. The maximum processing range is dependent on the range of the translation stage. However, the written waveguides have an asymmetrical mode field at the cross-sectional region. On the other hand, the longitudinal writing introduces more symmetric waveguide cross-section, meanwhile, the maximum range of fabrication is constrained by the small working distance of the focusing objective.

In sum, the femtosecond laser fabrication condition can be used to tune the properties of the fabricated devices, such as refractive index change, propagation loss, waveguide size, birefringence, etc. The laser-material interaction is also dependent on the material properties of the transparent substrate, such as the bandgap and thermal conductivity. The dependence of all the different laser-material interactions on the fabrication parameters needs to be taken into careful consideration to design versatile devices on different platforms with optimized performances.

3.0 Femtosecond Laser Fabrication of Multiplexable Fiber Sensors

Optical fiber has been widely applied in telecommunication to transmit light-carried signal between two ends. An optical fiber is a miniature device that is 10s of micrometers in size and can be made from glass, crystal, or plastic. Using the advanced femtosecond laser manufacturing methods, optical fiber sensor devices can be integrated inside the fiber core with the protective coating intact. An optical fiber sensor can both transmit the light signal over distance and track the changes of environmental parameters. The Fiber Bragg Grating (FBG) and the Fabry-Perot Interferometer (FPI) are two types of optical fiber sensors that are most widely used. Both sensors can perform sensing at a fast sampling speed for changes in measurands, i.e. temperature, strain, vibration. Through careful tuning the fabrication parameters, multiplexation can be achieved for both sensor types to achieve quasi-distributed sensing using a low-cost interrogation system. Chapter 3 describes the fabrication of the FBG and FPI sensor arrays on a single-mode silica-core optical fiber through femtosecond laser direct writing and a reel-to-reel setup. The sensors are created using the Type-II femtosecond laser modification or the nanograting and exhibit stable performances under high temperature at 1000°C.

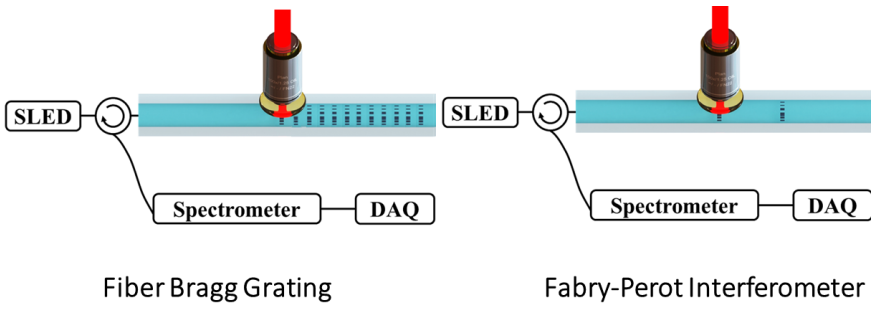

Figure 7 The fabrication and demodulation setup of (a) an FBG and (b) an FPI sensor device.

3.1 Motivation and Background

Many industrial processces take place under extreme physcial conditions. Additive manufacturing systems, advanced propulsion systems, and nuclear and fossil fuel production processes all involve various extreme conditions in their environments such as high temperatures, strong radiation and high pressures amongst others etc. A common challenge for optimizing the processes that occur in extreme environments is the lack of tools that can gather high temporal and spatial resolution information. For decades, very few electronical sensors (e.g. thermocouples) were considered suitable for measurements in extreme envrionmental conditions. Moreover, electronic sensors are point devices, that limit the spatial resolution of measurements. The deployment of electronic sensors in extreme environments also involves significant challenges in the installation as each sensor must have its dedicated wiring and reading instruments.

In addition to electronic sensors, both silica and sapphire optical fibers have demonstrated exceptional stability under harsh envirornmental conditions [8]–[11]. These optical fibers are miniature light-guiding devices that are chemically inert, resilient to radiation and high temperatures, as well as immune to strong electromagnetic fields. Unmodified optical fibers are able to perform distributed sensing over a long distance with a high spatial resolution, by utilizing the intrinsic scattering inside the fiber core. Meanwhile, using the advanced laser manufacturing techniques, multiplexable point fiber sensors such as FBGs can also be fabricated in the optical fiber to perform multi-point measurements using a single fiber. Sensing measurement does not require complicated wiring and as both measurement and signal transmission are possible using the same fiber sensor. With these unique traits, fiber sensors are a promising alternative candidate to address the challenging environmental monitoring requirements in extreme environments.

Fiber optics point sensors based on FBGs are one of the most well-developed optical fiber sensing devices widely used to perform various measurements. Traditionally, FBGs have been fabricated using UV lasers with continuous wave (cw) or -ns pulse duration outputs [10], [11]. Using various interferometry exposure schemes such as the phase mask approach, FBGs can be fabricated with very low insertion loss, thus enabling dense multiplexation of many FBGs for high spatial resolution measurements [31], [32]. However, the UV laser-fabricated FBG requires photosensitized fibers either through a special dopant in fiber cores or the photosensitization process such as hydroen loading. Moreover, the UV-laser produced FBGs cannot sustain temperatures higher than 300°C and will be erased at a temperature of 700°C unless further processed [33], [34].

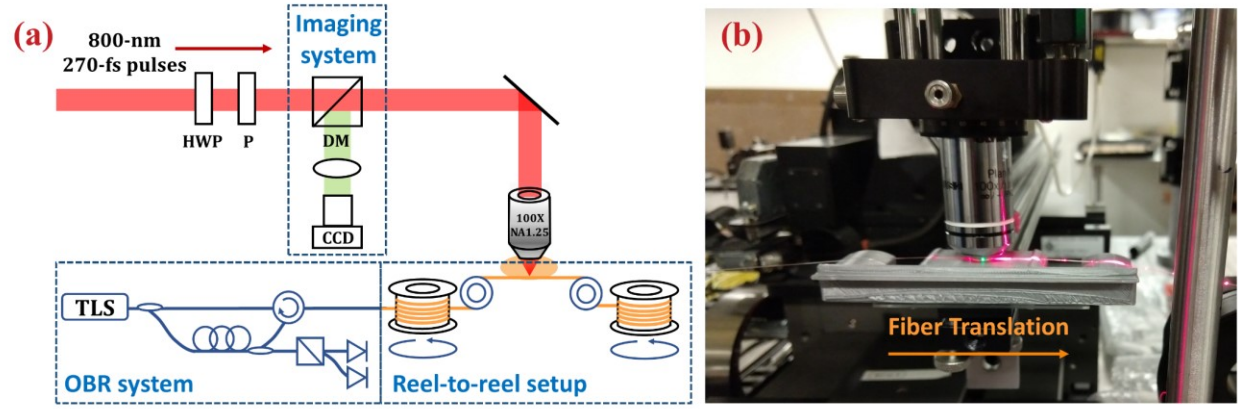

Figure 8 (a) The schematic and (b) the photo of the fabrication setup for optical fiber writing.

Alternatively, the femtosecond lasers with an output usually at the NIR wavelength have also been used to fabricate fiber sensor devices such as FBGs. With the highly localized microscale focus and ultra short pulse duration, femtosecond laser can deposit optical energy with extremely high intensity up to 10^{14} W/cm^2 at the focal volume to initiate a whole host of nonlinear absorption

processes [35], [36]. Through these nonlinear laser matter interactions, femtosecond lasers can be used to inscribe FBGs using interferometry exposure (e.g. bulk interferometer and phase mask) approach akin to the UV laser FBG fabrication [37], [38]. Since the femtosecond laser can produce highly confined material modification through nonlinear absorption, different direct writing schemes have also been developed. Depending on the writing geometry and procedure, these methods include: point-by-point, plane-by-plane [39], [40], line-by-line [41], pitch-by-pitch [42], and continous scanning [39].

Both the **Type-I** and **Type-II** femtosecond laser modification regimes have been used to fabricate FBGs, which correspond to the Type-I-IR and Type-II-IR FBG [43]. The Type-I modification results in low loss and and gives a uniform output. Furthermore, the effect is similar to those refractive index changes induced by UV laser irradiation [44]–[46]. However, these Type-I FBGs often degrade at 1000°C if not thermally processed, as compared to the Type-II-IR FBG which demonstrates long-term stability in both hign temperature, up to 1000°C with minimal decay and radioactive environments [47]. The exceptionaly harsh enviornmental resistence of Type-II FBG is inseparable from femtosecond laser-inscribed nanograting, both of which have been demonstrated to have exceptional long-term stability under 1100°C [48], [49]. Moreover, various research studies have also confirmed the formation of nanograting inside the fiber core of Type-II FBG [50], [51].

Though fiber sensors fabricated with the femtosecond laser Type-II modifications exhibit exceptional high-stability under extreme temperatures and incur high insertion losses as compared to fiber sensors fabricated by femtosecond Type-I modification using either UV cw or -ns pulse duraton lasers. The high insertion losses incurred in Type-II femtosecond modification could be attributed to light scattering by the nanograting formed in fiber cores [22]. Even though both the

UV laser-fabricated and femtosecond laser-fabricated FBGs attribute the device manufacturing process to the periodic laser-induced modification, UV laser-fabricated FBGs can have an insertion loss as low as 0.002 dB [38], while the insertion losses of the femtosecond laser fabricated Type-I FBGs are much higher. Prior research studies report insertion losses of Type-I FBGs fabricated by femtosecond lasers at <0.1 dB [37]–[41], however these losses are highly depedent on FBG parameters such as grating strength and fabrication methods. In sharp constrast, the typical insertion losses of the Type-II FBG are between 0.1 and 1 dB [40], [52], [53]. The increased loss of Type-II FBG could limit the multiplexing capability of these fiber sensors.

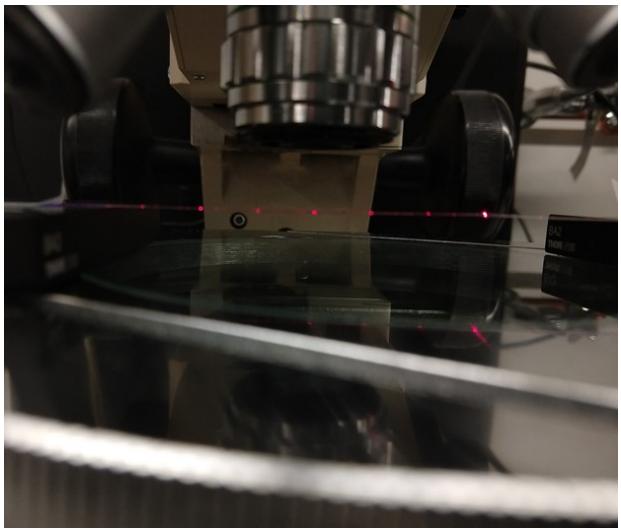

Figure 9 Photo of cascaded IFPI scattering 638 nm red light.

The **FPI** sensors are promising alternatives to the FBGs. An FPI sensor is composed of a pair of reflectors inside the optical fiber core. Light from the two reflectors interfere with each other, giving rise to a interference fringe at the detector. The fringe can be used to extract the physical parameter change along the FPI from the cavity length change. There are two main types of FPIs. An Extrinsic Fabry-Perot Interferometer (EFPI) which is fabricated from inserting an

external fiber part [54] or an air gap [55] between two cleaved optical fibers sections. Femtosecond lasers have been used to perform micromachining on a cleaved optical fiber end-facet to create a cavity, followed by fusion splicing to form EFPI diaphragm sensors for pressure [56] and refractive index [57] measurements. By depositing a Pd film over the femtosecond laser micromachined EFPI cavity, hydrogen sensing can also be performed [58]. The femtosecond laser ablation technique has also been used to produce a micro-notch to form an IFPI inside a single-mode optical fiber and a photonic crystal fiber for both refractive index [59] and temperature measurements [60], [61]. Finally, utilizing femtosecond laser-assisted etching, multiplexed IFPIs can be formed in silica fibers for refractive index sensing [62]. However, FPI devices formed by laser micromachining techniques can incur high insertion losses that limit multiplexing capability and performance. Moreover, physical features produced by the laser micromachining processes have significant impact on mechanic integrities of fibers. As a result, their multiplexing capability suffers from high insertion loss and degradation which occurs with increased cavity length.

On the contrary, an Intrinsic Fabry-Perot Interferometer (IFPI) can be fabricated by the integration of the reflector inside an optical fiber, such as a pair of FBGs [63] or micro-reflectors [64]. Compared to EFPIs, IFPIs are easier to package and handle, and have lower insertion loss and are well suited for multiplexed measurements. Dense multiplexing of IFPI sensors can be achieved by weak FBG arrays inscribed by UV laser [63]. However, IFPI sensors formed by FBG reflectors only produce interference fringe within FBG resonance wavelengths. This could potentially reduce the accuracy of demodulation algorithms to determine the cavity length of devices. Additionally, FBGs inscribed by UV lasers do not have good stability at high temperatures. FBG fabrication also requires a hydrogen loading process for standard optical fibers or photosensitive fibers [65]. Femtosecond lasers have been used to fabricate Type-I as

temperature, strain, pressure, vibration, and gas concentration sensors [66]–[72]. However, the same challenge for the Type-I FBG exists in the Type-I FPIs, unless further processed, the fiber sensor would suffer from degradation under long-term high-temperature operation at 1000°C.

Femtosecond laser induced Type-II modification can be applied in IFPI fabrication. The challenges related to Type-II FBG can be addressed by Type-II IFPI sensors. FBGs are composed of thousands of periodic Type-II modifications. For example, a 1-cm long FBG with 50% duty cyles consists of 5-mm section of fiber core with nanograting structures, whereas an IFPI sensor is composed of only a pair of μm-size reflectors inside the optical fiber core. Scattered guided light from the two reflectors are sufficient to produce interference fringes. These fringes can be used to extract the IFPI cavity length changes caused by physical parameter changes. As a result, the insertion loss incurred by nanograting-induced light scattering can be significantly reduced. Overall, this process improves the multiplexability of high-temperature stable fiber sensors. Section 3.3 demonstrates the fabrication of low-loss and highly-multiplexable Type-II IFPI sensor arrays as 1000°C stable temperature sensors. Through optimization of laser processing, the insertion loss of Type-II IFPI devices has been optimized to be as low as 0.002 dB/device [73], [74].

3.2 Type-II-IR Fiber Bragg Grating

This section presents the operating principle, fabrication method, multiplexation, demodulation, and the high temperature sensing performances of the femtosecond laser fabricated Type-II FBGs. The FBGs described in this chapter were formed by the point-by-point femtosecond

laser direct writing, formed through Type-II modifications, or the nanograting, that can sustain high-temperature environments with stable performances.

3.2.1 Operating Principle

When an FBG is illuminated by a broadband laser light, the light will be reflected from the sets of periodically modulated planes of the FBG structure. Light reflected from each surface will interfere with each other, while one single wavelength will be reflected from the FBG sensor. The light that is not in resonance will transmit through the FBG, while light of the resonate wavelength will be reflected from the structure. Thus, an FBG can act as a wavelength bandpass filter for the reflected light and a notch filter for the transmitted light. The refractive index modulation inside an FBG can be described in the following equation:

$$n(z) = n_0 + \Delta n \sin\left(\frac{2\pi}{\Lambda}\right) z \qquad (3-1)$$

n_0 and Δn are the DC and AC components of the refractive index modulation at the FBG inscription area, Λ is the modulation period, and z is the light propagation direction. While the center wavelength of the reflection, the FBG reflectivity, and bandwidth can be deducted from the coupling mode theory and the Bragg's law:

$$\lambda_B = 2n\Lambda \qquad (3-2)$$

$$R_{peak} = tanh^2|\kappa|L \quad |\kappa| = \frac{\pi}{\lambda}\Delta n \qquad (3-3)$$

$$\Delta\lambda = \lambda_B \kappa \sqrt{\left(\frac{\Delta n}{2n}\right)^2 + \left(\frac{1}{N}\right)^2} \qquad (3-4)$$

λ_B is resonant wavelength, $|\kappa|$ is the coupling coefficient, L is the FBG length, N is the number of FBG periods.

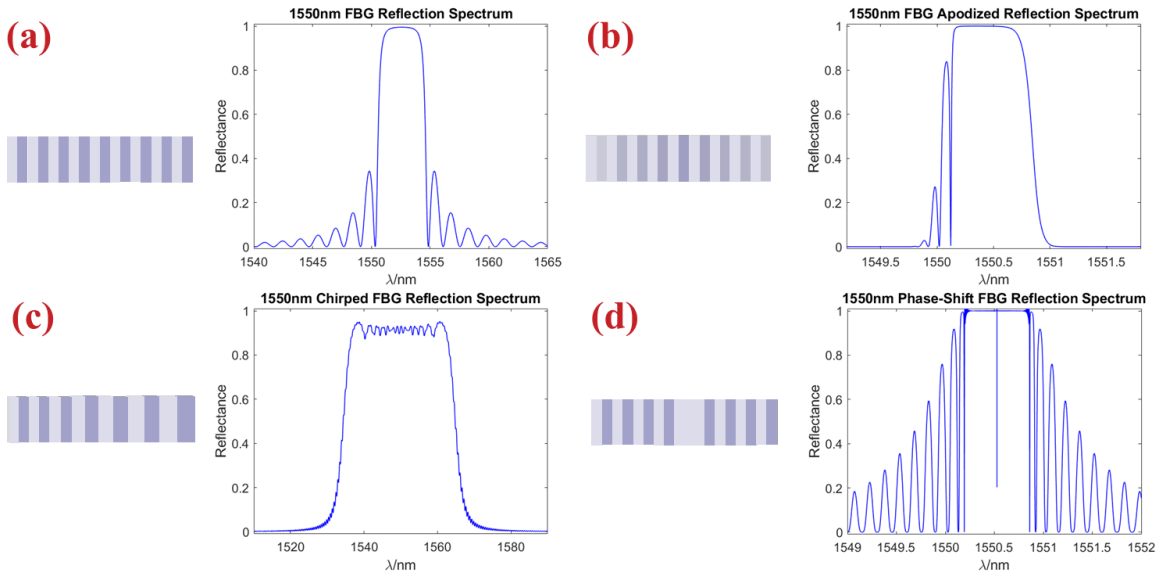

Figure 10 The diagram and spectrum of (a) normal, (b) apodized, (c) chirped, and (d) phase-shifted FBGs.

The Bragg resonant wavelength λ_B is dependent both on the grating period and the refractive index, while both are subjected to changes based on environmental parameters change. During temperature variations, the grating period changes according to the thermal expansion and contraction, while the fiber sensor refractive indices changes due to the thermal-optic effect. As a result, the resonant wavelength of the FBG would shift due to temperature and strain changes, described with the following equation:

$$\frac{\Delta\lambda_B}{\lambda_B} = \left[P_\varepsilon(\alpha_s - \alpha_f) + \sigma\right]\Delta T + P_\varepsilon \Delta\varepsilon \qquad (3-5)$$

α_s and α_f are the thermal expansion coefficients, σ is the thermo-optic coefficient, and P_ε is the strain-optic coefficient. The shift in the center wavelength can be used to monitor the

environmental parameter changes. While FBG with different resonant wavelengths can be demodulated spectrally, the sensor can be multiplexed to achieve quasi-distributed sensing of temperature and strain.

3.2.2 Nanograting Formation for Type-II Modification

In order to fabricate the Type-II fiber sensor devices which is made from nanograting, a Scanning Electron Microscope (SEM) was used in this and the following chapters to observe the correlation between the fabrication conditions and the femtosecond laser-induced modifications. Fiber sensors were fabricated using different pulse energies and cleaved at the locations of the laser modification regions. The cross-sections were observed under the SEM. Figure 11(a) presents SEM photos of nanograting formation in the center of optical fiber cores. As presented in section 2.2.2, the threshold of nanograting formation is dependent on fabrication conditions including pulse energy and duration, and laser repetition rate [29], [75]. With a fixed laser repetition rate and pulse duration, the pulse energy was varied to find the nanograting formation threshold. A pulse energy between 80 to 160 nJ was used to inscribe the fiber sensor samples. Through SEM investigation of nanograting formation at different pulse energies (Figure 11(a)), the nanograting formation threshold was found to be 100 nJ with 270-fs pulse duration and 250-kHz repetition rate, using an oil-immersion objective. The dependence is presented in Figure 11(b). When the laser pulse energy exceeds 100 nJ, nanograting forms. As the pulse energy continues to increase, a change in the nanograting morphology takes place. Nanograting is formed within the laser focal volume inside laser focal volume, while the size of the nanograting increases with increased pulse energy.

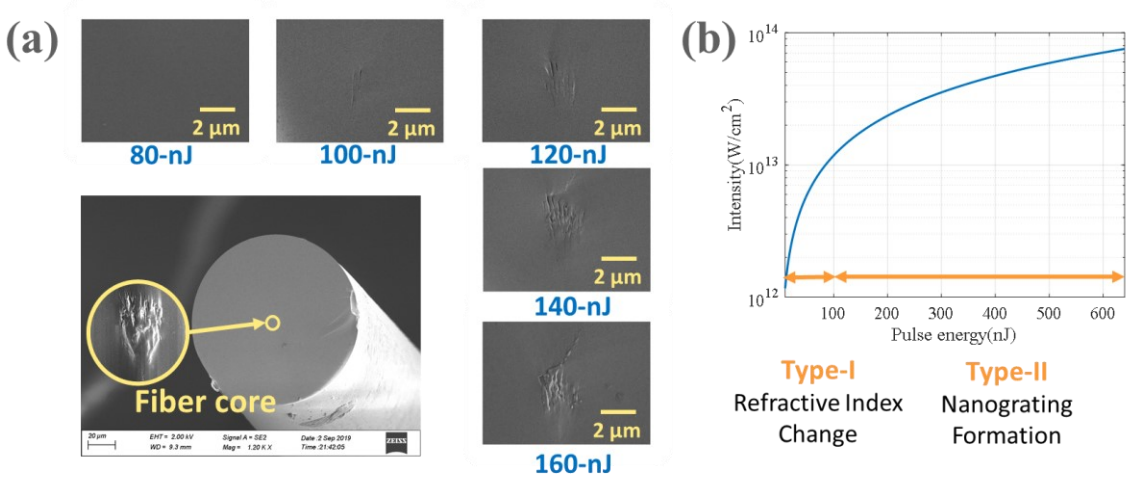

Figure 11 (a) the nanograting morphologies of the IFPI reflector in the fiber core area from overlapping pulses, inscribed with pulse energies of 80, 100, 120, 140, and 160nJ and (b) the pulse energy and intensity dependence of femtosecond laser modification regime with the current fabrication paramters. Adapted with permission from [73] **© The Optical Society.**

3.2.3 Fabrication and High-Temperature Performances

The fabrication setup is schematically shown in Figure 8(a). The Ti:sapphire regenerative femtosecond laser system was used. The laser delivers near-infrared laser pulses of 800-nm wavelength, at a fixed repetition rate of 250 kHz and pulse duration of 270 fs. A pulse energy between 80 to 600 nJ is used, adjusted by a half-waveplate and polarizer. Using a three-axis nano-precision motion stage (Aerotech ABL20020) and an imaging system, the laser beam is focused inside the center of the fiber core. To mitigate the optical aberration induced by cylindrical geometry of the optical fiber shape, an oil-immersion objective (100×, NA 1.25) and index-matching oil (n = 1.518) are used to tightly focus laser energy into the center of a fiber core.

A customized reel-to-reel laser fabrication setup is constructed for continuous fabrication of fiber sensors along an optical fiber. The setup is consisted of optical fiber reels, metal pulleys, fiber tension control structures, 3-D printed fiber supporting structures, and a nano-precision motion stage for the cross-sectional alignment. The setup was used to continuously fabricate FBGs with and without the protective polymer coatings. An Optical Frequency Domain Reflectometry-based Optical Backscattering Reflectometer (OBR) was used to monitor real-time Rayleigh backscattering profile modification of fiber under laser irradiation.

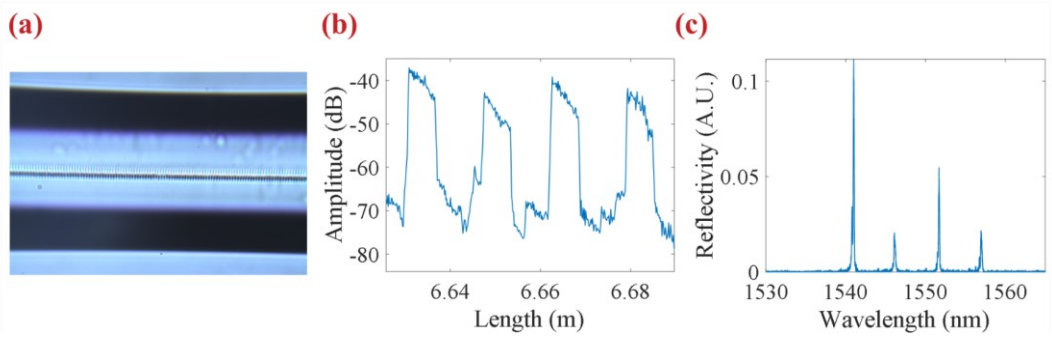

Figure 12 (a) A second-order FBG under the optical microscope, (b) the backscattering profile of four multiplexed FBGs, and (c) the spectrum of the four multiplexed FBGs.

The FBGs were fabricated using a continuous core-scanning approach. The fiber core was aligned with the laser focal spot first using a nanometer precision motion stage. The optical fiber substrate was then continuously translated in the axial direction at a constant speed of 0.1 mm/s under the irradiation of an oil-immersion objective. An acousto-optic modulator was used to pick pulses from the 250 kHz high repetition rate laser to inscribe the desired periods inside the optical fiber core. FBGs with different orders were written with 100 to 400 nJ pulse energies using a duty cycle between 10% to 75%. Figure 12(a) shows the microscopic view of a fourth-order grating inscribed inside the fiber core. Four FBGs with difference resonant wavelengths were written on

the same fiber sample. The pulse energy used was chosen to be 160 nJ to ensure the existence of nanograting. Their Rayleigh backscattering profile measured by the OBR is shown in Figure 12(b). Each FBG has a length of 1 cm. The pulse energy used was 400 nJ, while the duty cycle was set to be 20%. The spectral performances of the cascaded FBGs are recorded in Figure 12(c). The evolution of the FBG spectrum (Figure 13(a)) and the backscattering profile (Figure 13(b)) of a single fourth order FBG were tracked using the OBR. As the length of the FBG grows, the peak reflectivity grows, while the FWHW of the peak decreases.

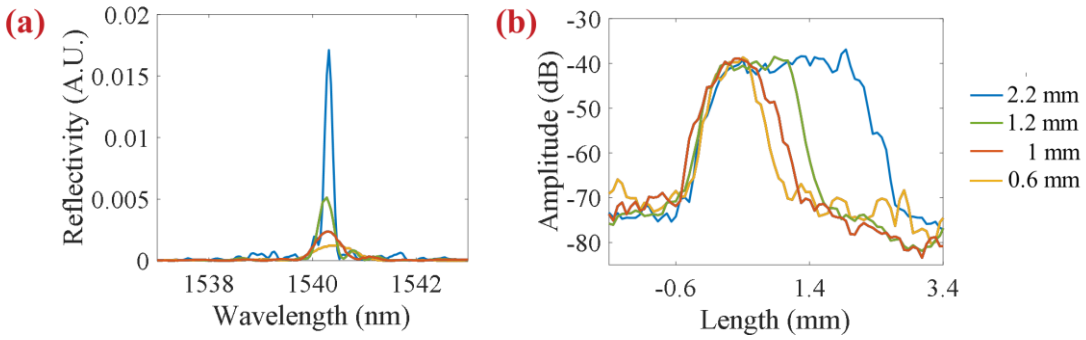

Figure 13 The evolution of point-by-point femtosecond laser direct-written FBG in time, as shown in (a) the spectral domain and (b) the Rayleigh backscattering profile in the spatial domain.

For demodulation, a broadband light from a Super-luminescent Light Emitting Diode (SLED, EXS210059-01) was coupled to the FBG sensors through a circulator. The spectrum of the reflected light was detected by a CCD-based spectrometer (Bayspec, FBGA) and transferred to a computer for dynamic demodulation. For characterization, the fiber sample was placed inside a furnace for high temperature test. Each heating cycle started from room temperature then raised to 1025°C. Figure 14(a) shows the wavelength change of the multiplexed FBGs during one single heating cycle. The temperature measurement of the FBG sensors during the heating cycle and after under 1000°C is presented in Figure 14(b).

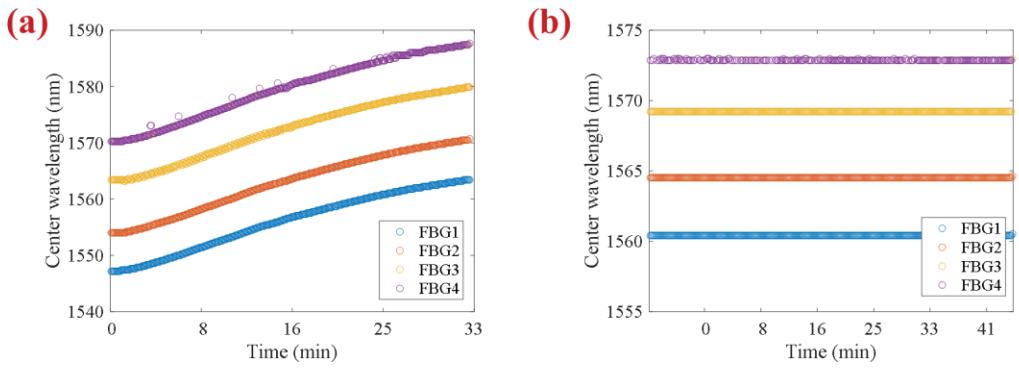

Figure 14 Temperature measurements from the multiplexed FBG sensors during (a) a heating cycle and (b) constance temperature at 1025°C.

3.3 Type-II-IR Fabry-Perot Interferometer

Compared to FBG, IFPIs are simpler in design that are composed of only a pair of reflectors. While the FBGs are demodulated in the spectral domain, IFPIs are demodulated in the spatial domain. This section presents the design, fabrication, multiplication, optimization, and measurements of IFPI sensors.

3.3.1 Operating Principle

The interference signal from the two reflectors are picked up by a white light interferometry-based demodulation method. Assuming identical reflection strength from the two reflectors. The interference spectrum of an IFPI can be expressed as a function of wavevector k, and can be expressed with the following equation:

$$I(k) = 2I_0(k + k_0)[1 + \gamma\, cos(\, 2l(k + k_0) + \varphi_0)] \qquad (3-6)$$

$I_0(k)$ is the reflection spectrum of the light source at the reflector, l is the optical path length of the IFPI cavity, γ is the fringe visibility, k_0 is the wavenumber of the spectrum's first data point, φ_0 is the phase delay of light transmits through the first reflector, which is set to zero, since the length of nanograting reflector is much shorter than the designed cavity lengths. For calculation, the envelope of the light source $I_0(k)$ is then removed for further calculation of the fringe frequency. Discretization was applied after the DC signal is removed and interpolation process:

$$I'(n) = 2\gamma\, cos(\frac{l\Delta kn}{N} + lk_0 + \varphi_0) \tag{3-7}$$

$$k = \frac{\Delta kn}{N} \;\; n = 0,1,2,3,\dots,N-1 \;\; \Delta k = k_1 - k_0 \tag{3-8}$$

The interpolated interference signal was transformed into the wavenumber domain through a Discrete Fourier Transform (DFT):

$$F(\xi) = \sum_{n=0}^{N-1} \gamma e^{i\left(\frac{l\Delta kn}{N} + lk_0 + \varphi_0\right)} e^{-2\pi i\left(\frac{n\xi}{N}\right)}$$

$$= \gamma e^{i\left(lk_0 + \varphi_0 + \pi\left(\frac{l\Delta kn}{2\pi} - \xi\right)\left(\frac{N-1}{N}\right)\right)} \frac{sin[\pi(\frac{l\Delta k}{2\pi} - \xi)]}{sin[\pi(\frac{l\Delta k}{2\pi} - \xi)/N]} \tag{3-9}$$

$F(\xi)$ is the positive half of the DFT spectrum. At the peak locations of the DFT spectrum, the peak index can be described as:

$$\xi_p = \frac{l\Delta k}{2\pi} \tag{3-10}$$

And the phase φ is:

$$\varphi\left(\frac{l\Delta k}{2\pi}\right) = lk_0 + \varphi_0 \tag{3-11}$$

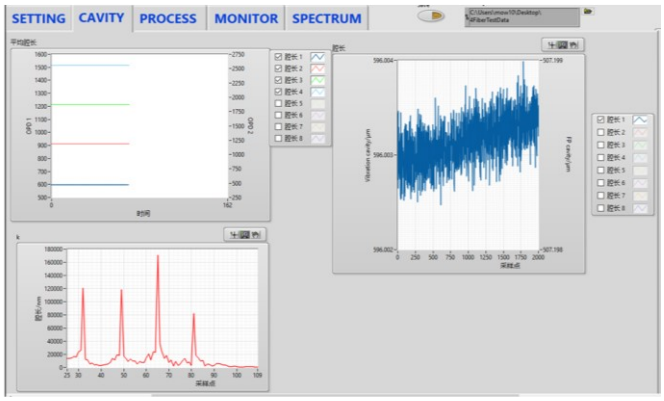

Figure 15 The LabVIEW interface showing the Graphical User Interface real-time simultaneous demodulation of temperature from four multiplexed IFPIs.

At the peak index ξp, the optical path difference and phase are:

$$l = \frac{2\pi\xi_p}{k_1 - k_0} \quad \varphi\left(\frac{l\Delta k}{2\pi}\right) = \frac{2\pi\xi_p}{k_1 - k_0} k_0 + \varphi_0 \qquad (3-12)$$

A Buneman frequency estimation is used to determine the peak location and the phase from the fringe [76], [77]. From finding the peaks in the DFT spectrum, the optical path difference (OPD) can be derived. When physical parameters, such as temperature or strain, change takes place, an increment in the OPD occurs with the increase of temperature, that can be expressed as:

$$\Delta l_{OPD} = 2\left(\frac{dn}{dT} l + \frac{dl}{dT} n\right)\Delta T = l_{OPD}(\alpha_o + \alpha_e)\Delta T \qquad (3-13)$$

α_0 is the thermo-optics coefficient of 8.6×10^{-6}/°C for the Ge doped silica core fiber, and αe is the thermal expansion coefficient, equal to 0.55×10^{-6}/°C [78]. The algorism was realized using LabVIEW. Figure 15(a) presents a screen snapshot of the graphical interface. The demodulation can be performed at a sampling rate of up to 5 kHz.

3.3.2 Fabrication

Commercially available standard telecom single-mode optical fiber (Corning SMF-28e+) was chosen as the sensor platform. The single-mode fiber reel was mounted on a customized reel-to-reel fabrication setup for translation. The fabrication process was done with the protective jacket to preserve the mechanical strength of the optical fiber. A Coherent RegA 9000 Ti:sapphire laser and amplifier system operating at 800 nm, 270 fs, and 250-kHz repetition rate was used for fabrication. Linearly polarized laser beam was tightly focused inside the core of the fiber sample through an 100× oil-immersion objective (NA 1.25) with index matching oil, to compensate for the spherical aberration at the spherical fiber shape (Figure 16(a)). Each FPI reflector was created with 25,000 femtosecond laser pulses of 160-nJ pulse energy.

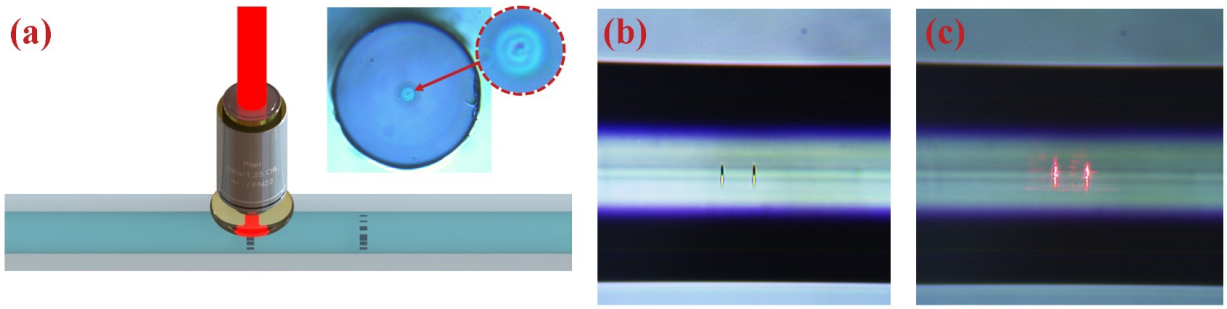

Figure 16 (a) Schematic of the IFPI fabrication setup. Inset shows the microscopic side view of the IFPI cross-section, with a modification region visible inside the single-mode fiber core, (b) microscopic photo of the IFPI sideview of two nanograting reflectors, and (c) the reflectors scattering 638 nm light. Reprinted with permission from [73] **© The Optical Society.**

Figure 16(a) inset and Figure 16(b) shows the cross-section view and side view inscribed reflector. The reflectors appear black due to the random scattering of light caused by the physical

modification at laser focus spot inside the fiber core. A 638-nm red laser light was injected to observe the scattering feature of the reflectors (Figure 16(c)). Except the core area, no physical modification could be identified except the inside the fiber core, that is a distinct feature of the highly localized femtosecond laser-material interaction. The fabrication was characterized in real-time using a commercial Rayleigh scattering-based Luna OBR4600 interrogation system. Figure 17(a) presents the Rayleigh backscattering profile of an IFPI composed of laser-induced reflectors with 1.3-mm cavity length. Femtosecond laser could induce a reflector with a 50-dB increase of the reflection signal above the intrinsic Rayleigh scattering in optical fiber. The OBR profile was used to verify the location of the inscribed points.

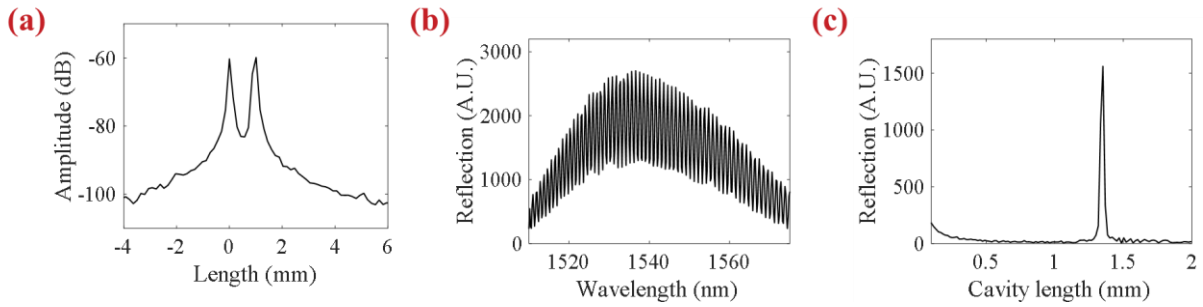

Figure 17 (a) Rayleigh backscattering profile of an IFPI using two nanograting reflectors, (b) spectrum of a single IFPI cavity, and (c) the FFT of the spectrum [73]**. Reprinted with permission from** [73] **© The Optical Society.**

After verification, a broadband method was used for IFPI characterization [79]. Broadband light centered at 1550-nm (FWHM 20 nm) from a Super-luminescent Light Emitting Diode (SLED, EXS210059-01) was coupled into the IFPI fiber sample through a circulator. The interference fringes were detected by a 512-pixel CCD-based spectrometer (Bayspec, FBGA), with a spectral range from 1510 nm to 1590 nm. IFPI fiber sample end-facet was anti-reflection

processed to eliminate the noise from Fresnel reflection. Figure 17(b) shows the spectrum of one single FPI. A Fast Fourier Transform (FFT) based white-light interferometry-based method was selected for demodulation due to its low-cost and high flexibility [79], [80]. Using non-zero-padded FFT with Buneman frequency estimation, the algorithm takes uses of both the fringe order and phase information from a single spectrum to perform accurate absolute measurement, insensitive to signal intensity fluctuations. Besides, it was able to simultaneously demodulate multiplexed FPIs from a single spectrum pattern, while the calculation speed is not related to the number of cavities to be demodulated [105-107]. The wavelength domain spectrum for the 1.3-mm was presented in Figure 17(c).

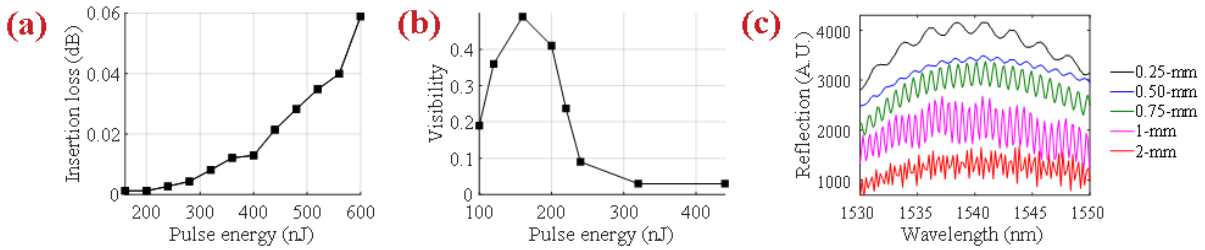

Figure 18 (a) The dependence of the insertion loss per reflector on pulse energy, (b) the dependence of a 1-mm IFPI visibility on the pulse energy, and (c) spectrums of IFPIs with different cavity lengths. Reprinted with permission from [73] **© The Optical Society.**

Single IFPI cavities with 1-mm cavity length were inscribed on the standard telecom optical fiber with different irradiation pulse energies. The dependence of fringe visibility of an IFPI of 1-mm cavity length on the laser processing parameter is presented in Figure 18(a) and (b). An inverse U-shape was observed as an optimized visibility was found at an inscription pulse energy of 160-nJ at 0.49. The reason for the peak at an intermediate pulse energy is likely due to the tradeoff between reflecting power and insertion loss. The insertion loss dependence on

fabrication condition was also characterized by measuring optical transmission power of the fiber device at 1550-nm. At each pulse energy, ten nanograting reflectors were inscribed inside the optical fiber core, and the transmission power difference was measured to calculate the insertion loss per dot (Figure 18(a)). As the size of the nanograting is smaller than the size of the optical fiber core, increasing the pulse energy increases the size of the nanograting. Thus, the insertion loss increases monotonically with laser pulse energy. This observation is consistent with the SEM studies presented in section 3.2.2 [30], [81].

The visibility of an IFPI is the contrast of the generated fringe. Figure 18(b) presents the dependence of the optimized visibility of a 1-mm IFPI written with different laser parameters. An optimized visibility takes place when the inscription pulse energy is 160 nJ. The optimized visibility occurs when reflected optical power from both reflectors are identical [47]. When the pulse energy used to fabricate the in-fiber reflectors is lower than the optimized energy, the reflected light from both reflectors are weak and are subject to the impact from continuous background Rayleigh backscattering of the pristine fiber. When the pulse energy continues to increase after the optimized energy is reached, both the insertion loss and the reflected light of the first reflector increases, leading to a decrease in the transmitted light to reach the second reflector. The fringe visibility declines as the optical power difference between reflected light from the first reflector and the second reflector becomes larger. At the optimized parameter of 160-nJ pulse energy, an insertion loss as low as 0.0012-dB per nanograting reflector can be achieved, enabling the dense multiplexing capability of IFPIs using these Rayleigh scattering centers.

The spectrums of IFPIs with different cavity lengths were demonstrated in Figure 18(c). A cavity length as long as 2-mm could be clearly demodulated from the algorism. Using the optimal parameter found using the above-mentioned method, IFPIs with different cavity lengths were

fabricated on a single-mode fiber with 1-cm spacing. Figure 19 presents the multiplexation of different numbers of IFPIs on an optical fiber sample, using the 160 nJ inscription pulse energy. Up to 20 IFPIs could be inscribed, with ~100 µm cavity lengths spacing, and clearly identified in the FFT domain suing the fast white-light demodulation algorism.

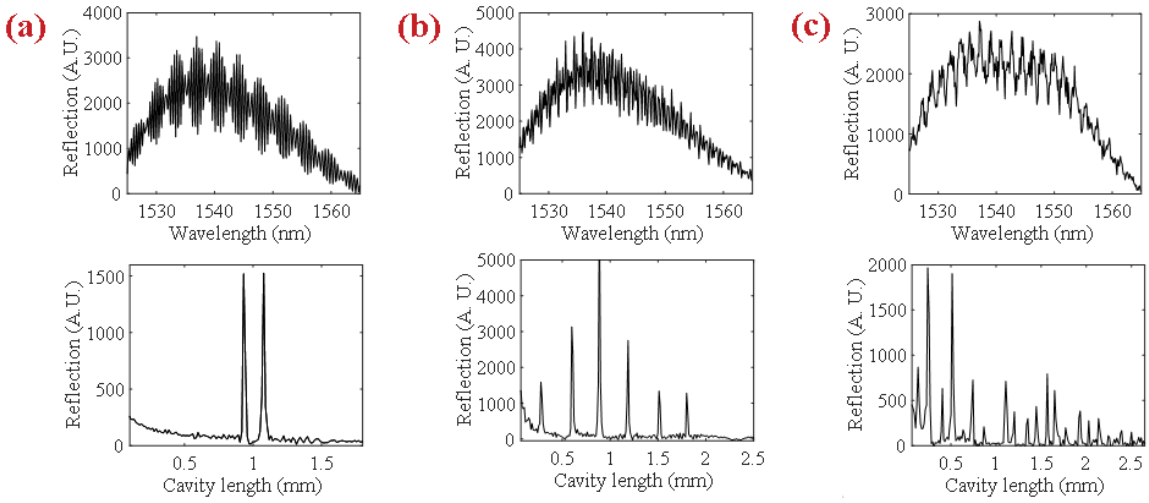

Figure 19 The spectrums and FFT spatial domain of (a) two multiplexed IFPIs, (b) six multiplexed IFPIs, and (c) twenty multiplexed IFPIs.

3.3.3 High-Temperature Performances

A single IFPI sensor with 1346.9-µm cavity length fabricated using 160-nJ pulse energy was placed inside a box furnace for high temperature stability test. The cavity length was demodulated using a fast white-light algorism with a sampling time of every 1 second. The backscattering profile, wavelength spectrum, and FFT transform into the wavevector domain are presented in Figure 20(a), (c), and (d). The fiber sensor was first annealed at 1000°C for 5 hours, then went through repeated heating and cooling cycles. Each heating cycle started from room

temperature then raised to 1000°C in a step of 100°C at 5°C/min ramp rate, holding 1 hour at a steady temperature at each step of 100°C. The temperature of the furnace was continuously tracked by a type-K thermocouple with USB temperature logger (Lascar EL-USB-LCD) every 20 seconds. Afterwards, the sample was cooled down in furnace at natural cooling rate. The cavity length was calculated with respect to the electronic thermocouple measurement to obtain the characterization curve in Figure 20(a). The sensitivity was 11.1-nm/ at a temperature below 300°C and 14.4-nm/°C at a temperature above 300°C, similar to the behavior reported previously for high temperature measurements for FPIs and FBGs [82], [83]. Figure 20(b) presents the measured FPI temperature against the thermocouple measurements, using the obtained characterization curve, showing the precise sensor response of the IFPIs during the repeated heating and cooling cycles.

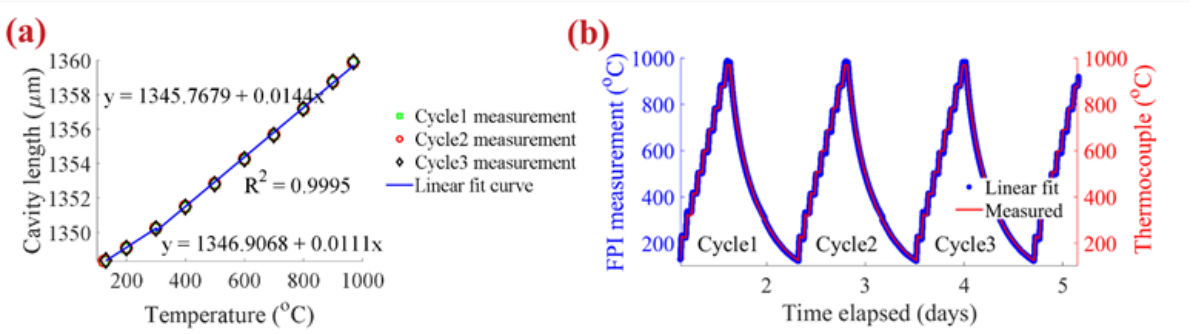

Figure 20 (a) Temperature response and linear fit curve of a single IFPI sensor and (b) FPI measurement results and the thermocouple measurement during the first three three repetitive heating cycles. Reprinted with permission from [73] **© The Optical Society.**

Two cascaded IFPIs were fabricated to characterize the crosstalk of multiplexed fiber sensors fabricated using the nanograting reflectors. A single-mode fiber was translated along the axial direction using a customized reel-to-reel setup, to inscribe nanograting points as IFPI sensor array at points of interest, using the optimized pulse energy of 160-nJ. Two IFPIs were inscribed

on a single-mode optical fiber, with cavity lengths of 934.9-μm (Sensor1) and 1050.2-μm (Sensor2). Figure 21(a) shows the wavelength spectrum and the FFT wavevector domain of the two sensors. The two peaks are distinguishable in the wavevector domain. Sensor 1 was placed under constant room temperature in the lab, while Sensor 2 was placed inside a furnace. The temperature of the furnace was increased from room temperature to 500°C at a fast ramp rate of 10°C/min. The cavity lengths change was demodulated in real time. Figure 21(b) shows the cavity length change during the whole crosstalk measurement process, while Figure 21(c) presents the details when both IFPI sensors were kept at room temperature (top) and when Sensor 2 was at 500°C and Sensor 1 was kept at room temperature (bottom). Some crosstalk and noise were observed due to the rapid temperature increase. However, while an over 5-μm cavity length increase was observed in Sensor 2 due to the thermo-expansion caused by temperature increase, the cavity length change of Sensor 1 was negligible. The temperature of Sensor 1 fluctuated a little bit, this was probably due to the fluctuation of the lab temperatures.

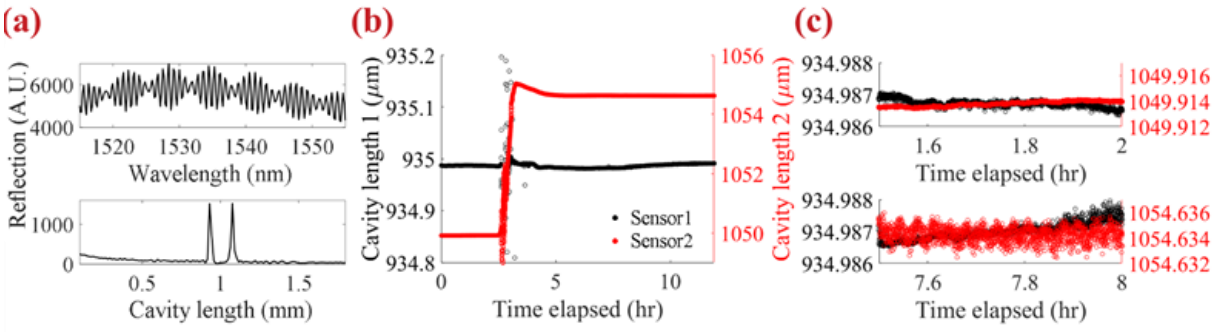

Figure 21 (a) Top: spectrum of the two multiplexed IFPIs and Bottom: the FFT of the IFPIs, and (b) the cavity change of the IFPIs during the measurement when both Sensor 1 (black, right axis) and Sensor 2 (red, left axis) were placed at room-temperature (top subplot) and when Sensor 1 stayed at room-temperature while Sensor 2 was kept at 500 °C (bottom subplot). Reprinted with permission from [73] **© The Optical Society.**

To demonstrate the multiplexing capability, a string of six IFPI sensors were inscribed on a single-mode fiber sample. Since the crosstalk experiment in Figure 22 demonstrates that the sensor cavity length difference of 115-μm could not introduce identifiable crosstalk. We designed the cavity lengths to be 398, 599, 888, 1190, 1527, and 1814-μm, respectively for the multiplexed IFPIs. A 1-cm spacing between two adjacent sensors was chosen in order to locate the IFPIs at different positions inside our box furnace. The location and reflection strength of the nanograting reflectors were characterized by the OBR-measured backscattering profile in Figure 22(a). The interference fringe and the FFT transform is shown in the wavevector domain of the multiplexed sensors are shown in Figure 22(b) and (c). The six IFPI peaks are highly distinguishable in the FFT domain.

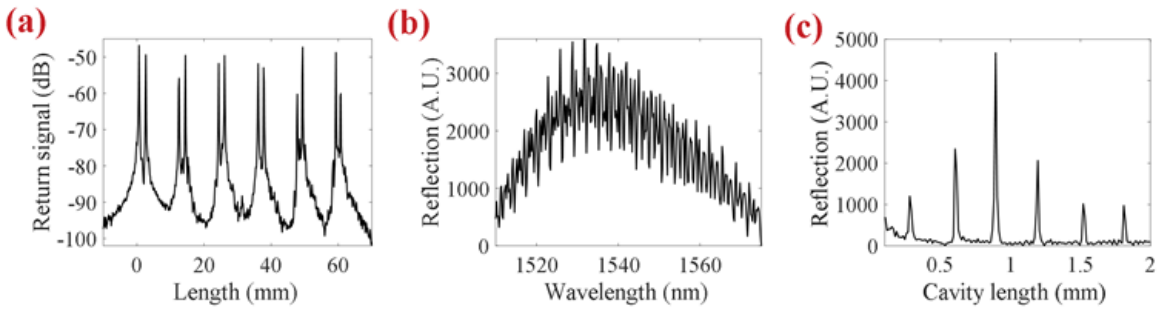

Figure 22 (a) Rayleigh backscattering profile of the multiplexed IFPIs, (b) spectrum of a multiplexed IFPI cavity, and (c) the FFT of the spectrum. Reprinted with permission from [73] **© The Optical Society.**

Similar to the high-temperature performance test for the single IFPIs, the multiplexed IFPIs were first annealed, then went through repeated heating and cooling cycles. Again, each heating cycle started from room temperature and heated up to 1000°C at a speed of 5°C/min, holding 1 hour at each step of 100°C. The furnace temperature was tracked using an electronic temperature data logger while cavity lengths of the IFPIs were demodulated and recorded every 1 second. The

calibration curves shown in Figure 23(a)-(f) exhibit linear relationship between cavity length and temperatures for each of the six multiplexed IFPIs. The temperature sensitivity of sensors obtained from the linear fitting are 3.71, 5.66, 8.39, 11.15, 14.28, and 17.15-nm/°C for the cavity lengths of 398, 599, 888, 1190, 1527, and 1814-µm, respectively. Taken these sensitivities back to Equation (3-13), the experimental data is consistent with the theoretical thermal expansion. Using these calibrations curves, temperature measured by these IFPIs are compared against measurement performed by the thermocouple in a box furnace for the third heating cycle (Figure 23(g)).

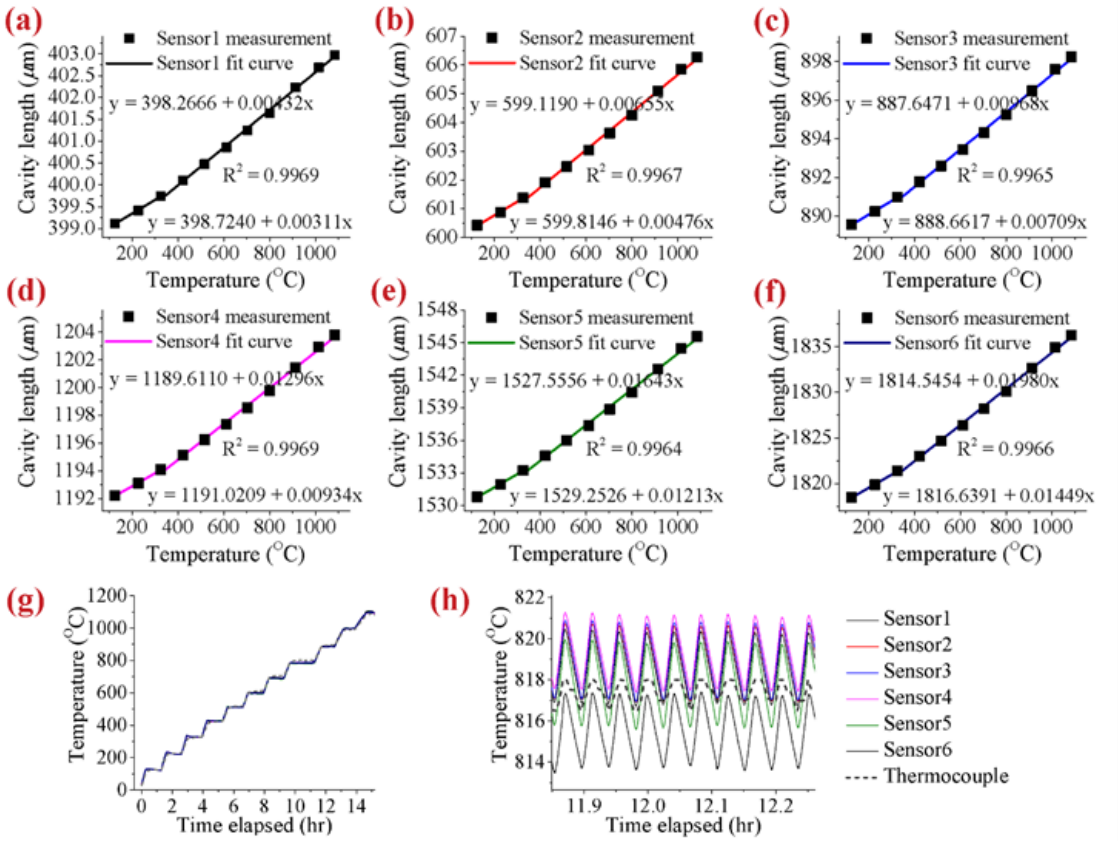

Figure 23 (a-f) Linear fit curves of the six cascaded IFPI sensors, (g) The demodulated response of cascaded IFPI sensors at furnace temperature of 817°C. Reprinted with permission from [73] **© The Optical Society.**

Figure 23(h) presents a zoomed-in area in Figure 23(g) when the temperature of the box furnace was held around 817°C. The thermocouple sensor measurement shows a periodic temperature fluctuation, caused by the PID control for the furnace's temperature modulation. The measurement from the six multiplexed IFPI sensors traces that of the thermocouple. While the temperature variation inside the box furnace is highly inhomogeneous, the IFPI sensors measured a different temperature depending on their position inside the furnace, while the overall trend is consistent with the thermocouple.

4.0 Femtosecond Laser Fabrication of Distributed Fiber Sensors

Distributed sensing is a unique characteristic of optical fiber sensors. Through utilizing the intrinsic scattering inside fiber core, one single fiber can be equivalent to thousands of electronic point sensor devices. Distributed tracking of the measurands, such as temperature, strain, and vibration can be achieved at a high spatial resolution of sub-centimeter on an unmodified optical fiber. However, the intrinsic scattering signal is usually weak inside the commercial optical fibers, as it induces undesirable loss. This limits the Signal-to-Noise Ratio (SNR) of the fiber sensor. Moreover, while many industrial applications demand robust operation under challenging environments, the intrinsic scattering is vulnerable to harsh environmental conditions such as high temperature and radiation. Femtosecond laser fabrication is able to address these challenges and improve the stability of optical fiber sensors under harsh environments. Chapter 4 describes the continuous femtosecond laser inscription of low-loss artificial scattering centers in commercially available silica and sapphire optical fiber core to form distributed sensors for distributed temperature. Long-term high-temperature performance was successfully demonstrated with improved thermal stability.

4.1 Motivation and Background

Distributed sensing is a unique property of optical fiber sensors. Through exploiting the intrinsic scattering phenomenon happening inside an optical fiber, namely Raman, Brillouin, or Rayleigh scattering, physical parameter change can be extracted from different positions along an

optical fiber. Rayleigh scattering is the strongest scattering amongst others inside an optical fiber. It takes place at particle size much smaller than the wavelength, usually due to the inhomogeneity induced inside a fiber during manufacturing. Rayleigh scattering is a kind of elastic scattering, meaning there is no energy loss during the process, and thus, the laser wavelength does not change. Through the extraction of the Rayleigh backscattering signal amplitude from different fiber locations, distributed sensing can be achieved. Currently, several types of Rayleigh scattering-based distributed optical fiber sensing technologies are available commercially [84]–[87].

The first of the many distributed sensing techniques is the Optical Time-Domain Reflectometry (OTDR). OTDR was first proposed in 1977 by Barnoski et al. to monitor the attenuation along an optical fiber [88]. The algorism uses a pulsed laser and tracks the time delay of the backscattered signal from the Fiber Under Test (FUT). One drawback of the OTDR is the spatial resolution, which is limited by the pulse duration and power limitation of the laser source. In contrast, the Optical Frequency-Domain Reflectometry (OFDR), developed in 1998 by Froggatt and Moore, can significantly increase the spatial resolution of the Rayleigh scattering-based distributed sensing [89]. The system is composed of a Tunable Laser Source and an interference-based detection system, consist of Mach-Zehnder Interferometers. The backscattered signal from the FUT is sampled across a frequency range, then FFT was performed to transfer the signal into the spatial domain. Interrogation system using OFDR can achieve high spatial resolution of 10s micrometers, making the technology a perfect candidate for high precision distributed sensing applications.

The challenge of Rayleigh scattering-based distributed sensing is that scattering is minimized by optimized processes of fabrication for commercial optical fiber, as it induces undesired loss in fiber communication. As a result, the performance of Rayleigh scattering-based

distributed fiber sensors is limited by the weak signals generated from Rayleigh scattering. To address this challenge, UV laser is used to create artificial Rayleigh scattering centers in photosensitized or photosensitive optical fiber enhances. Previous work has demonstrated that increased Rayleigh scattering signal led to improved performance in OFDR-based distributed temperature and strain sensing. The UV-enhanced distributed fiber strain sensors have also been used in medical applications for shape sensing [90]–[92]. Despite these improvements, the UV inscription process requires specialty photosensitive fibers or additional pre-processing steps such as hydrogen loading. Moreover, the performance of the UV sensor would degrade at extreme temperatures, making it less suitable for applications in harsh environments.

The femtosecond laser has emerged as a promising technique in the fabrication of fiber sensors, especially for use in harsh environments. Random gratings induced by femtosecond laser direct writing have been reported to enhance the scattering signal for application in OFDR-based distributed temperature sensing. By varying either the fiber writing speed or laser repetition rate, random gratings can be generated to increase the sensing accuracy [93], [94]. However, the random grating with ultra-low loss was generated by the femtosecond laser-induced homogeneous refractive index change (Type-I-fs), and thus is not suitable for long-term monitoring at a high temperature range. Meanwhile, at a higher inscription pulse energy, another femtosecond laser-material interaction regime takes place, characterized by the formation of high-temperature stable nanostructures (Type-II-fs) that has exhibited exceptional harsh environment endurance over 1000°C.

First observed in 2003, the femtosecond laser induced nanograting is widely used for femtosecond laser selective etching for microfluidic channels and FBGs for harsh environment applications. Previous microscopy studies demonstrate that nanograting is formed with periodical

nanocracks that consist of nanopores of 10s nanometers in size, which is likely due to the SiO_2 decomposition caused by laser-induced electron plasma [95], [96]. Rayleigh scattering takes place due to inhomogeneities inside the fiber core with a feature size much smaller than the wavelength. The nanopores formed by laser irradiation provide additional scattering structures that generate stronger Rayleigh backscattering signals than those in unmodified fibers, which lead to improved SNR for fiber sensors [97]. The nanopores formed by laser irradiation provide additional scattering structures that generate stronger Rayleigh backscattering signals than those in unmodified fibers, which lead to improved SNR for fiber sensors [98]. Both Type-II laser modifications and associated anisotropic scattering characteristics have been studied as a function of wavelength. Previous literature has demonstrated that Rayleigh scattering and Mie scattering can account for increased nanograting induced scattering loss intensity [99]–[101]. Recently, high-temperature stable sensors that exploit femtosecond laser-induced nanograting as Rayleigh scattering centers, were tested in a reactive hydrogen gas environment with temperatures up to 800°C. The Rayleigh enhanced section has proven to be functional in both nuclear reactor cores and internal to solid oxide fuel cells. However, the sensors suffer from high propagation loss of 0.15 dB/cm, thus, the sensing range is limited. Moreover, normal fibers are vulnerable to the intense neutral flux and suffers from low scattering signal. To address these challenges, this chapter presents a novel method of reel-to-reel femtosecond laser direct writing method that enhances Rayleigh scattering on both silica-core and sapphire optical fiber for distributed temperature sensing. By studying the correlation between the Rayleigh scattering profile and the femtosecond laser-induced high-temperature stable nanograting in fiber core at the Rayleigh enhanced section, a method to fine-tune the fabrication conditions to produce meters of optical fibers with an enhanced Rayleigh scattering profile and low propagation loss.

4.2 Optical Frequency Domain-Reflectometry Operating Principle

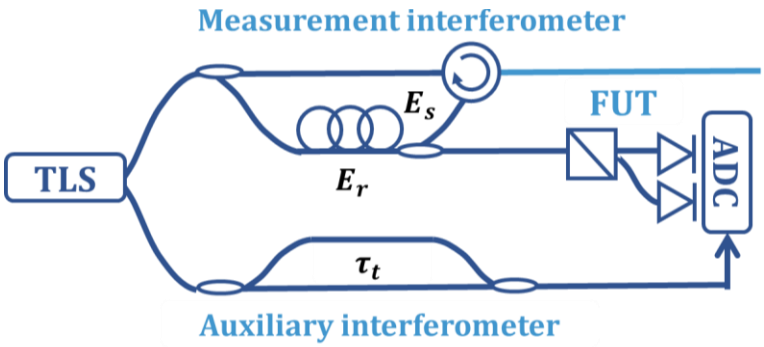

Figure 24 Schematic of the OFDR optical network for Rayleigh scattering measurement. FC: fiber couple; PC: polarization controller; PBS: polarization beam splitter; PD: photodetector; ADC: analog-to-digital converter.

A typical Optical Frequency Domain Reflectometry (OFDR) system is demonstrated in Figure 24. The system contains a Tunable Laser Source (TLS), Mach-Zehnder Interferometers (MZI), and Photodetectors (PD) [102]. The swept-wavelength coherent interferometry technique to tune the frequency of the light source linearly with time. When the laser is swept at a rate of γ, the frequency of the light can be expressed as:

$$w(t) = w_0 + \gamma t \qquad (4-1)$$

The light from the TLS is unevenly split into two paths - an auxiliary interferometer and a measurement interferometer. The upper side of Figure 24 shows an MZI. Light at the measurement interferometer is again split into a measurement arm and a reference arm. The Rayleigh backscattering signal from the FUT will merge into the measurement arm signal from the circulator. Then the combined signal of the measurement arm and the reference arm will be

split again with a polarization beam splitter and picked up by photodetectors. To start with, the input light from the TLS can be expressed as:

$$E_{in} = E_0(t)e^{-iw(t)t} \quad (4-2)$$

$w(t)$ is the instantaneous angular frequency. Then, the recombined interference signal of the measurement and reference arm can be expressed as:

$$E_r = E_0(t+\tau_1)e^{-iw(t+\tau_1)t} \quad (4-3)$$

$$E_s = E_0(t+\tau_2)e^{-iw(t+\tau_2)t} \quad (4-4)$$

τ1 and τ2 are the time delay from the reference arm and the measurement arm. Assume that the backscattered Rayleigh signal from the FUT has an amplitude gain ρ(w) and phase change φ(w), the field of the scattered time at the recombined coupler, the total light field and the measurement arm, and the measured light field intensity at the photodetector can be expressed with the following equations:

$$E_R = E_0(t+\tau_2)\rho(w)e^{-iw(t+\tau_2)t+i\varphi(w)} \quad (4-5)$$

$$E_{out} = E_r + E_R = E_0(t+\tau_1)e^{-iw(t+\tau_1)t} + E_0(t+\tau_2)\rho(w)e^{-iw(t+\tau_2)t+i\varphi(w)} \quad (4-6)$$

$$I_{out} = |E_0(t)|^2 + |E_0(t-\tau)\rho(w)|^2 + 2\rho(w)E_0(t)E_0(t-\tau)\,cos[w(t)\tau - \varphi(w)] \quad (4-7)$$

$\tau = \tau_1 - \tau_2 = 2nl/c$ is the time delay between the reference arm and the measurement arm, that is the time delay at length l of the FUT. In this case, the backscattered signal from the FUT can be extracted from the frequency domain signal. The temporal response from the can be obtained from Fourier Transform the frequency domain signal:

$$I(\tau) = I\left(n\frac{\Delta l}{c}\right) = FFT[I(w)] \quad (4-8)$$

The spatial resolution is equivalent to the time domain resolution, that is limited by the spectral bandwidth of the tunable laser source:

$$\Delta z = \frac{\lambda_S \lambda_f}{2n_g \Delta\lambda} \cong \frac{c}{2n_g \Delta f} \qquad (4-9)$$

$$\Delta f = \frac{\lambda_S \lambda_f}{\Delta\lambda} \qquad (4-10)$$

λ_S and λ_f are the start and end wavelength of the laser source. n_g is the refractive index of the FUT. Thus, the spatial resolution is related to the wavelength sweeping range of the coherent light source. A scanning range from 1535 nm to 1575 nm corresponds to 20 μm spatial resolution. Moreover, the maximum detection length L_{max} is determined by the sampling rate and the tunable laser rate:

$$L = \frac{c}{4n_g} \frac{f_S}{\gamma} \frac{c\tau_g}{4n_g}_{max} \qquad (4-11)$$

f_s is the sampling rate, triggered by the auxiliary interferometer for each tunable laser sweep. f_s is related to the differential delay in the unbalanced auxiliary interferometer τ_g and the laser sweep rate with $f_S = \gamma\tau_g$. An 800 nm wavelength, the differential delay is equivalent to a 40 m detection range. It should be noted that the maximum detection length is also limited by the coherence length of the light source.

To sense the temperature signal, a cross-correlation calculation is performed along a gauge length for each section along the FUT defined by the measurement spatial resolution. The spectral shift of each section between the reference arm and the measurement arm is proportional to the temperature or strain change. Ideally, Rayleigh scattering is independent to the physical parameter change in an optical fiber, and thus, the cross-correlation is only sensitive to the temperature or

strain change. A reference signal was first taken when the fiber is undisturbed, then the temperature or strain change along the fiber can be determined by the cross-correlation between the current measurement with the reference:

$$-\frac{\Delta\nu}{\nu} = \frac{\Delta\lambda}{\lambda} = K_T\Delta T + K_\varepsilon\Delta\varepsilon \qquad (4-12)$$

where $K_T = 6.45 \times 10^{6\circ}C^{-1}$ ad $K_e = 0.780$ are the temperature and strain coefficient for most germane-silicate core fibers. The temperature and strain resolution are constrained by:

$$\Delta L(K_T\Delta T) = \Delta L(K_\varepsilon\Delta\varepsilon) = \frac{\lambda}{4n} \qquad (4-13)$$

The measurement resolution can be increased by decreasing the gauge length of the cross-correlation. However, the decrease of the gauge length will also decrease the SNR of the measurement. Usually, a temperature resolution of 0.1°C or strain resolution of 1 με can be achieved by 1 cm gauge length.

4.3 Femtosecond Laser Sensor Fabrication

A Coherent Ti:sapphire regenerative femtosecond laser system was used for fiber sensor fabrication, focusing 800-nm, 270-fs, and 250-kHz light through a 100× 1.25-NA oil-immersion objective. The spot of laser focus was aligned with the center of the optical fiber core with the help of a high-precision motorized stage (Aerotech ABL20020). To achieve continuous femtosecond laser inscription, the fiber was translated using a customized reel-to-reel setup at a constant speed. Laser beam is linearly polarized, with its direction of polarization perpendicular to the direction of

fiber translation. The backscattering behavior of the fiber sample was probed using the Luna 4600 OBR system, as illustrated schematically in Figure 25(a).

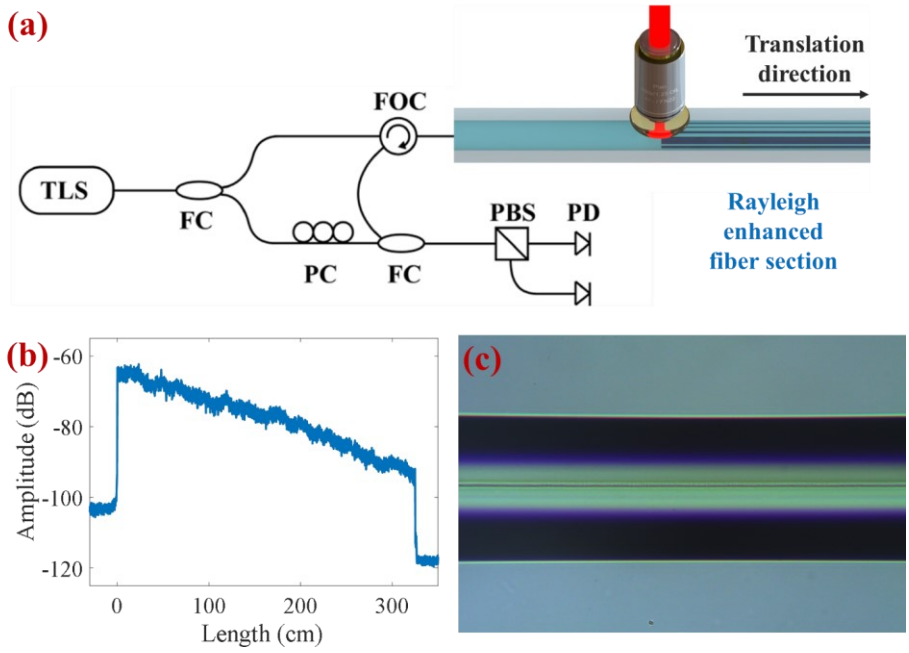

Figure 25 (a) Schematic of the fabrication setup, (b) the Rayleigh backscattering profile of a 325-cm Rayleigh enhanced section, and (c) the microscopic photo of the fiber sideview [103]**. © Copyright 2020 IEEE.**

An example of the OBR backscattering profile of a Rayleigh enhanced section that is over 3 meters long is presented in Figure 25(b). Using the same reel-to-reel fabricated setup described in Chapter 3, the inscription of meters of fiber sensor were enabled with simple alignment procedure. Figure 25(c) shows the sideview of the Rayleigh enhanced section under the optical microscope, with a continuous modification track in the center of the fiber core. A pulse energy of higher than 100 nJ was used to ensure the existence of nanograting at the laser written region, as discussed in section 3.2. The Rayleigh enhanced section was cleaved afterwards at the section of

femtosecond laser modification to confirm the formation nanograting at the fiber core using the SEM, that is high-temperature stable up to 1100°C [45], [49].

4.4 Mechanisms and Optimization

SEM studies of nanograting formation in correlation to the Rayleigh backscattering profile provide tell-tale clues on how to further optimize the fabrication process. Figure 26 show the OBR measured backscattering profiles of Rayleigh enhanced sections on a standard silica-core single-mode optical fiber (Corning SMF28e+) written with 160, 140, 120, 100, and 80-nJ inscription laser pulse energies, at a constant speed of 0.5 mm/s, while their SEM photos revealed significant cross-section morphology variations in correlation to the OBR profiles.

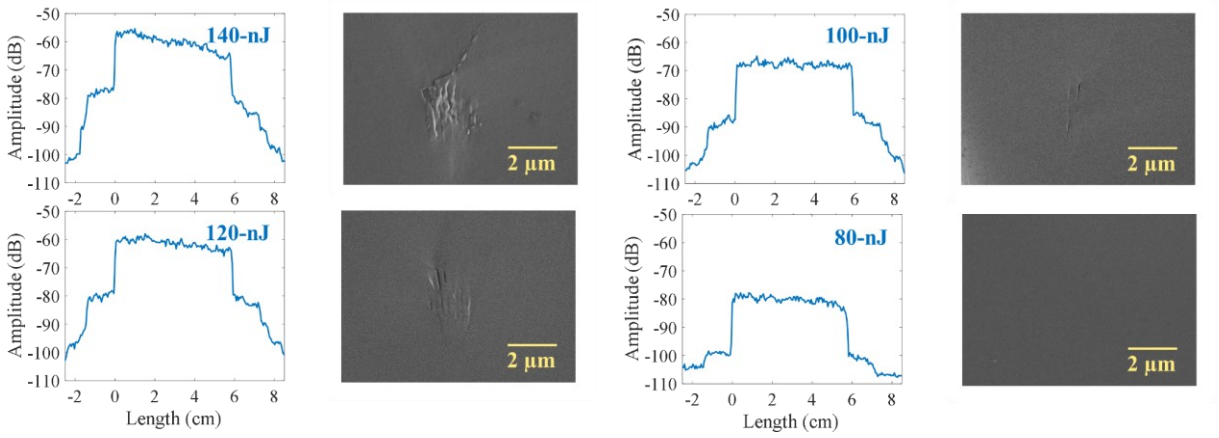

Figure 26 (a-e) Rayleigh backscattering profiles and (f-j) SEM photos of fiber core cross-section morphology of the Rayleigh enhanced sections fabricated using pulse energies 160, 140, 120, 100, and 80 nJ, respectively.

At a pulse energy below 60-nJ, no change in the Rayleigh backscattering profile could be measured, since the pulse energy is lower than the threshold of making Type I refractive index

change in the fiber. At a pulse energy between 60 nJ and 100 nJ, an increase in the backscattering signal occurred, while there was no visible morphology modification (Figure 26(j)). This is the regime where the multiphoton absorption process induces a low-loss homogeneous refractive index modification, that is typically used to fabricate waveguide for integrated photonic circuit. Loss can be identified in Figure 26(e). This can be explained by the localized refractive index change modification region with the size much smaller than the fiber core, resulting in a coupling loss due to the mismatch between the femtosecond laser induced waveguide-like structure and the fundamental mode of the optical fiber. When pulse energy was higher than 100 nJ, an anisotropic nanostructure was observed in the fiber core (Figure 26(f-i)), indicating the regime of laser-induced nanograting formation.

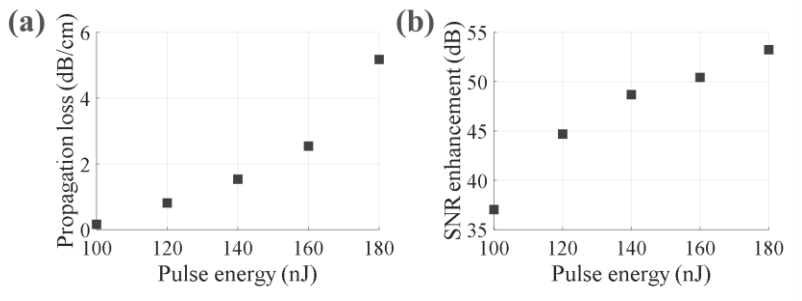

Figure 27 Dependence of (a) propagation loss and (b) SNR enhancement on the femtosecond laser exposure conditions [103]**. © Copyright 2020 IEEE.**

Figure 27 summarizes the dependence of OBR-measured propagation loss and SNR enhancement on the fabrication pulse energy at the pulse energies that allows the formation of high-temperature stable nanograting. The propagation loss is calculated from the linear fit of the optical OBR measured return loss [104], [105], and the SNR enhancement is measured from the increase in returned backscattering signal of the Rayleigh enhanced fiber section as compared to

the unmodified fiber section, where only intrinsic Rayleigh scattering exists. A general relationship that is revealed from the OBR profile suggests that with an increase in laser pulse energy, both the SNR enhancement and the propagation loss increase. This is consistent with the SEM observations (Figure 26(f-i)), showing an increased size of the nanograting with increasing pulse energy.

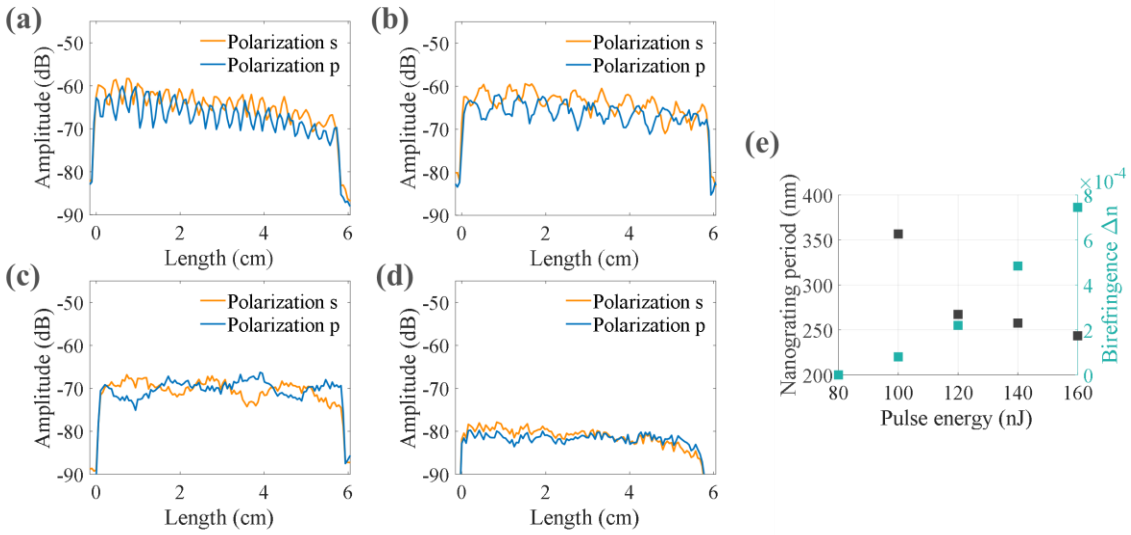

Figure 28 The s and p polarization states of the OBR-measured Rayleigh backscattering profiles, written with pulse energies of (a) 140-nJ, (b) 120-nJ, (c) 100-nJ, and (d) 80-nJ, respectively [103]**, and (e) the dependence of nanograting period and the birefringence on the laser pulse energy. © Copyright 2020 IEEE.**

The controllability of loss and enhancement on pulse energy is a result of the distortion-free oil-immersion objective used during the fabrication process. Because of the high Numerical Aperture of the objective, the laser-induced nanograting size is much smaller than the size of the fiber core, and thus, the larger physical modification caused by nanograting increases the size of inhomogeneity inside the fiber core, resulting in a higher Rayleigh backscattering signal and scattering loss measured at the interrogator. As such, precise tuning of the Rayleigh enhanced section is enabled. By optimizing the conditions of laser exposure, the optimized exposure

condition in SMF28e+ was found at 100-nJ, with a minimum loss of 0.01-dB/cm and an SNR enhancement of over 35-dB. This can be explained by the relatively small nanograting size formed at 100-nJ pulse energy (Figure 26(i)), especially since 100-nJ is close to the threshold energy between the femtosecond laser-induced refractive index modification regime and the nanograting formation regime.

Due to its asymmetric morphology, birefringence is introduced in optical fiber core during the formation of nanograting. By simultaneously monitoring the two orthogonal s and p polarization states in the OBR-measured Rayleigh backscattering profile, the formation of nanograting can be identified using a non-invasive approach during fabrication. Figure 11(a-d) show polarization states of the Rayleigh enhanced section written with a pulse energy of 140, 120, 100, and 80-nJ, respectively. No preference in polarization can be seen at 80-nJ (Figure 28(d)), indicating the material modification is in the regime of isotropic positive refractive index change, consistent with the SEM observation in Figure 26(j). Meanwhile, as pulse energy reaches 100-nJ and beyond, beating occurs in the two polarizations. The birefringence of 140, 120, and 100-nJ profiles (Figure 28 (a-c)) were calculated to be 9.9×10^{-4}, 2.7×10^{-4}, and 0.8×10^{-4} [102], [104], respectively, which is due to the increased birefringent nanograting size (Fig. 2(g-i)). Compared to the low birefringence of $\sim 10^{-7}$ for unmodified single-mode optical fiber (Corning SMF28e+), the scattering centers produce an approximate increase of three orders of magnitude in the in-fiber birefringence, which is consistent with previous descriptions of the in-fiber birefringence induced by nanograting [106], [107].

4.5 High-Temperature Performances

For high-temperature stability test, a Rayleigh enhanced section fabricated with 100-nJ pulse energy and 1-mm/s speed was first annealed at 1000°C for 20 hours and subjected to repeated heating and cooling cycles. Each cycle started from the ambient temperature, then rose to 1000°C at a rate of 5°C/min, remaining stable at each step of 100°C for 1-hour, followed by cooling at the natural rate from 1000°C back to the ambient. The temperature inside the box furnace was monitored with a Type-K thermocouple, and the Rayleigh enhanced sample was examined using the OBR every 10 min with 0.5-cm spatial resolution.

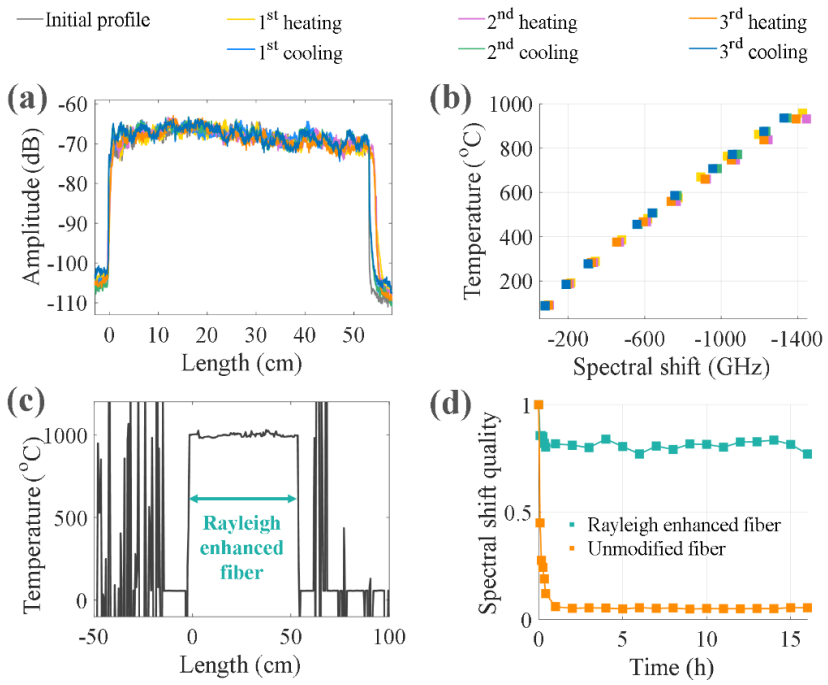

Figure 29 (a) The Rayleigh backscattering profile change and (b) the characterization curve during high-temperature test cycles, and (c) the temperature measurement after three temperature cycles and 16 hours at 1000°C, and (d) the spectral shift quality change of the Rayleigh enhanced fiber section and unmodified fiber during 16 hours [103]**. © Copyright 2020 IEEE.**

Figure 12(a) shows the profile change right after the fabrication, after annealing, and during each heating and cooling cycle. The characteristic curve for each cycle was calculated (Figure 29 (b)), as the sensitivity was measured to be -0.66 GHz/°C. The sensor was thermally stable throughout the temperature cycling, with no obvious change in the backscattering profile. Afterwards, the Rayleigh enhanced section was kept at a constant temperature of 1000°C for 16 hours, in order to verify the long-term thermal stability of the sensor. After 16 hours, it was still able to keep deriving correct temperature measurements from the Rayleigh enhanced section, using the ambient temperature profile as a reference, while the performance of the unmodified optical fiber degraded at 1000°C (Figure 29 (c)). This is probably due to the nanograting induced permanent physical modification exhibits better thermal stability at 1000°C than the intrinsic Rayleigh backscattering signal caused by inhomogeneities in fiber core.

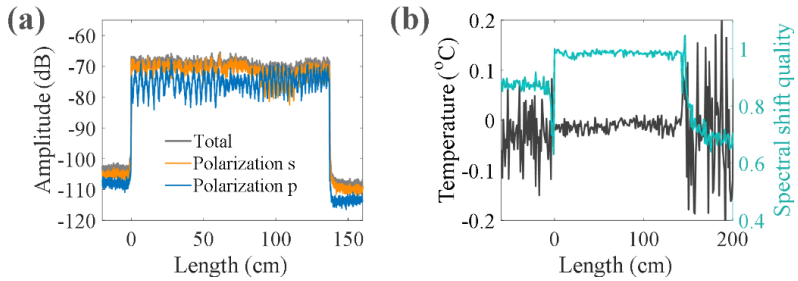

Figure 30 (a) The Rayleigh backscattering profile of a 137-cm Rayleigh enhanced section and (b) the OBR-measured temperature variation (right) and spectral shift quality (left) at room temperature [103]. **© Copyright 2020 IEEE.**

Figure 29 (d) represents the averaged spectral shift quality of both the Rayleigh enhanced fiber section and the unmodified fiber section over the time period of 16 hours at 1000°C, using the profile at the 0 hour at 1000°C as a reference. The range of spectral quality is a number between 0 and 1, which evaluates the quality of the cross-correlation in OFDR-based sensing [84], [108],

[109]. Overall, the Rayleigh enhanced section exhibited significantly improved high-temperature stability over a long term. With a combination of laser exposure tuning and reel-to-reel fabrication, a 137-cm Rayleigh enhancement section was written with 35-dB Rayleigh backscattering enhancement and 0.01-dB/cm loss (Figure 30(a)). The fiber sample was placed inside a thermally insolated container for 12 hours. Spectral shift quality of the Rayleigh enhanced section exhibits superior performance and the RMS noise was measured to be 0.012°C, about four times better than the unmodified sections measured to be at 0.054°C (Figure 30(b)).

Radiation resilience of the femtosecond laser enhanced fiber samples was carried out with collaborated work with MIT Research Nuclear Reactor. Rayleigh enhanced fiber region was placed in a radiation reactor at a steady temperature of above 600°C and with fast neuron flux above 1×10^{14} n/s/cm^2. Figure 31 shows temperature measurement after 29 days of radiation. While the backscattering profile of the un-irradiated fiber region changed from the radiation of fast neutron, the temperature profile of the femtosecond processed region traces the constant surrounding temperature.

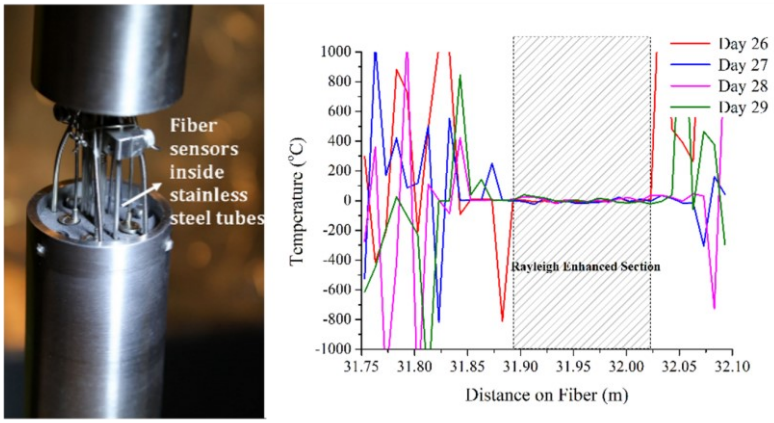

Figure 31 Nuclear setup (left) Rayleigh backscattering temporal profile (right).

4.6 Other Types of Silica-Core Optical Fibers

The versatility of femtosecond laser direct writing technique was demonstrated on different types of silica-core optical fibers in this section. Many laser manufacturing techniques, such as the UV laser fabrication, require specialty photosensitized optical fiber. The processed fiber substrate needs to be either expensive photosensitized fiber or pre-processed in hydrogen for days to increase its photosensitivity, which increases the time and cost. The manufacturing process also require the removal of the protective coating which is not transparent to UV light, making the fiber substrate vulnerable to disturbances. In contrast, femtosecond laser can inscribe sensors on different types of optical fiber. At the high intensity focal volume, the nonlinear absorption processes can be applied to a wide variety of commercially available optical fibers. The fabrication scheme does not require any pre-processing. As the protective coating is transparent to the NIR femtosecond laser wavelength, the mechanical strength of the fabricated sensor is preserved and can be used in the fabrication of vibration and strain sensors.

Fiber sensors inscribed on single-mode silica-core optical fiber has been widely used in environmental monitoring, meanwhile sensors fabricated specialty fibers with special doping or geometry design has also been used for specific industrial applications. The random airline-cladding (RAL) pure-silica core specialty optical fiber is a promising candidate for sensing application under radioactive environments [110]. While normal optical fibers usually have a Ge-doped optical fiber core to combine light at doped region with the higher index, the RAL fiber is made of silica only. Nanometer scale random air holes around the fiber core area form an area of lower effective refractive index, confining light inside the RAL fiber core. Similarly, continuous Rayleigh scattering centers were induced in RAL fiber.

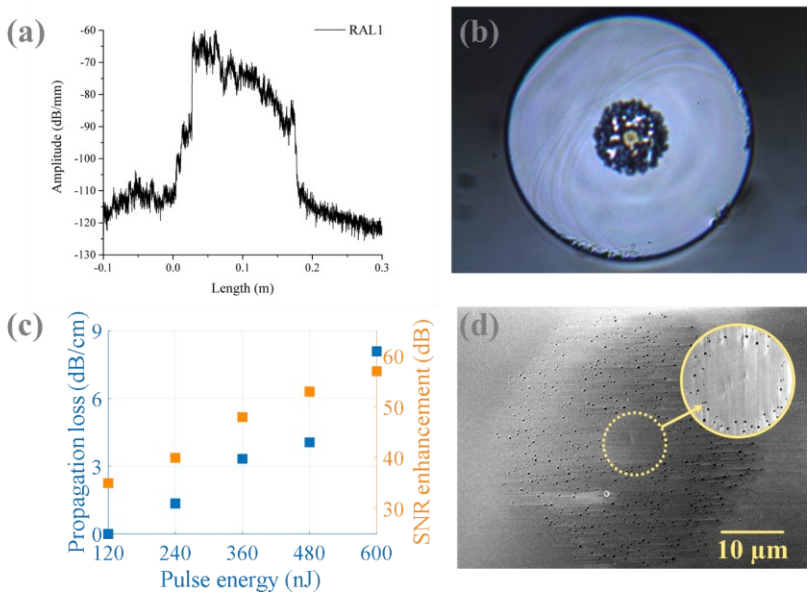

Figure 32 (a) The Rayleigh backscattering profile of a 10-cm Rayleigh enhanced section on an RAL fiber, (b) the microscopic image of a RAL fiber cross-section, (c) the dependence of the Rayleigh enhanced section loss and SNR enhancement of a RAL fiber, and (d) the SEM image showing the existence of nanograting inside the fiber core [111]**. © Copyright 2020 IEEE.**

Figure 32 (a) presents a 10-cm Rayleigh enhanced section written on a RAL fiber. The fluctuation of the laser processed region is larger due to the random distortion of the laser focus at the holes surrounding the fiber core. The corresponding microscopic image is presented in Figure 32(b). A modification spot is clearly visible inside the RAL fiber core area. Figure 32(c) summarizes the propagation loss and SNR enhancement dependency on pulse energy. The trend for the propagation loss and signal enhancement are the same as the Rayleigh enhanced section written on a single-mode fiber, as both fiber core materials are made from silica. However, the energy required is noticeable larger. The increased laser pulse energy was used to compensate for scattering of light at random air holes. The SEM photo of Figure 32(d) presents the successful inscription of high-temperature stable nanograting in the fiber core.

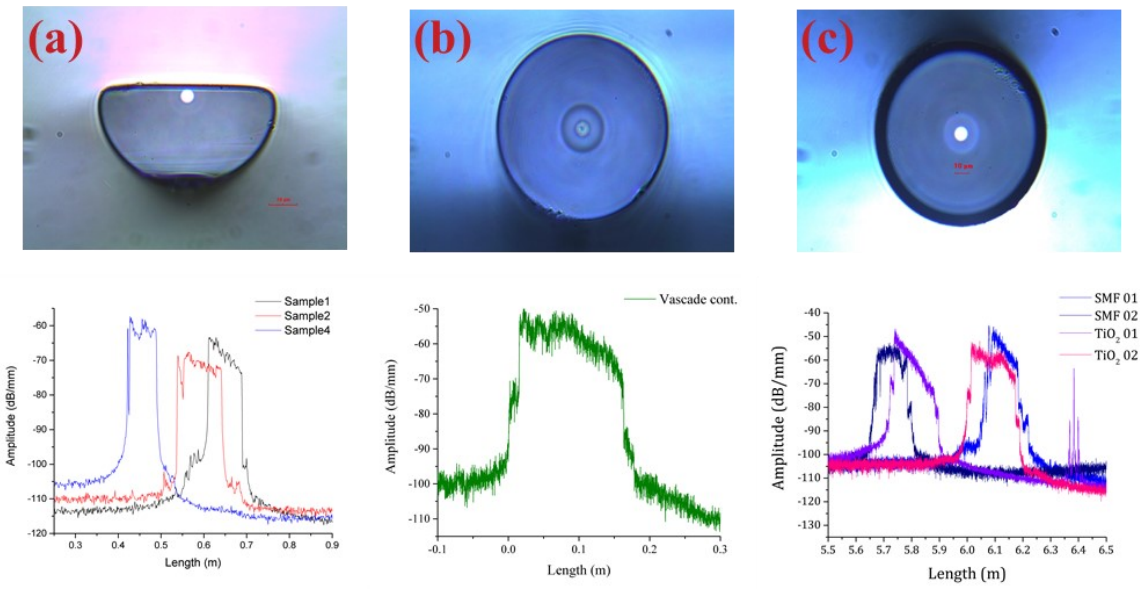

Figure 33 The optical microscopic images and the Rayleigh backscattering profile of (a) a D-shaped optical fiber, (b) a Vascade optical fiber, and (c) TiO_2-coated optical fiber.

The D-shaped fiber is fabricated from a D-shaped preform through a standard drawing process [112]. The fiber has a similar design as the silica-core single-mode fiber, the core is 9 µm in diameter, while the top of the fiber is flat. The distance from the core edge to the cladding surface is 3.5 µm. Because of the close distance from the fiber core to the cladding surface, the D-shaped surface can be act as a substrate for deposition of novel nanostructures for chemical sensing through different schemes. Writing of the Rayleigh enhanced section on the D-shaped fiber could be potentially useful for improving the resolution of distributed gas concentration sensing. Figure 33(a) presents Rayleigh enhanced profile written on a D-shaped optical fiber (Corning Inc). Fluoride-doped optical fibers are also known to exhibit good stability under radiation [113]. Rayleigh enhanced section was written in the core of a fluoride-doped cladding single-mode silica-core fiber (Corning Vascade ®). Figure 33(b) shows the Rayleigh backscattering profile and the Vascade fiber cross-section of the femtosecond laser modified section. TiO_2 is a kind of

semiconducting metal-oxides, which is able to perform chemical reaction when interaction with gas [114]. Through adding a catalyst into the metal-oxide, such as Pt, Pd, and Ag, gas concentration sensors can be formed for environmental and air-quality monitoring. The TiO_2 doped fiber has a core size similar to that of the single-mode fiber, and the cladding is 108 μm. The plastic protective coating is replaced with a thin coating of TiO_2 around the cladding area (Figure 33(c)) for sensing applications. Rayleigh enhanced section is written in the core area of the TiO_2 fiber, that can be used to improve the performance of distributed gas sensing.

4.7 Single-Crystal Sapphire Optical Fiber

Sapphire optical fiber has been known for its excellent thermal stability in harsh environment. Compared to silica fibers, sapphire has a high melting point at 2040°C and extra stability under corrosive environments [55], [115]. We applied the femtosecond laser writing technique on a 125-μm sapphire fiber for sensor integration (MicroMaterial Inc.). The optical fiber was translated along the axial direction using the customized reel-to-reel setup, and hexagonal shape sapphire optical fiber was compensated using an oil-immersion objective with index-matching oil.

A continuous track of 8-cm length was inscribed at the center of the sapphire fiber core (Figure 34(a)). Figure 34(b) shows the OBR-measured profile Rayleigh backscattering behavior. To further demonstrate the mechanisms of femtosecond laser induced modifications, the sapphire fiber was cleaved at the laser modification section. The end-facet was polished, and the cross-section morphology of the laser-induced track was observed using the SEM (Figure 34(c)). Self-organized nanostructure could be identified at the laser inscription area, whose morphology is

consistent with the formation of femtosecond laser-induced nanograting in sapphire reported in previous literatures [116], [117].

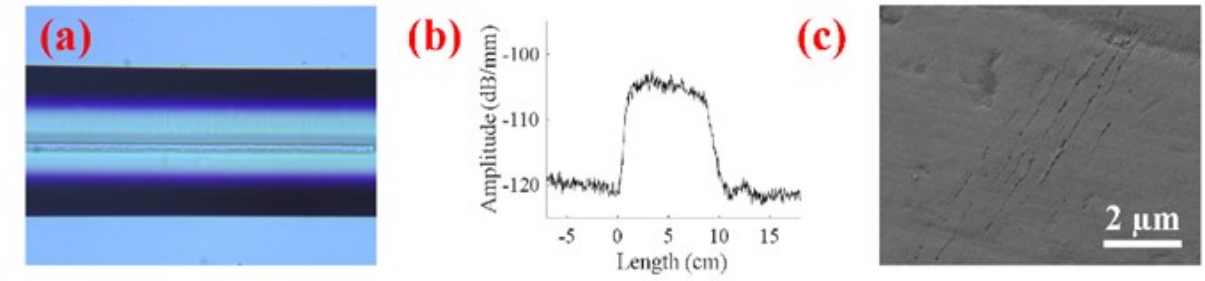

Figure 34 (a) Rayleigh enhanced section written on a sapphire optical fiber, (b) the OBR measured backscattering profile an 8-cm section of femtosecond laser modification, and (c) the SEM image of the cross-section morphology.

Commercially available sapphire optical fiber lacks optical cladding and is inherently multimode. One challenge in sapphire fiber operation is the large number of modes due to the large refractive index and the guiding of light without the existence of cladding. The multimodal behavior degrades the performance of sapphire optical fiber sensing. Previously, different techniques have been explored to make the sapphire optical fiber into a more suitable high temperature sensor, by adding a high-temperature stable cladding or chemical etching to reduce the diameter [7], [118].Waveguides were fabricated in a commercial multimode single-crystal sapphire fiber, to create an artificial core using the femtosecond laser inscribed waveguide. An 800-nm Ti:sapphire laser and amplifier system was used for fabrication, delivering 270-fs, 250-kHz linearly polarized light. Laser was tightly focused through a 100× oil-immersion objective with immersion oil. Femtosecond laser written waveguide inside a sapphire fiber, we first used a 25-mm × 25-mm c-plane sapphire bulk (MicroMaterial Inc.). The bulk was mounted on a three-

axis nano-precision stage. Femtosecond laser of different pulse energy was used to create waveguides at a depth of 60 μm under the bulk surface Modifications were inscribed at a speed of 1-mm/s. Both single-track and double-track waveguides were known to guide NIR light in a crystalline material [133].

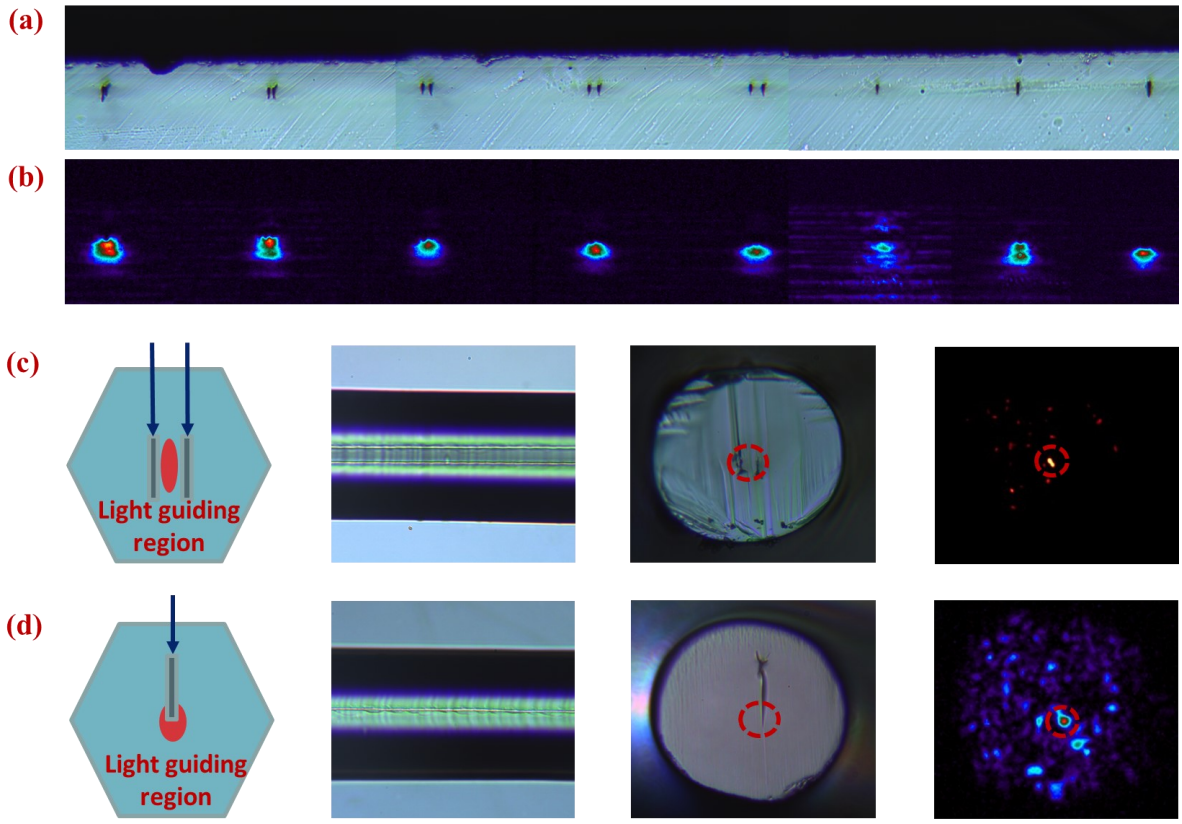

Figure 35 (a-b) The microscopic top view (a) and the mode field at 1550 nm (b) of single-track and double-track waveguides written on a sapphire bulk, and (c-d) The schematic, microscopic top view, microscopic cross-section view, and mode field at 1550 nm of a single-track (c) and double-track (d) waveguide written on a sapphire optical fiber.

Figure 35(a) shows the microscopic image of femtosecond laser written waveguides on a sapphire bulk with different fabrication conditions. From left to right, sapphire ridge waveguides

were written with 3, 6, 9, 12, 15-μm spacing at a pulse energy of 200-nJ, following single track written with 100, 200, and 300-nJ pulse energy. For characterization of the propagation behavior of the femtosecond laser-written waveguide, the sapphire bulk was mounted on motion stage. A 1550-nm laser was butt-coupled into each waveguide from a single-mode optical fiber (Corning SMF28e+). The respective mode fields of the light guiding structure written with different fabrication conditions were imaged using a 4-f imaging system and an InGaAs NIR camera (ICI Inc.), as presented in Figure 35(b). A 125-μm sapphire fiber was used for sensor integration (MicroMaterial Inc.). Both single-track and double-track waveguides were written on the sapphire optical fiber using the optimized parameter found on the bulk. Microscopic images of the polished sapphire fiber end-facet are shown in Figure 35(c) and Figure 35(d). damage track could be seen in the middle of the single-crystal fiber. The elongation of the laser modified region is probably caused by the aberration from the hexagonal shape of the crystal fiber. A 1550-nm light was coupled from a single mode optical fiber to the sapphire fiber and the measurement of the near-field profile shows a confined guiding. Femtosecond laser can be potentially used to create an artificial core inside the sapphire optical fiber, which provide an alternative technique to improve the performances of sapphire optical fiber for harsh environmental stable sensors.

5.0 Femtosecond Laser Direct Writing of Photonic Lattices

Light propagation inside a functionalized optical material shares a resemblance with the evanescently coupled optical waveguide arrays. Based on this, the femtosecond laser direct-written photonic lattices are well-established model systems to emulate complicated functionalized optical materials and to predict the quantum particle wavefunction in time. Recently, photonics lattices fabricated using femtosecond laser direct writing technique have attracted much research curiosity to discover novel phenomenon in solid-state physics. During fabrication, the laser condition can be tuned to fabricate high-density waveguide arrays which resemble photonic lattices with low propagation loss, homogeneous cross-section, and single-mode light guiding behavior. This chapter describes the physics background, the fabrication setup, and technical challenges of the femtosecond laser direct-written waveguide arrays. The chapter then presents three projects in which 3-D photonics structures were fabricated using the femtosecond laser direct writing method to study fundamental optics science. These works were performed with collaboration with Dr. Mikael Rechtsman's group (Leptos) from the Department of Physics, Penn State University to simulate the physics phenomenon of topological photonics.

5.1 Motivation and Background

Topology refers to the geometry of an optical system which can result in unique guiding characteristics. The topology of a system can be manipulated through tuning the geometric phases. One attractive application of manipulation of topological phases is a topological insulator, which

is an insulator in the bulk but metallic on the edge. The edge states inside a topological insulator are in the bandgap. Light propagating inside these edge states are topologically protected and are immune from back scattering. They provide a promising novel method of electron transport in the presence of disorder, and thus can be used towards topologically insulated laser and slow light devices [119]–[121].

While new topological designs are proposed, it is hard to verify the electron transport behavior through conventional electronics method. Alternatively, due to the analogy between a quantum system and a classical photonics system, the experimental realization of the theorical topological designs can be realized using semiconductor technology. However, the design requires multiple steps and expensive equipment. On the other hand, light propagation inside an evanescently coupled single-mode waveguide array is akin to the quantum evolution of particle wave functions. Recent years, many newly proposed topological phenomena have been verified using a photonics system. The modes inside a waveguide array are analogues of topological zero mode.

In quantum mechanics, the diffraction of light can be described by the paraxial Schrodinger equation under tight-binding approximation. The wavefunction ψ can be described by the following:

$$i\hbar\frac{\partial}{\partial t}\psi(x,y,z) = -\left(\frac{\hbar^2}{2m}\left[\frac{\partial^2}{\partial x^2}+\frac{\partial^2}{\partial y^2}\right]-V(x,y,z)\right)\psi(x,y,z) \qquad (5-1)$$

Meanwhile, in a classical system, the light propagation inside a photonics lattice with weakly coupled optical waveguides can be described using the Helmholtz equation with paraxial approximation. The electrical field envelope E can be described as:

$$i\bar{\lambda}\frac{\partial}{\partial z}E(x,y,t) = -\left(\frac{\bar{\lambda}^2}{2n_0}\left[\frac{\partial^2}{\partial x^2}+\frac{\partial^2}{\partial y^2}\right]+\Delta n(x,y,z)\right)E(x,y,t) \qquad (5-2)$$

The following resemblances can be concluded from the Schrodinger and the Helmholtz equations:

- The time t (Schrodinger) and the propagation distance z (Helmholtz)
- The Planck's constant $\hbar = \frac{h}{2\pi}$ (Schrodinger) and the reduced wavelength $\bar{\lambda} = \frac{\lambda}{2\pi}$ (Helmholtz)
- The mass m (Schrodinger) and the refractive index n_0 (Helmholtz)
- The Potential V (Schrodinger) and the refractive index change $\Delta n = n_0 - n(x,y,z)$ (Helmholtz)

From the above connections, the evolution of quantum wavefunction in time t can be indicated from the evolution of wave packet in propagation distance z, while the effective potential can be emulated using the refractive index profile change across the lattice. Femtosecond laser can locally induce a permanent and positive refractive index change inside a highly localized focal volume in a material. Light would be confined in waveguides when propagating inside a waveguide array. Through observing the propagation of light, this resemblance enables a more observable method to simulate the complicated quantum phenomena. The research in solid-state physics, which requires resolving the electron probability wavefunction in very short time, can be solved using optics tools. The technique has been exploited to verify a wide range of topics in physics, including quantum-optical analogues, optical effects, nonlinear phenomena such as Bloch oscillations and dynamic localization [122], [123].

5.2 Bulk Photonics Array Fabrication and Calibration

5.2.1 Fabrication Setup

The well-established material platform Corning Eagle XG borosilicate glass was used for the photonics lattices covered in this chapter. Before fabrication, the side surfaces of the glass were polished to optical quality, and front and back surfaces were thoroughly cleaned. The glass was mounted on a three-axis nano-precision motion stage using a vacuum pump. Linearly polarized laser light was delivered from the laser system to the glass sample through the beam delivery system described in Chapter 2, then through a 50× aberration-corrected objective (NA = 0.55). The motion stage was then translated according to a pre-programmed trajectory and speed written in G-code while the laser focus was fixed. The inscription was performed layer-by-layer from the bottom layer to the top surface.

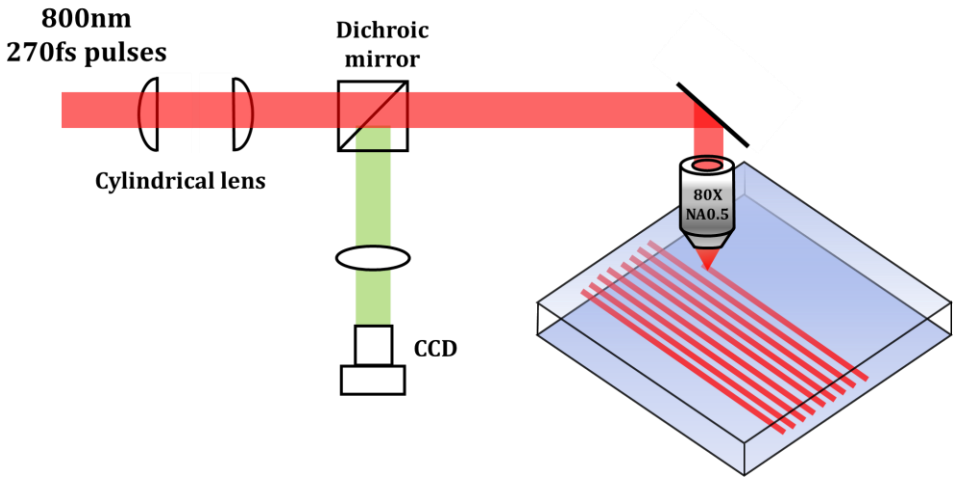

Figure 36 The schematic femtosecond laser direct writing waveguide setup on glass.

Waveguide arrays discussed here were fabricated using the transversal writing geometry. As discussed in detail in Chapter 2, the transversal writing scheme can construct 3-D photonics circuits which are relatively large in scale. The size is limited only by the maximum translation range of the motion stage system, which is usually 10s of centimeters. However, unlike the longitudinal writing geometry, in which the waveguide size is determined by the beam focal volume. In transversal writing geometry, only the waveguide waist perpendicular to the propagation direction is determined by the beam focal size w_0, while the waveguide waist parallel to the propagation direction is determined by the depth of focus, or the Rayleigh range of the laser $z_R = 2\pi w_0^2/M^2\lambda$ or the confocal parameter. For an 800 nm laser pulse focused to a circular spot of a 1 μm radius, the confocal parameter is calculated to be ~ 30 μm. This leads to a highly elongated waveguide size with an aspect ratio of larger than 10 to 1. In order to achieve a symmetrical circular beam profile, the following equation needs to be satisfied:

$$w_0 = z_R = \frac{\pi w_0^2}{M^2\lambda} \qquad (5-3)$$

However, the solution of the above equation for a symmetrical beam profile $w_0 = M^2\lambda/\pi$ requires a tight, nearly diffraction-limited focusing with sub-micrometer in scale, which is hard to achieve in real. To address these challenges and produce a waveguide with more symmetrical profile, many methods have been developed, including astigmatic focusing [124], slit aperture [125], [126], and multi-scan [127], [128]. In this chapter, the astigmatic beam shaping method was applied. The technique introduces a pair of cylindrical lenses, that has different focus. The Gaussian beam thus has an astigmatic profile. The intensity, beam size, and Rayleigh range can be described by the following equations:

$$I_0(x,y,z) = I_{00}\left(\frac{w_{0x}}{w_x(z)}\right)\left(\frac{w_{0y}}{w_y(z)}\right)e^{-2\left(\frac{x^2}{w_x(z)^2}+\frac{y^2}{w_y(z)^2}\right)} \quad (5-4)$$

$$w_x(z) = w_{0x}\sqrt{1+\left(\frac{z}{z_{Rx}}\right)^2} \quad z_{Rx} = \frac{\pi w_{0x}^2}{\lambda} \quad (5-5)$$

$$w_y(z) = w_{0y}\sqrt{1+\left(\frac{z-z_0}{z_{Ry}}\right)^2} \quad z_{Ry} = \frac{\pi w_{0y}^2}{\lambda} \quad (5-6)$$

z_{Rx} and z_{Ry} are the Rayleigh ranges for x and y directions. z_0 is the astigmatic difference between the beam waists, which is a key parameter to control the waveguide profile. With the help of the telescope lens, the beam waists in the x and y direction are now controllable. In the transversal writing geometry, the sample is translated along the x direction. As a consequence, the waveguide size is determined by the y direction Rayleigh range and the beam waist size w_y, while being independent of the beam waist size in the x direction w_x. By decreasing the x-direction Rayleigh range through changing the astigmatic difference z_0, the higher divergence in the x-z plane would reach the nonlinear absorption threshold faster, resulting in a smaller depth of focus.

In sum, the waveguide cross-section will be determined by the waist size along the less focused direction (y direction in this case) and the depth of focus along the tight focused propagation direction (x direction in this case). By choosing the proper aspect ratio of the aperture, the shape of the waveguide can be tuned. In this experiment, a pair of cylindrical lens (f_1 = 50 mm, f_2 = 150 mm) was installed inside the beam path, demonstrated in Figure 36. The distance z_0 between the two lenses was carefully tuned with respect to different focusing objective and materials. With the feedback from the following characterization method, the distance was tuned to achieve the waveguide profile with an optimal guiding performance.

5.2.2 Waveguide Characterization

After the writing process, the waveguides are first observed by an optical microscope for the mode field size and shape. For the light guiding performances, waveguides are characterized at the NIR wavelength range using the setup shown in Figure 37(a). Light from a Tunable Laser Source (Santec TLS210) was transmitted through a single-mode fiber (Corning SMF28e+) which is butt-coupled to the bulk glass chip with the help of a 3-D nano-precision stage. A polarization control unit was used to tune the polarization of the input light. The near field output pattern from the waveguide array is collected with a 2-f imaging system and captured by an InGaAs CCD camera (ICI SWIR). The waveguide profile was modeled using a hyper-Gaussian distribution:

$$\Delta n(x,y,z) = \Delta n_0(z) e^{\left(-\left(\frac{x}{\sigma_x}\right)^2+\left(\frac{y}{\sigma_y}\right)^2\right)^3} \qquad (5-7)$$

Meanwhile, a flip mirror is used to guide the collected output light to an integrating sphere for power measurement. The loss of the waveguide was characterized, in order to determine the most optimized waveguide. For a waveguide written on bulk, the total loss can be expressed with the following equation:

$$P_{Total} = P_{IL} + L\,\alpha \qquad (5-8)$$

The first part of the equation P_{IL} is the waveguide coupling loss, which is a result of the mismatch between the waveguide mode and the single-mode fiber mode, while α is the propagation loss coefficient, which is the result of waveguide fabrication defects induced scattering loss. Traditionally, both losses can be measured and calculated using a transmission and a cut-back method. The bulk waveguide is cut back millimeters in length, and the power is measured to determine the propagation loss, while the insertion loss is determined by the offset of the power

measurement curve [129]. However, this method is destructive to the optical chip. Alternatively, the insertion loss can be calculated by the overlap integral between the measured waveguide mode profile and the fiber mode, while the propagation loss can be measured using interrogation units, such as an OBR [130]–[132].

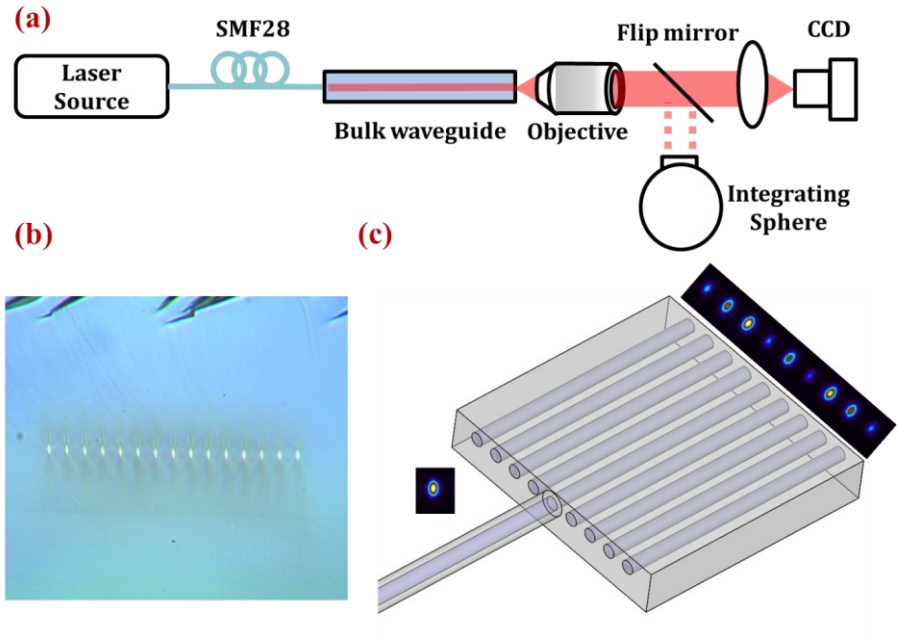

Figure 37 (a) Schematic of the waveguide array characterization set-up, (b) microscopic photo of a 1-D waveguide aray, and (c) schemaic of the 1-D refractive index calibration setup.

Common approaches to measure the refractive index include using equipment such as a refractive index profilometer [133] or a quantitative phase microscopy method using a phase contract optical microscope with the inverse Abel transform [134]. Alternatively, refractive index can be calculated from the analysis of shifted near-field intensity profiles [135]. For the waveguide circuits fabricated in this chapter, a method based on observing the diffraction pattern of a designed 1-D waveguide array (Figure 37(b)) was used to determine the waveguide refractive index against

the simulated results. The waveguide number, waveguide-to-waveguide separation and coupling length of the array were carefully chosen to allow the near-complete transfer of energy from the middle waveguide, where light is injected to the waveguide closest to the edge. Figure 37(c) shows the measurement setup diagram for such a calibration structure.

Both the microscopic cross-section and the output pattern of a refractive index calibration waveguide array composed of 15 parallel straight waveguides is presented in Figure 38. The different diffraction patterns were measured at a wavelength of 1550 nm and correspond to different writing speeds for calibration. The waveguide array has a 30-μm spacing and 55-mm propagation distance. Laser was injected into the center waveguide, then continued to spread out by evanescent coupling while propagating. The spacing and coupling length allow the light at the tested refractive index range to spread out while energy remained spreading in a single direction at the end of the propagation distance. It can be seen from the Figure 38 that with the decrease of the translation speed, the beam spread out due to the decrease in refractive index while the waveguide beam waists stay almost unchanged.

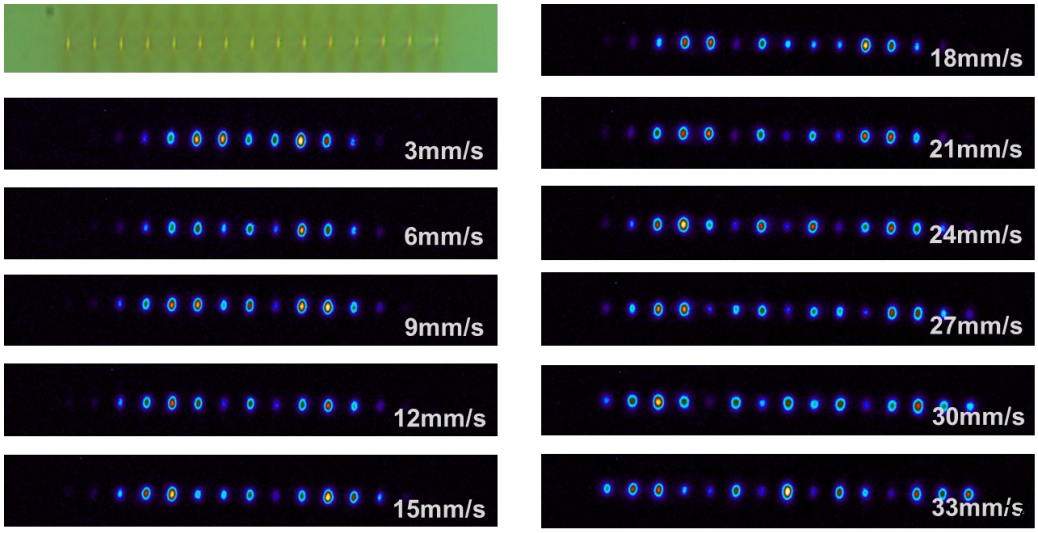

Figure 38 The microscopic image of the linear array (top right) and the measured output pattern (rest).

The above diffractive pattern was compared with the simulation data. Simulation in this chapter was performed using the Beam Propagation Method (BPM) in both BeamPROP (RSoft) and a MATLAB code composed by Dr. Mikael Retchsman and his group. The waveguide profile was measured from experimental data through fitting the near field mode profile with a Gaussian mode. These data were taken back to the simulation parameters. A set of simulation was performed using different refractive indices, then the experimentally measured pattern was compared with the simulation pattern to decide the refractive index change of the femtosecond laser-written waveguides. A refractive index modification at the range of 2×10^{-3} to 3.3×10^{-3} can be obtained at a pulse energy of 800 nJ to inscribe a single-mode low-loss waveguide on Eagle XG glass.

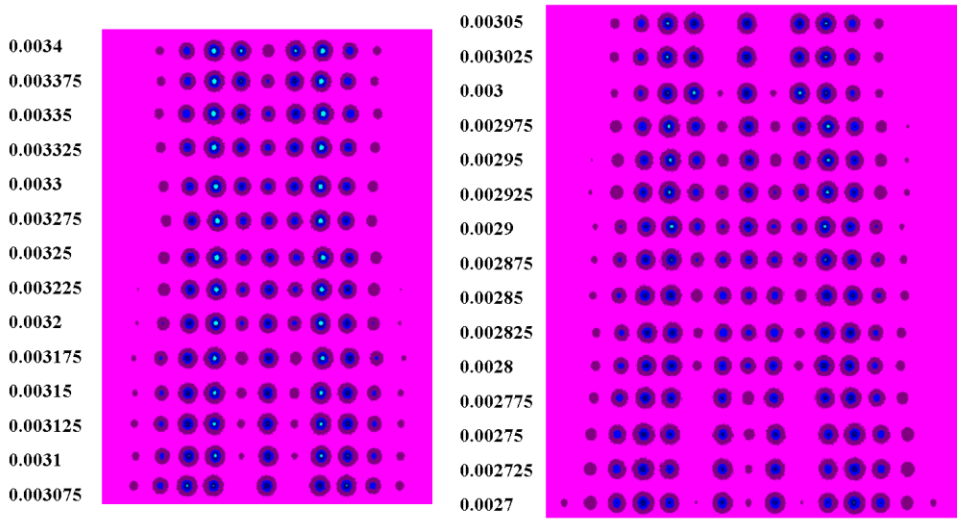

Figure 39 Examples BeamPROP (Rsoft) simulation results of the 1-D waveguide of different refractive indices (left column).

The refractive index can be extracted from the experimental measurement in Figure 38 using a computer-generated machine-learning based regression model. Simulation of the light propagation in the designed waveguide array was performed on a range of refractive index

differences between 1.5×10^{-3} and 7×10^{-3} (Figure 39(a)). This range was chosen to guarantee proper guiding confinement and single mode guiding behavior. To obtain a closer similarity between the simulation data and the real measurement, different types of noise including Gaussian and flicker noise, image rotation at angles $\pm 5^{o}$, and refractive index difference randomness was added during the simulation. For each dataset, the peak power intensity was extracted from each waveguide inside the array. After the argumentation, a regression model was trained on a total of 55,000 datasets in the MATLAB Regression Learner App. A variety of regression algorithms were tested and a five-fold cross-validation method was used. The results are presented in Figure 40, showing the performance of each model. The best model is found to be the ensembles of bagged trees. The Root Mean Square Error (RMSE) was found to be 7.17×10^{-6}.

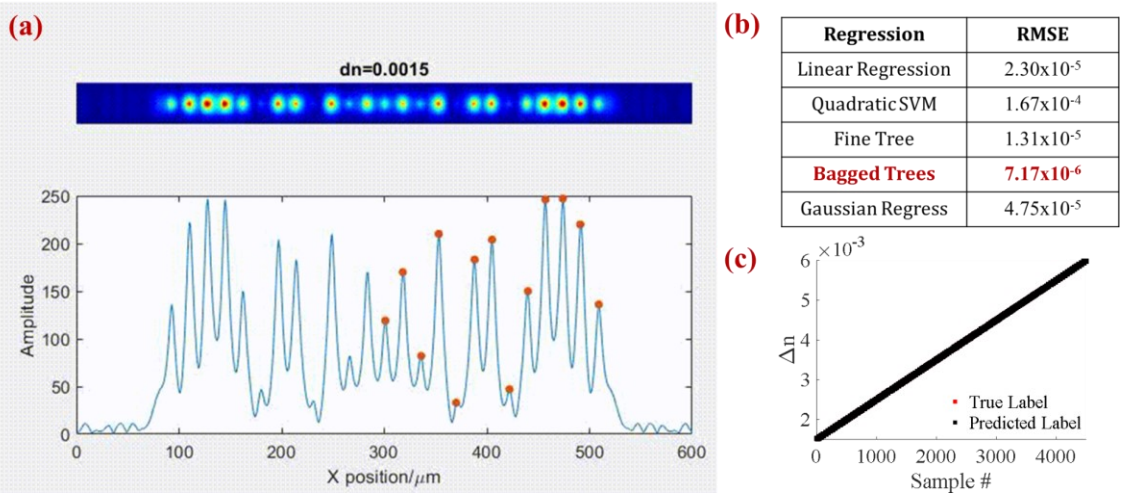

Regression	RMSE
Linear Regression	2.30×10^{-5}
Quadratic SVM	1.67×10^{-4}
Fine Tree	1.31×10^{-5}
Bagged Trees	$\mathbf{7.17 \times 10^{-6}}$
Gaussian Regress	4.75×10^{-5}

Figure 40 (a) The waveguide array simulation output, (b) performances of different regression models, and (e) the response plot of the bagged trees model.

5.2.3 Optimization Procedure

As discussed in the above section, during the fabrication, the beam shaping method was applied to mitigate the asymmetrical waveguide cross-sectional area. The astigmatic difference was fine tuned to guarantee a near-symmetrical beam shape. The laser pulse energy was then scanned to write a series of waveguides to measure the lower and higher energy limit of a single mode guiding behavior of a waveguide. Afterwards, 1-D waveguide arrays were written with different laser powers in this range to calibrate their respective mode profiles and their corresponding refractive indices using the above-mentioned method. For applications that require dynamically refractive index adjustment, different speeds were used to write these 1-D arrays at a fixed chosen pulse energy [136].

Nevertheless, one intrinsic challenge of femtosecond fabrication is the wavefront distortion at the interface between air and the material platform. By using the femtosecond laser direct writing method, 3-D photonics lattices can be constructed layer-by-layer. However, the mismatch in the refractive index between air (n = 1) and the borosilicate glass (n = 1.47) lead to a depth-dependent aberration inside the photonic lattices. Figure 41(a) left shows a vertical 1-D array written with no aberration compensation. The bottom waveguides suffer from higher aberration and are elongated with a slightly lower refractive index. The spherical aberration limits the accuracy and scale of the fabricated photonics circuit, while solutions have been proposed to mitigate the distortion of focus, such as a spatial light modulator, deformable mirror, MEMS digital mirror array [137], [138]. However, these all involves complicated setup and expensive equipment. Moreover, adding extra equipment in the beam delivery system will incur extra optical power loss.

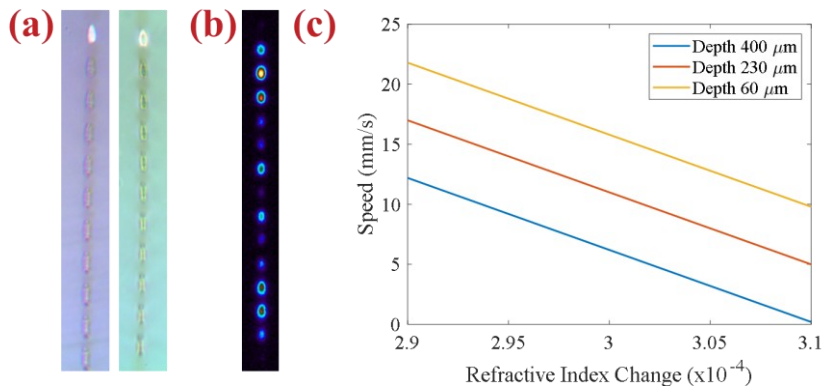

Figure 41 Vertical waveguide arrays written with differnet speed compensation methods, (a) with no compensation (left) and with depth-dependent speed compensation (right), (b) diffraction pattern of a speed-compensated aray, and (c) the depth-dependent speed compensation curve.

To address these challenges to fabricate a waveguide array with simple setup, negligible variations in depth, and symmetry in cross-sectional shape, fabrication conditions were tuned to compensate for the aberration during fabrication. Horizontal waveguide arrays were first written at different depths up to a maximum depth of 450 μm using the method described in section 5.2.1. Their coupling constants at a function of depth and speed were calculated. The depth-dependent aberration was compensated using dynamically adjusting the speed at each depth. Figure 41 shows an example of the fitting curve.

5.3 Braiding Photonics Topological Zero Modes

The braiding of topological defects describes when the two defects are would around one another. This can result in non-trivial geometric phase which comes from the adiabatic change of the bound-state wave function. A single braid can lead to any phase between 0 and π. The non-

Abelian braiding is a universal wave phenomenon beyond the electronics system, which has been predicted theoretically. In this project, evanescently coupled waveguides were used to characterize the braiding of the vortices. Braiding of topological defects are emulated in a waveguide array as vortices in a vector field. An offset α was applied to the lattice's order parameter to monotonically increase or decrease the geometrical phase. Two arrays with either 0 or π geometrical phases are designed by tuning the photonics vortex modes through parameter α. Their relative phase can be observed directly using the photonics lattices through the interference between two vortices with difference modes. This work can provide a robust quantum information processing solution, and can be also useful in the study of condensed matter physics, cold atomic gases, and quantum communication applications [139].

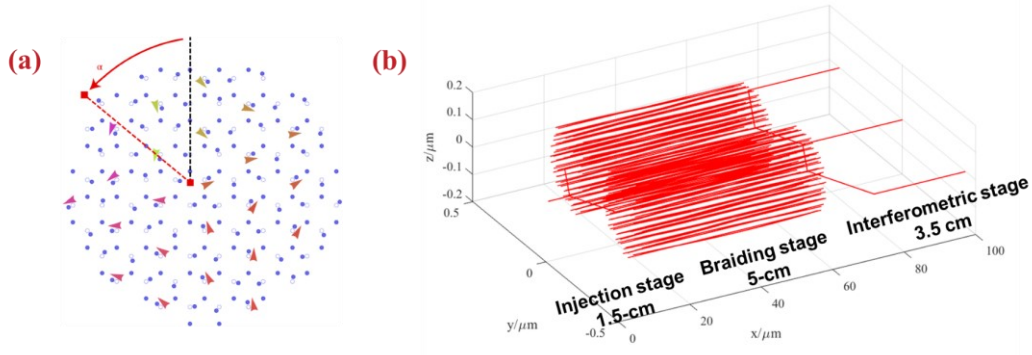

Figure 42 (a) Femtosecond laser direct writing setup schematic and (b) optical microscopic photo of the cross-section of a 1-D waveguide array output.

The first experiment verifies the constructive interference between two identically braided lattices. The order parameter of both lattices on the left and right are rotated from α to $\alpha + \pi$, that the vortex was braided at infinity around both lattices counterclockwise by an angle π. Light from both the left and right lattices have the same phase. Then in the second experiment verifies the

destructive interference between two lattices with a 2π phase difference. The left lattice is rotated from α to $\alpha + \pi$, while the right lattice from α to $\alpha - \pi$. In this case, the vortex at infinity was braided 180^o counterclockwise around the left lattice, while clockwise around the right vortex.

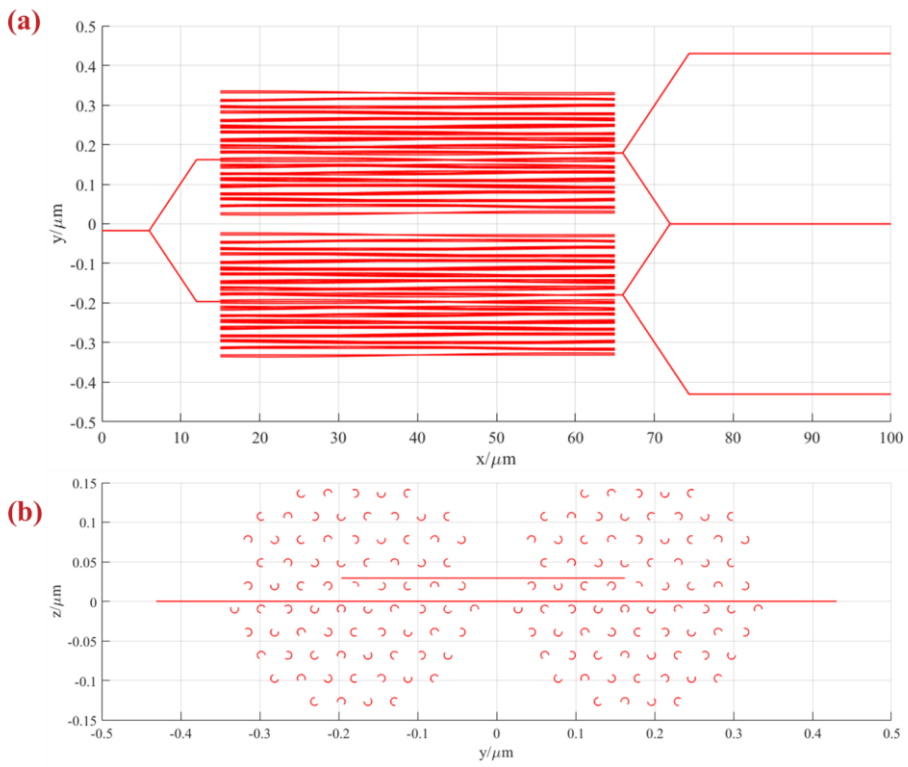

Figure 43 (a) Birdview of the photonics lattice and (b) front view of the lattice.

The photonics arrays were inscribed on a 10-cm Eagle XG borosilicate chip. The entire photonics structure consists of three parts, an injection stage (1.5 cm), a braiding stage (5 cm), and an interference stage (3.5 cm). The first stage is a symmetrical Y-branch structure that splits the input light evenly into the center waveguides of the lattice in the left and the one in the right, that the input of both lattices have equal amplitude and phase. The second stage contains the braiding structure. As light from the center waveguide of each lattices enters each braiding waveguide array, light diffracts throughout the distorted honeycomb lattice. Each waveguide moves smoothly along

the propagation direction to produce the rotation of a displacement angle, resulting in a change in the order number.

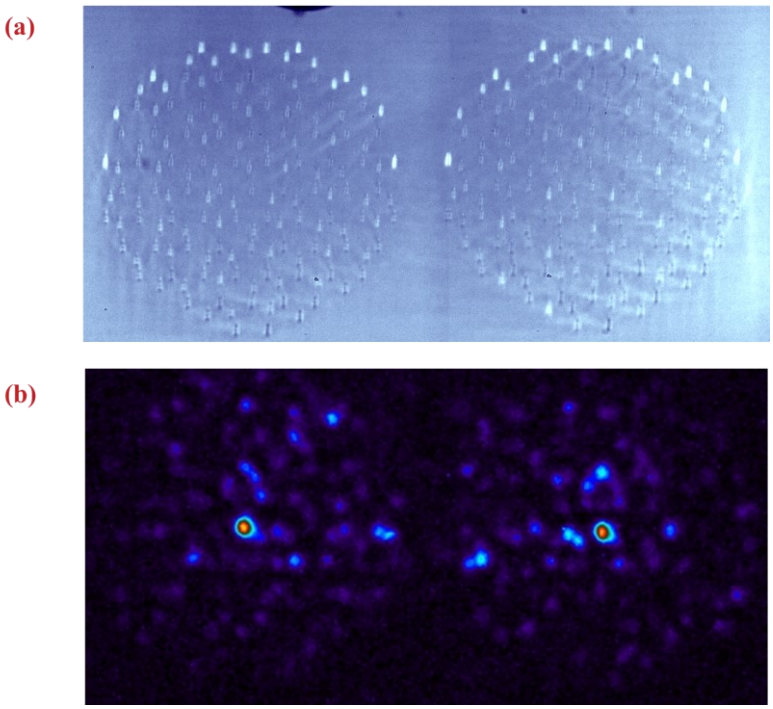

Figure 44 (a) The microscopic photo of the two photonics lattices cross-section at the output of braiding section and (b) the measured output at 1550 nm.

This is followed by a third interferometric stage which contains two Y-branch structures. The vortex-mode light from center waveguides of the left and right lattices propagate through two waveguides, while the rest of the waveguides in the lattice are terminated. The light from both lattices are split symmetrically into two with equal amplitude and phase. Then the two innermost waveguides are combined in the middle to interfere with each other. If the two vortex-mode lights are in phase with each other, and thus, the excite the symmetric bound mode and lead to a higher intensity at the combined waveguide. Otherwise, when the two lights are out of phase, light will

be diffracted away. In this way, the relative phase of these waveguides at the braiding structure can be measured.

The results at the wavelength of 1550 nm are shown in Figure 44. The waveguide arrays were verified part-by-part. The Y-branch structures in the injection stage and the interferometric stage were first tested to make sure light splits and combines with the correct intensity. Afterwards, the output of light after the injection and braiding stage was verified. A large portion of the input light remain localized near the vortex core, while the rest of the light diffracts throughout the lattice during propagation. This matches the simulation result, indicating the braiding process was performed sufficiently adiabatically. Figure 45 (a) and (b) shows the result after the interferometric stage. When the left and right waveguides are braided in the same direction, constructive interference takes place. Meanwhile, when the left and right waveguides are braided in opposite directions, destructive interference lead to a nearly zero intensity in the middle.

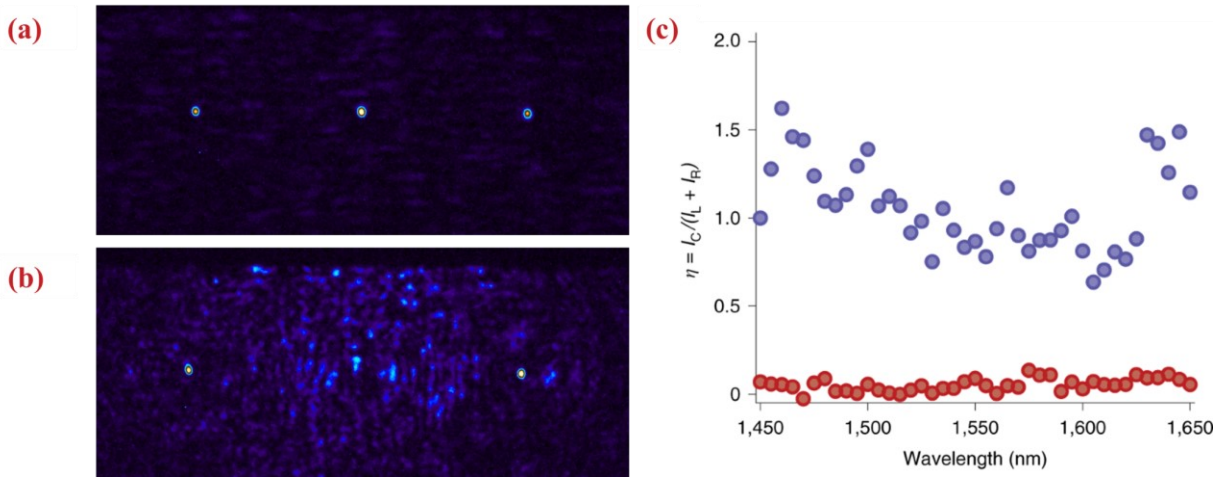

Figure 45 The measured output diffraction pattern after the interferometeric section when the two lattices are braided in the (a) same direction and (b) different direction, and (c) the contract of the interferometer observed at difference wavelength (Figure (a), (b), and (c) source: [139]**; use permitted under the Creative Commons Attribution License CC BY).**

The interference was calculated using the contrast $\eta = \frac{I_{Combined}}{I_{Left}+I_{Right}}$while I_{Left}, I_{Right}, and $I_{Combined}$ are the measured intensity of the left, right, and combined waveguides. A contrast of close to 1 was calculated for the constructive interference, while the destructive interference is a close to zero. These are consistent with the numerical simulation. The photonics arrays were measured at 1450 to 1650 nm. The different wavelengths correspond to different dynamic phases during propagation. While the measurements are insensitive to wavelength, the phase difference comes from the geometric phase, instead of the dynamic phase. Figure 45(c) presents the experimentally measured contrast data when both lattices are braided in the same direction and in opposite direction.

5.4 Thouless Pumping in Disordered Systems

Adiabatic charge pump is a kind of topological system. When a system with a uniformly filled valence band is periodically modulated, the localized Wannier states has adiabatically evolved to be transported by a unit cell. Then if the system is finite, the Wanner states are pumped across the bandgap to the conduction band. The system can be viewed as Chern insulators in the 1+1 dimensions, as the periodic modulation in time can be viewed as a second spatial dimension. Such a system was original proposed by Thouless to provide a method for to perform topological pumping. The electronic adiabatic pumps have studied the bulk transport on adiabatically pumped optical platforms. In the experiment, nearly quantized topological transport was realized in a Thouless pumped optical system. Meanwhile, the Thouless pumping in the presence of a disorder

was also verified. The experimental studies here can be useful for applications such as a high-density optical interconnect and slow light devices [140].

The Rice-Mele tight-binding model is an adiabatic pump model. It is a bipartite array generated from periodically modulated on-site energy and coupling coefficients of the Su-Shrieffer-Heeger lattice. The Rice-Mele model Hamiltonian can be written as:

$$\widehat{H}_{RM}(z) = \left\{ \sum_{j} \left[\frac{\tau}{2} + j \left(\frac{\delta_j(z)}{2} \right) \left(\hat{c}_j^{\dagger} \hat{c}_{j+1} + h.c. \right) + \Delta_j(z) \hat{c}_j^{\dagger} \hat{c}_j \right] \right\} \qquad (5-9)$$

τ is the uniform hopping amplitude, $\hat{c}_j^{\dagger}$ and $\hat{c}_j$ are the creation and annihilation operators on the lattice site j, $\delta(t)$ and $\Delta(t)$ are the dimerization order and staggered sublattice on-site energies. In the experiments, the degree of on-site energy and the coupling variation are chosen to be:

$$\delta_j(z) = \tau \left(e^{(-1)^j \tilde{\delta} \sin\left(\frac{2\pi z}{Z}\right)} - 1 \right) \qquad (5-10)$$

$$\Delta_j(z) = \left[(-1)^j \bar{\Delta} \cos\left(\frac{2\pi z}{Z} \right) \right] \qquad (5-11)$$

$\bar{\Delta}$ is the on-site energy modulation and $\tilde{\delta}$ is the evanescent coupling modulation between neighboring waveguides. In this project, the Rice-Mele model of the Thouless pump was represented from evanescently coupled waveguide array, while the on-site energy being represented by the refractive index and the effective coupling coefficient as the waveguide separation [140].

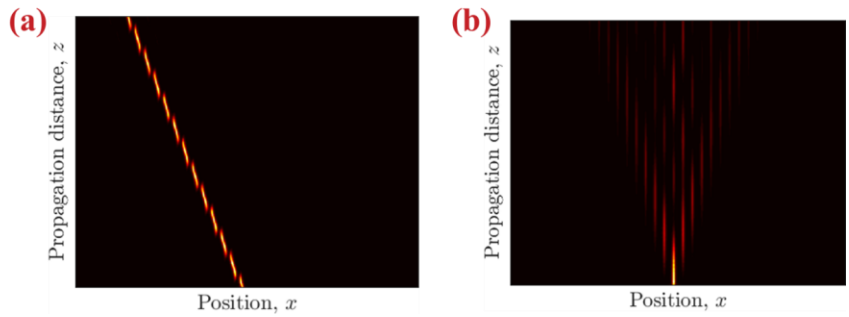

Figure 46 (a-b) The simluation of the light propagation inside a straight waveguide array and (c-d) the light propagation in the non-trivial mode.

The Thouless pumping system was emulated using waveguide arrays. Using femtosecond laser direct writing, 1-D arrays which consisted of 60 waveguides were inscribed into a 12-cm long Eagle XG borosilicate glass bulk using a pulse energy of 820 nJ. The schematic is shown in Figure 46(a). The size and shape are controlled within the laser's focal volume using a beam shaping cylindrical telescope setup, using a 50× aberration-corrected objective. Each waveguide is periodically modulated both in the spacing between neighboring waveguides and refractive index. The modulation period is set to 12 cm to emulate adiabatic pumping. The average spacing between each waveguide is 36 μm, with an added sinusoidal variation in the spacing of ±8 μm. The waveguide average index is set to be Δn=2.7 × 10^{-3}, which was also modulated from Δn=2.4 × 10^{-3} to 3.0 × 10^{-3} through each period. As a result, the on-site energy change and the coupling constant was tuned by refractive index modulation and evanescence coupling spacing. The refractive index calibration was performed using the method described in Chapter 5.2, then achieved using the dynamic speed variation during fabrication. Figure 46(b) shows the modulation of position and refractive index along the 12 cm long period.

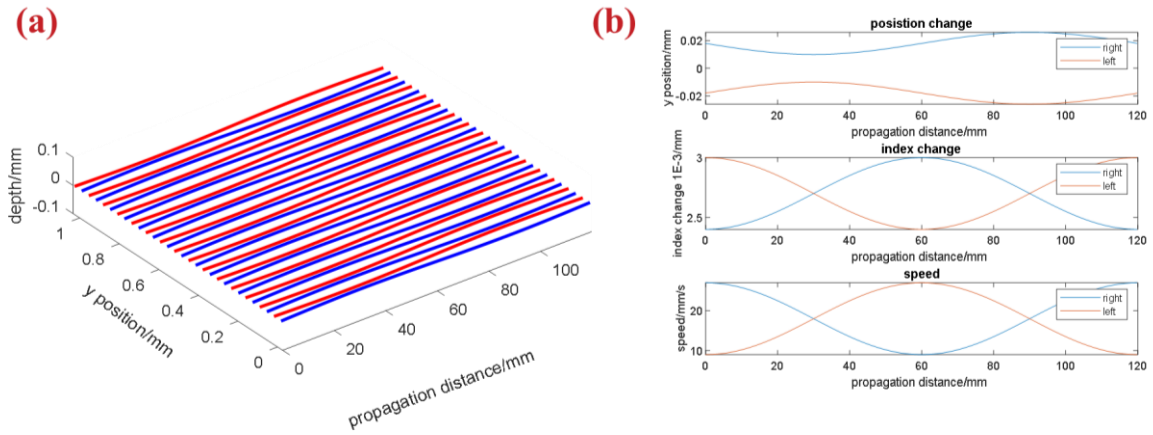

Figure 47 (a) Birdview of the cyclic modulated waveguide array and (b) the designed modulation of the waveguide position and refractive index variation.

System disorders were added to the system to observe their influences to the Thouless transport properties. Disorder is added by changing the spacing randomly over one pumping cycle between neighboring waveguides. A noise in spacing from 0 to 7 μm was added. Figure 48 (a-b) shows the microscopic cross-section view of evenly spaced waveguide array with no noise added and the array with spacing noise added. For characterization, the waveguide arrays were measured at a wavelength between 1450 and 1650 nm. The profile was measured to be 3.2 μm and 4.9 μm at the half maximum of the major and minor axis. During each measurement, one single waveguide was excited as light diffracted inside the array and the output pattern was recorded (Figure 48(c)). Figure At the wavelength of 1450 nm, the operation is in the non-adiabatic regime, while at 1650 nm, the system is in the adiabatic regime. The results were compared with to the simulation of the bulk bandgap width. Figure 48(d-g) shows the simulation and experimental results. When the noise is small, robust transport behavior is demonstrated, indicating tolerant to adiabaticity deviation and the system disorder. However, then the noise increases, the disorder strength increases. The

bulk mobility gap of the instantaneous spectrum is reduced and close to the modulation frequency and the transport is interrupted.

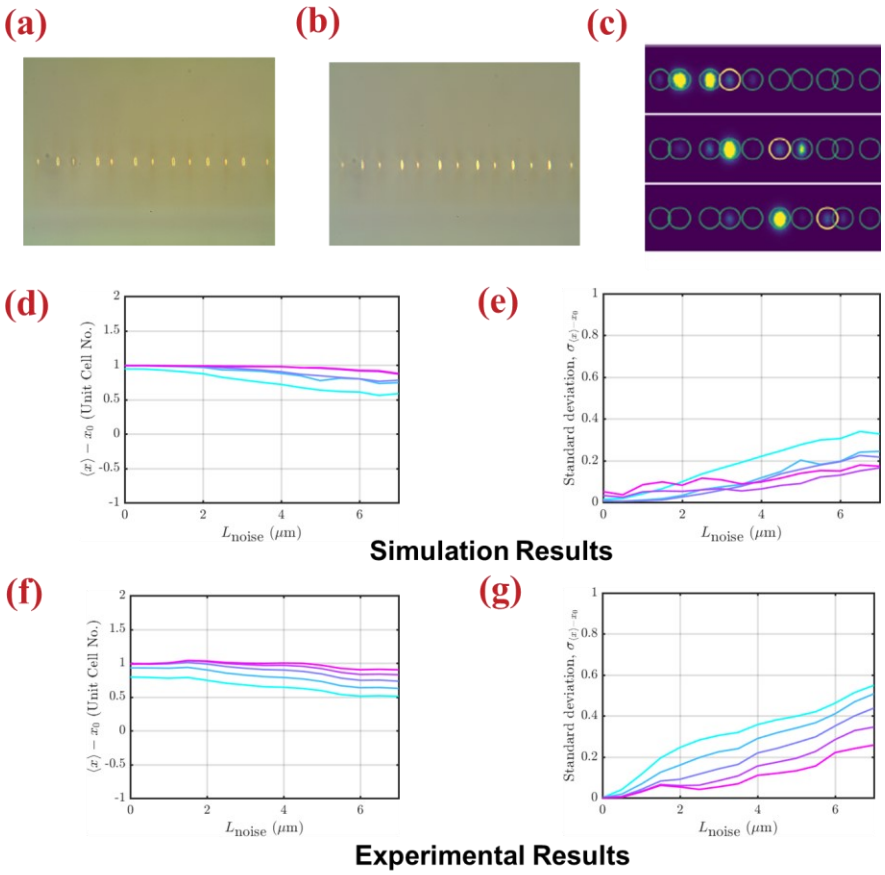

Figure 48 (a-b) The microscopic photo of the end-facet of a portion of the 1-D waveguide arrays (a) and with noise added (b), and (c) the experimental observation of transport at 1650 nm wavelength with disorder, (d-e) the simulation result of the dependence of the ensemble averaged variation (d) and the minimum mobility gap (e) on the disorder level, and (f-g) the experimental results (Figure(b) and (c) source: [141]**; use permitted under the Creative Commons Attribution License CC BY).**

5.5 Higher-Order Topological Pumping

Topological insulators have quantized transport properties and unconventional boundary states. The quantized particle transport in adiabatic pumping cycles in a periodic structure was discovered by Thouless. The Thouless system is topologically periodic in one-dimension. This section studies the counterpart of the Thouless topology in higher dimension. Higher-order topological insulator has protected in-gap states or fractional charges at the boundary of a boundary. They have been identified in arsenic and antimony monolayers and phases with corner states. Nontrivial adiabatic pumping cycles in 2-D crystal can be topologically nontrivial. They can product electron transport from corner to corner. In this research study, a model for a higher-order topological pump was realized using a 2-D lattice structure that evolves periodically. The energy was transferred from one corner of the structure to the other corner [142], [143].

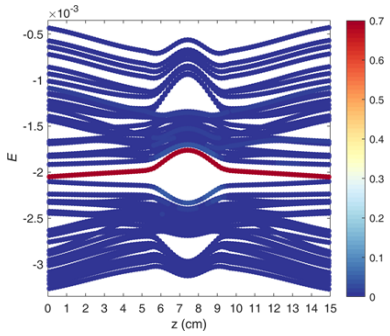

Figure 49 The simulated spectrum during one pumping cycle (Image source: [144]**; use permitted under the Creative Commons Attribution License CC BY 4.0.).**

The waveguides were written on an Eagle XG glass chip. The structure consisted with a 12-cm glass chip for the straw chip and a 15-cm chip of the pumping chip. The waveguides were written using a laser pulse energy of 810 nJ. The pumping chip consist of 54 waveguides, each

modulated in position and refractive index to simulate the desired pumping cycle. A 3-D schematic is shown in Figure 51(a). Depending on their types, each waveguide was modulated with the refractive index variation demonstrated in Figure 51(b). The waveguide array has honeycomb structure (Figure 51(c)) that varies in the propagation direction (Figure 51(d)).

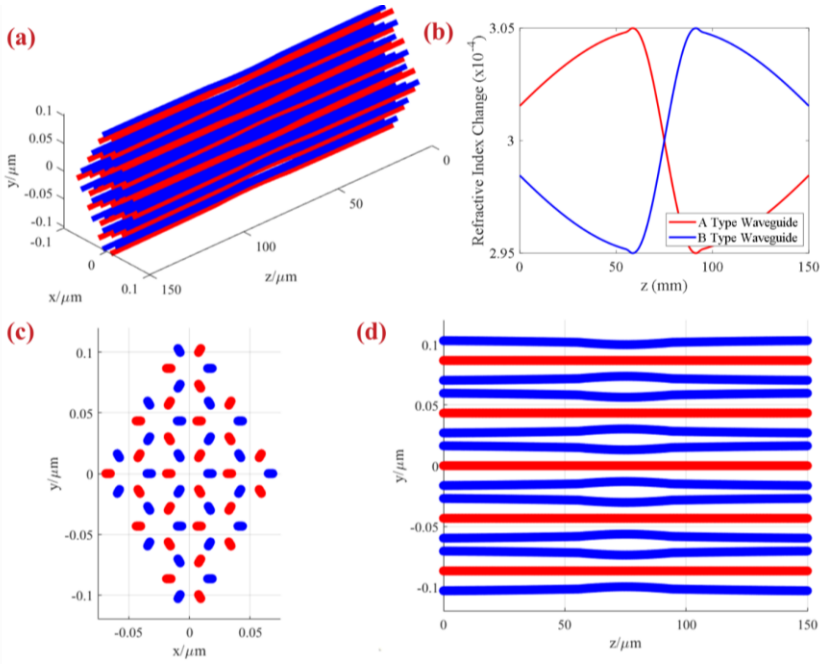

Figure 50 (a) The birdview schematic of the 3-D waveguide array array, (b) the cross-section at the input facet, (c) the top view of the array along the propagation direction, (d) the microscopic view of the input facet, and (e) one single period of the refractive index modulation along the propagation direction of A type waveguide and B type waveguide.

Light was injected into the pumping structure from a straw structure [143]. which is able to generate an output from two waveguides that are equal in intensity but π shifted in phase difference. The waveguide array consists of another 54-waveguide array with one input, indicated as the straw waveguide. The schematic of the straw structure is presented in Figure 51(a). Light from a single-mode fiber was injected into the dark blue straw waveguide. While the two off-

corner waveguides will be illuminated after propagation. Figure 51(c) shows the microscopic image. Figure 51(d) shows the measured output at the wavelength of 1550 nm, the waveguides were modeled using a hyper-Gaussian distribution, and measured to be 8.91 μm and 5.83 μm at half maximum of the major and minor axis.

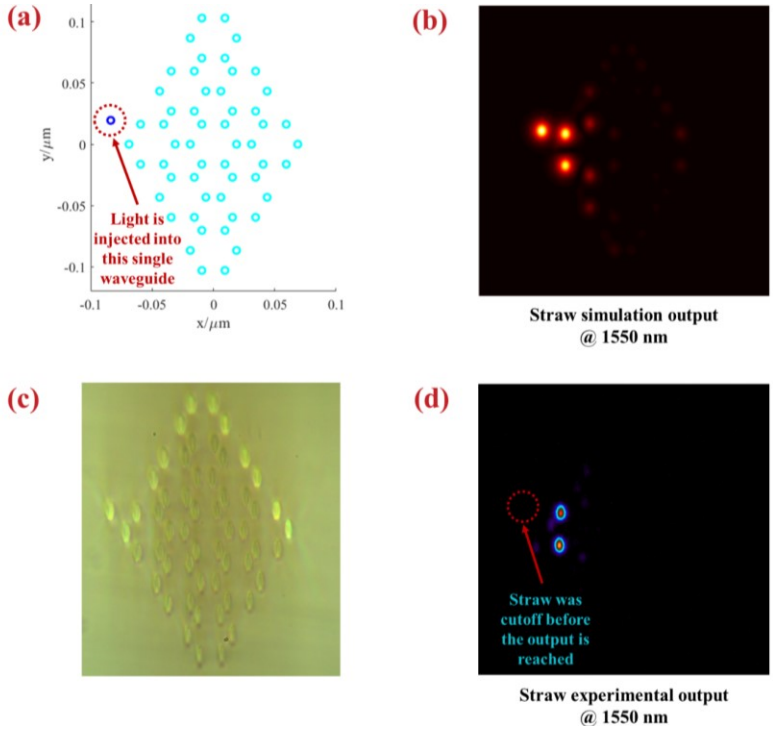

Figure 51 (a) The schematic of the input facet of the straw array, (b) the simulation of the output of the straw array at 1550 nm wavelength, (c) the microscopic view of the output facet, and (d) the experimental output of the straw waveguide.

Meanwhile, the pumping chip was written on a 15 cm glass chip. Figure 52(a) shows the microscopic image of the cross-section. To verify the pumping structure, the two chips were positioned in a cascaded manner. A single-mode input unit was first butt-coupled into the straw structure, then fixed using optical-quality UV-cure epoxy. Then the straw chip was mounted on a 3-D precise motion stage and coupled to the pumping chip (Figure 52(b)). Figure 52(c) presents a

setup of the characterization. Light was injected into the two off-corner waveguides from the straw chip into the corresponding waveguides on the pumping chip. As light propagates inside the pumping chip, corner to corner pumping was verified experimentally. Figure 52(e) demonstrate the transport of light as predicted in the simulation (Figure 52(d)). The transport provides the first experimental verification of 3-D second-order topological insulator, that is equivalent to 1-D Thouless pump, and the 2D quantum Hall effect in electron gas.

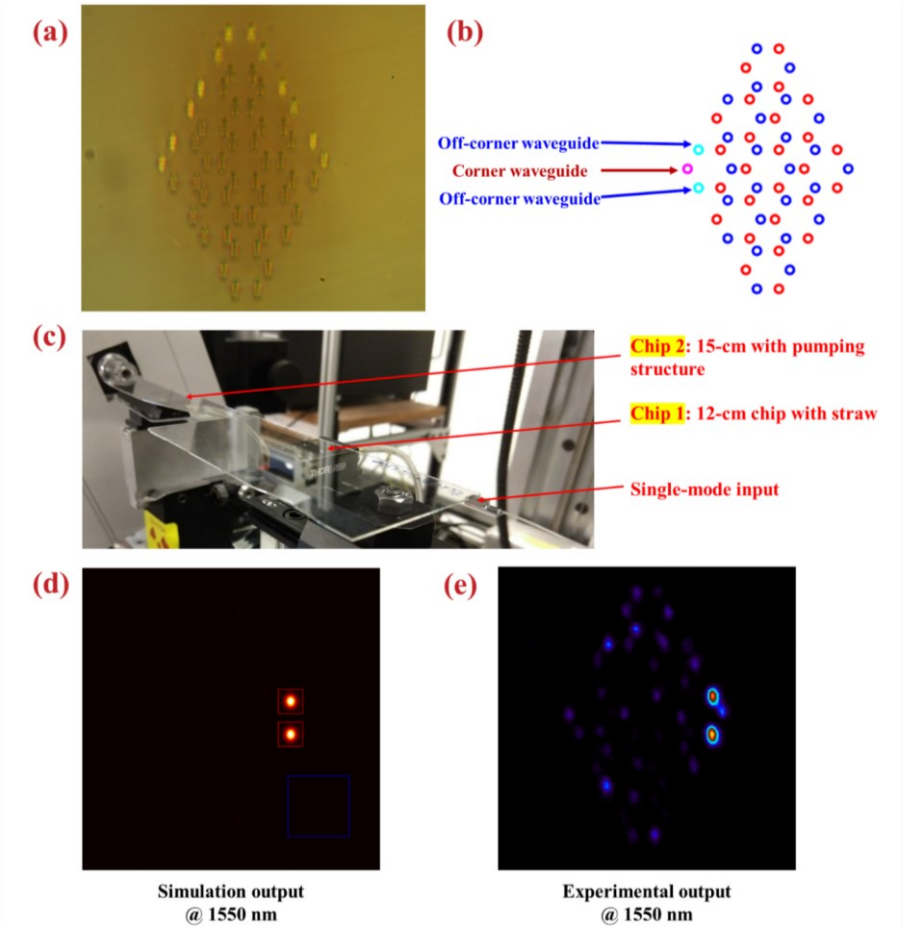

Figure 52 (a) The microsopic photo, (b) the schematic of the pumping chip input, (c) Photo of the measurement setup, (d) the simulation of the output of the pumping structure at 1550 nm wavelength, and (e) the experimental output

6.0 Femtosecond Laser Direct Writing of Photonic Devices

Optical devices on bulk substrates are widely used in applications such as telecommunication, astronomy, microscopic imaging. While commercial photonic devices are fabricated using lithographical method, large and expensive semiconductor manufacturing facilities and complicated fabrication procedure are required, and a new prototype usually requires creation of expensive phase masks. These characteristics make the process time and cost consuming. Contrarily, the femtosecond laser is a powerful alternative tool to fabricate these photonic devices. The fabrication process is rapid and simple at a reduced cost. Moreover, the fabricated devices are all-photonics. Femtosecond laser fabricated devices are able to directly perform the optical signal processing through optics physics, and thus reduces the cost of energy loss from the light-electronic-light conversion. Through the nonlinear absorption processes, femtosecond laser can fabricate true 3-D structures all-photonics structures on a wide range of materials and platforms. This chapter presents the preliminary results of the design and fabrication of novel photonics devices using femtosecond laser fabrication.

6.1 Optical Interconnect for Dual-Cladding Multicore Fiber

A dual-cladding optical fiber with a Er-doped secondary cladding has been used in optical telecommunication for signal amplification and fiber laser oscillator for improved conversion frequency. In contrast with a normal optical fiber with two layers of a core and a cladding, a dual-cladding fiber contains three layers including a core and two claddings composed of different

materials. In the telecommunication applications, as the signal light would transmit through the optical fiber core, the inner cladding layer is usually rare-earth doped, which can absorb a pumping light at a different wavelength to amplify the signal transmitted inside the fiber core. There are two common approaches to pump light into cladding-pumped optical fiber. In the end pumping approach, both pump light and signal light are coupled from the end facet of the fiber. However, the method suffers from signal loss and the core signal might degrade. Side pumping addresses this challenge by injecting light into the inner cladding through sides of the fiber and has been traditionally achieved using methods such as V-grooves, embedded mirrors, downsized capillaries, and down-tapered coreless fibers. However, the coupling efficiency is usually low due to the mismatch between the unsymmetrical shape of the pump region, which limit the pumping efficiency. Moreover, both methods can hardly address the challenges of novel optical fiber designs [145]–[147].

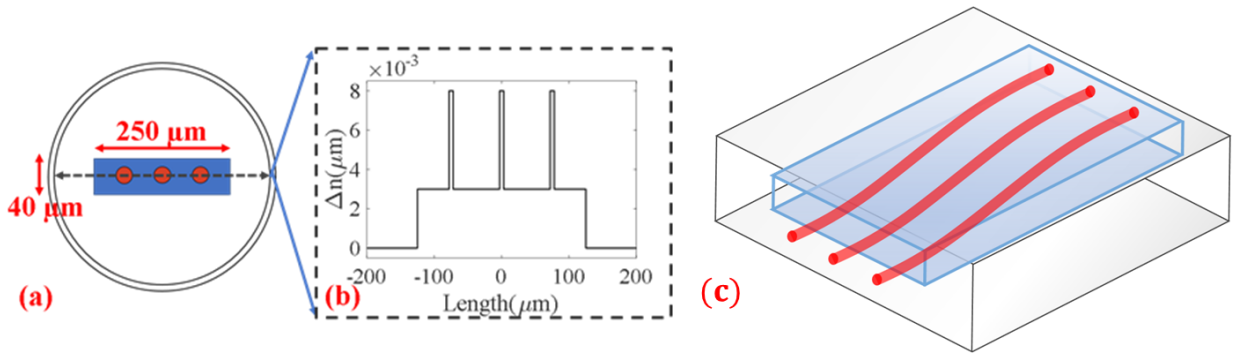

Figure 53 (a) Schematic of the dual-cladding multi-core optical fiber (NEC Corporation Inc.), (b) the refractive index profile of the fiber in the axial direction, and (c) the schematic of the femtosecond laser fabricated optical interconnect.

A multicore fiber contains several fiber cores that are uncoupled from each other. Each core delivers signal light. They are widely used in telecommunication applications to expand the

signal bandwidth. Figure 53 (a) shows a diagram of the dual-cladding multi-core fiber designed by NEC Corporation. All the three cores will transmit 1550-nm signal light and are embedded in a common inner cladding doped with Er ions. The inner cladding is able to guide the pump light and amplify optical signal light. Its refractive index profile is shown in Figure 53(b).

The motivation behind the project is to design and fabricate a novel 3-D waveguide structure that can perform coupling and decoupling between the signal and pump light between the source and the designed fiber region geometry shape with minimal coupling loss. Figure 53(c) presents a novel solution of a photonic circuit design which can be fabricated using the femtosecond laser direct writing method. An integrated cladding-pump fiber amplifier coupler can be integrated in bulk fused silica to simultaneously combine the signal light and the pump light. The waveguide allows simultaneously coupling of signal light into three fiber cores from different sources injected from single-mode fibers, and the transmission of light from a multimode rectangular shaped laser diode bar.

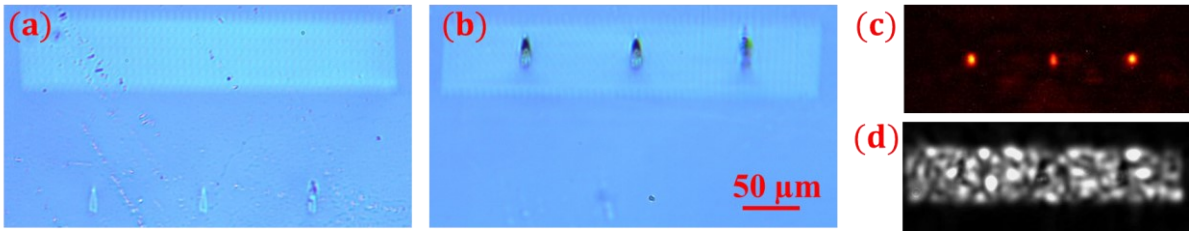

Figure 54 The microscopic image of the (a) input and (b) output facet of the fused silica and the measured output mode pattern (a) of the signal light at 1550 nm light and (b) of the 980 nm pump laser diode light.

The design was realized on a fused silica chip with the length of 25 mm and thickness of 1 mm. Two sections were written, including a rectangular region with lower index of 3×10^{-3} for the insertion of pump light from a laser diode bar pump source and three single-mode waveguides

with an index of 8×10^{-3} for the delivery of signal light to the three fiber cores. The curves of these waveguides were designed with simulation so that the bending induced propagation loss in 3-D space can be minimized. The refractive index was also designed to match that of the designed fiber, in order to optimize the coupling loss between the glass chip and the specialty optical fiber.

For the fabrication process, the pumping waveguide region was first written with 760-nJ pulse energy at a speed of 10 mm/s. The size of the single spot beam was measured so that a layer-to-layer transversal scanning scheme is used. Then, three waveguides for each core are written on top of the rectangular shaped pumping waveguide, with 810-nJ pulse energy, 1-mm/s speed. The three waveguides are 75 μm away from each other. At the input side, the waveguides for signal light delivery are 100 μm below the pump waveguide region. During the propagation, these waveguides merge into the pump waveguide along a designed trace. Center of the pump waveguides is 100 μm below the surface of the chip sample (Figure 54 (a) and (b)). The light transmission of the pump region was measured with a laser diode at the wavelength of 650 nm. The signal waveguides were measured with both 1550 nm and 980 nm light sources using butt-coupling with three single-mode fibers simultaneously. Three different signals with different intensities were used to test the transmission. The mode pattern of 1550 nm light at the end surface is shown. Single-mode propagation behavior was also verified using an NIR camera, as shown in Figure 54(c). The transmission of 980 nm multimode was also verified in Figure 54(d) using a VIS range CCD camera. The coupling presents minimal transmission loss.

It has been proved that coupling can be achieved from specialty optical fiber to pumping and transformed into various shapes using the femtosecond laser direct writing method. Another geometry of the dual-cladding optical fiber is a ring-shaped secondary cladding. In this way, the multicore fiber cores can be arranged in a circular way around the center. This allows maximum

distance between each core and a minimal cross-talk between cores over long-distance transmission. Figure 55 shows another optical interconnect structure fabricated from femtosecond laser direct writing. It allows the smooth and low-loss coupling of pump light from a rectangular shaped laser diode bar output to a ring-shaped secondary fiber cladding, while the size of both output matches that of the laser bar and fiber cladding. The structure was carefully designed to minimize the propagation loss and bending loss.

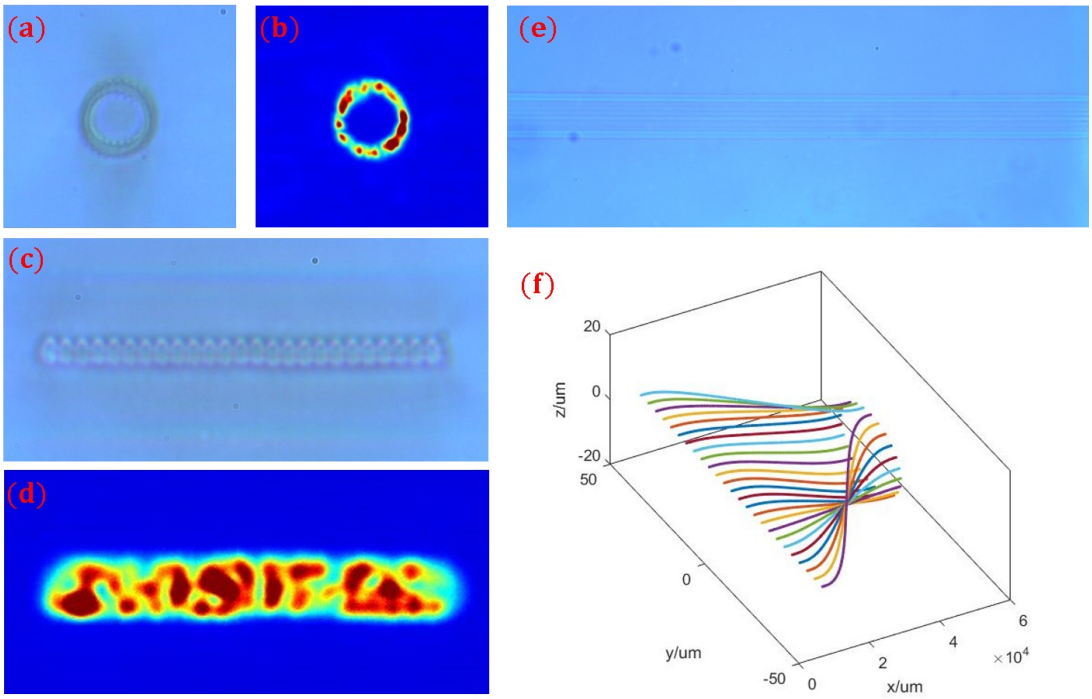

Figure 55 (a) the microscopic photo of the output facet, (b) output mode field at 1550 nm, (c) the microscopic photo of the input facet, (d) input mode field at 1550 nm, (e) top view of the chip, and (f) schematic.

In sum, femtosecond laser has enabled the fabrication novel optical interconnect design in 3-D space. Such optical interconnects can be customized to different geometry designs of fiber core and claddings. Moreover, through calibration of the femtosecond laser writing induced index

change, the pumping and coupling efficiency can also be optimized to that of the light source and fiber design, and the device has a minimal insertion loss.

6.2 Close-to-Surface Waveguides on Display Glass

Optical substrate has a large commercial application. There are many well-established optical substrates, such as display glass. The smart phone market has experienced astonishing growth the recent decade. Gorilla glass produced by Corning Inc. has been widely used as the phone screen. It is a special kind of glass has an extra chemical strengthened layer on top of the bulk, which can prevent the phone screen from physical damage and scratches. Though it is highly desirable to integrate optical devices directly on a phone screen to make the phone "smarter", there are several challenges for such optical designs. The technique has to preserve the integrity and optical quality of the glass, small in scale, and transparent to eye. Besides, due to the limited thickness of a phone screen, the difficulty increases when fabricating devices close-to-surface without introducing damage to the actual glass surface.

Femtosecond laser direct writing has proved to be a good candidate. Waveguide, which is the basic unit of a photonic circuit, is fabricated on a chemically strengthened glass produced by Corning Inc. The spatial scale of the fabrication technique was characterized by writing waveguides at different depth of the glass. Figure 34 shows channel waveguides fabricated by horizontally translating the motion stage across the laser beam focus, forming a light guiding line across the transparent bulk. Waveguides at a depth between 40 μm to 500 μm were written on the 10-cm long, 1-mm thick chemically strengthened glass. These waveguides were written using an average power of 100 to 200 mW, a pulse width of pulse width 270 fs, 250-kHz repetition rate, at

1 to 10 mm/s speed, using an 80X objective (NA 0.75). The mode guiding behavior was measured through by butt coupling 1550-nm light from a single-mode optical fiber. Then the mode profile was imaged using a 2-f imaging system and a NIR camera. Though single-mode guiding was verified, the waveguide suffers from the spherical aberration. Meanwhile, it is of high importance that waveguides can be inscribed in close proximity to glass surface in order to integrate compact devices on a phone display. However, challenges exist to fabricate waveguide that are close to surface. The closer is the focus to the glass surface, the stronger is the objective focus strength, and the lower is the power threshold required to induce refractive index change.

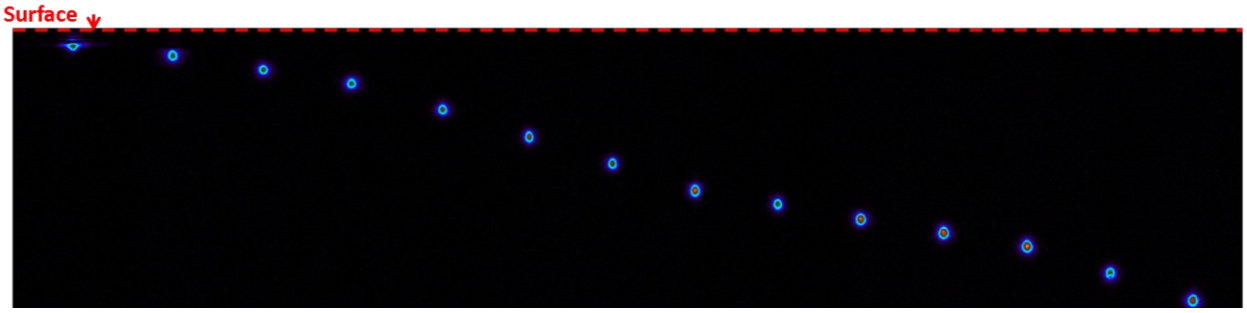

Figure 56 (a) Transmission of mode fields at 1550nm at various depth of a chemically strengthened glass, (b) the chemical strengthened layer guiding 1550nm light, (c) the backscatteirng profile of the bulk waveguide, (d) zoomed in profile at the waveguide showing optical loss

The above-mentioned challenges can be compensated from dynamically tuning the power and speed. Waveguides that were close to the glass surface will be inside the chemically strengthened layer. Using 200-fs pulse width, 130 to 160 mW average power, 250-kHz repetition rate, the close-to-surface waveguides were fabricated. The laser beam was focused on different depths through an 80X objective (NA 0.75), and the glass sample was translated at 1 mm/s speed using a multi-scan method. Figure 57 presents the microscopic photo and mode field of the

waveguides. Waveguides with less than 10 μm depth suffer from significant loss and the mode field of the waveguide close to the chemically strengthened layer suffers from much distortion. These are due to the inhomogeneities inside the chemical-strengthened layer.

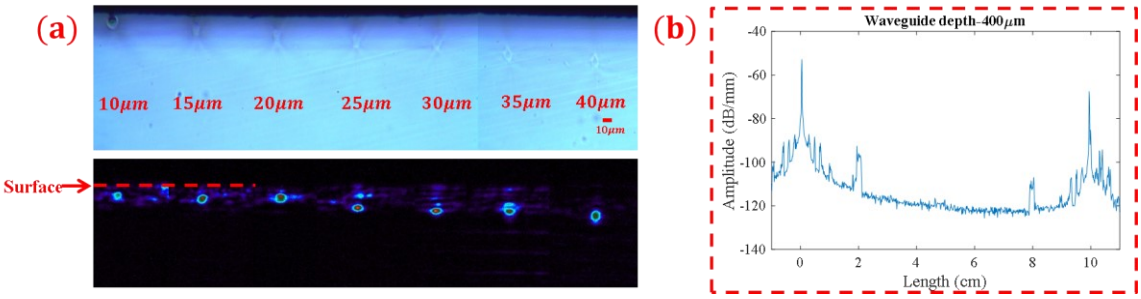

Figure 57 (a) Waveguides on a chemically strengthened glass close to surface and (b) the backscattering profile of a bulk waveguide.

Measurements of the propagation loss are based on OFDR-based method. The femtosecond laser written waveguides was characterized by an OBR. The NIR laser output from the OBR was butt coupled to the waveguide through a single-mode fiber into the waveguide. Index matching gel was applied to both ends of the waveguide to mitigate the impact of Fresnel reflection from the two the substrate facets. Figure 57(b) shows the measured result. The peaks in the trace denote the front and back facets of the substrate, respectively. By linear fitting the trace between the two reflection peaks, the propagation loss of the waveguide is indicated by the slope of the fitted line. The propagation loss was found to be 0.12 dB/cm.

7.0 Conclusion and Future Works

Femtosecond laser fabrication of optical devices is emerging as a powerful technique to compete with the well-established semiconductor-based method. With only a laser system, a beam delivery system, and a three-axis motion stage, femtosecond laser can complete fast prototyping of photonic devices in the lab environment at reduced cost. The multiple steps involved in the semiconductor-based manufacturing approaches can be saved in the femtosecond laser fabrication that by simply running a pre-programmed code, a true 3-D devices can be written inside a transparent substrate. The fabrication can be completed on many types of commercially available materials and platforms. By careful control of the nonlinear laser-material interactions in the femtosecond time scale and nanometer spatial scale, femtosecond laser is a flexible and versatile cross-platform manufacturing method to fabricate 3-D photonic structures on distinct transparent substrates.

The first part of the dissertation demonstrates femtosecond laser fabrication of optical fiber sensors in silica and sapphire optical fibers with spherical surfaces. The sensors have demonstrated improved thermal stability under an extreme temperature of 1000°C. Femtosecond laser is able to inscribe the high-temperature stable Type-II modification inside an optical fiber. Femtosecond laser direct written fiber sensors are fabricated by depositing energy at a micrometer scale focal volume inside the fiber core. Both the Fiber Bragg Grating sensor and the Intrinsic Fabry-Perot Interferometer arrays are demonstrated with high performance and low insertion loss. The temperature stability and multiplexability are also presented. Using a reel-to-reel setup, femtosecond laser-induced artificial Rayleigh backscattering centers can be continuously inscribed on meters of optical fiber. The Rayleigh enhanced section can improve the SNR and accuracy of

OFDR-based distributed sensing, while the exceptional thermal stability of nanograting also contributed to improved harsh environmental resilience under fast neutron radiation.

The second part of the dissertation presents the fabrication of 3-D photonic lattices and optic devices on glass substrate with flat surfaces. Inspired from the resemblance between the Maxwell and the Schrodinger equations, the light propagation inside a waveguide array fabricated by femtosecond laser direct writing can be used to emulate the electron transportation inside a lattice. The true 3-D high-density femtosecond laser-written waveguide circuits has enabled powerful possibilities in some of the most state-of-art photonic areas such as quantum information processing and topological insulator lasers. Through control of the spatial profile and the fabrication parameters, complicated and low-loss waveguide arrays can be fabricated with varying index profile. The dissertation presents the experimental verification of three projects, including the lattice braiding, Thouless pumping, and the higher-order topological pumping. The fabrication of photonic bulk devices for communication application was also demonstrated.

Many questions are still open for the physics behind the femtosecond laser-material interaction. Though the area of ultrafast optics has attracted much research curiosity, the material modification takes place at the time scale of femtoseconds, which is a time resolution much faster than what conventional electronic cameras and sensors can resolve. While many optics methods have been proposed to resolve this issue, this challenge can be addressed from the backward direction. Through the investigation of the modifications and their dependence on the laser parameters, the assumption and physics model can be constructed. A following work of this dissertation will be to continue study the mechanisms of femtosecond laser-material interaction through observation of the laser-induced modification, using a similar method presented in Chapter 3.

Topological photonics is a fast-growing area. The combination of fundamental physics and optical engineering can lead to the design of novel photonic devices, i.e. topological insulator laser, quantum information processing unit. Femtosecond laser is a promising technique to fabricate such 3-D designs on an all-optical platform with high efficiency at reduced cost. Meanwhile, there are still many challenges waiting to be solved to improve the optical quality of high-density waveguide circuits. One of those challenges is the optical aberration in the fabrication system. The spherical aberration inside an imaging system poses a constraint on the depth dimension of the photonic structure design. Another challenge is the asymmetrical cross-section, which will lead to distorted mode field and undesirable polarization dependent optical behavior. To advance the research described in the dissertation, various dynamic light adjustment techniques have been attempted with minimal optical power loss. Some of the solutions are a beam shaping techniques using a spatial light modulator or deformable mirror arrays, as well as aberration-resistant structural geometries designed using machine learning based models.

Moreover, the versatility of materials and platforms, as one of the most advantageous characteristics of femtosecond laser fabrication, can also be further exploited. While this dissertation has explored the device fabrication on silica and sapphire based bulks, the techniques can be transferred to fabricate devices on other types of materials, such as polymer, metal, ceramic, and bio-tissues. While each of these materials and platforms exhibits distinct fabrication challenges, the optical design can be realized by manipulating the laser-material interactions. Different kinds of nonthermal and nonlinear absorptions can be exploited to fabricate devices with novel functionalities by tuning a large femtosecond laser parameter space.

In sum, the dissertation studies the optics science of femtosecond laser-matter interaction to fabricate 3-D photonic devices for studies of optics science and for photonics applications in

communication and sensing. Some subsequent studies include further exploration of the fabrication technique for new designs and novel material substrates.

Bibliography

[1] K. M. Davis, K. Miura, N. Sugimoto, and K. Hirao, "Writing waveguides in glass with a femtosecond laser," *Optics Letters*, vol. 21, no. 21, p. 1729, Nov. 1996, doi: 10.1364/ol.21.001729.

[2] G. della Valle, R. Osellame, and P. Laporta, "Micromachining of photonic devices by femtosecond laser pulses," *Journal of Optics A: Pure and Applied Optics*, vol. 11, no. 1, 2009, doi: 10.1088/1464-4258/11/1/013001.

[3] F. Chen and J. R. V. de Aldana, "Optical waveguides in crystalline dielectric materials produced by femtosecond-laser micromachining," *Laser and Photonics Reviews*, vol. 8, no. 2, pp. 251–275, 2014, doi: 10.1002/lpor.201300025.

[4] D. Choudhury, J. R. Macdonald, and A. K. Kar, "Ultrafast laser inscription: Perspectives on future integrated applications," *Laser and Photonics Reviews*, vol. 8, no. 6, pp. 827–846, 2014, doi: 10.1002/lpor.201300195.

[5] S. Gross and M. J. Withford, "Ultrafast-laser-inscribed 3D integrated photonics: Challenges and emerging applications," *Nanophotonics*, vol. 4, no. 1, pp. 332–352, 2015, doi: 10.1515/nanoph-2015-0020.

[6] A. Y. Vorobyev and C. Guo, "Direct femtosecond laser surface nano/microstructuring and its applications," *Laser and Photonics Reviews*, vol. 7, no. 3, pp. 385–407, 2013, doi: 10.1002/lpor.201200017.

[7] H. Chen, M. Buric, P. R. Ohodnicki, J. Nakano, B. Liu, and B. T. Chorpening, "Review and perspective: Sapphire optical fiber cladding development for harsh environment sensing," *Applied Physics Reviews*, vol. 5, no. 1, p. 011102, Mar. 2018, doi: 10.1063/1.5010184.

[8] J. L. Rempe *et al.*, "Enhanced in-pile instrumentation at the advanced test reactor," *IEEE Transactions on Nuclear Science*, vol. 59, no. 4 PART 2, pp. 1214–1223, 2012, doi: 10.1109/TNS.2011.2174066.

[9] P. Calderoni, D. Hurley, J. Daw, A. Fleming, and K. McCary, "Innovative sensing technologies for nuclear instrumentation," in *I2MTC 2019 - 2019 IEEE International Instrumentation and Measurement Technology Conference, Proceedings*, May 2019, vol. 2019-May, doi: 10.1109/I2MTC.2019.8827129.

[10] S. J. Mihailov *et al.*, "Extreme environment sensing using femtosecond laser-inscribed fiber bragg gratings," *Sensors (Switzerland)*, vol. 17, no. 12, 2017, doi: 10.3390/s17122909.

[11] S. J. Mihailov, “Fiber bragg grating sensors for harsh environments,” *Sensors*, vol. 12, no. 2, pp. 1898–1918, 2012, doi: 10.3390/s120201898.

[12] D. Tan, K. N. Sharafudeen, Y. Yue, and J. Qiu, “Femtosecond laser induced phenomena in transparent solid materials: Fundamentals and applications,” *Progress in Materials Science*, vol. 76, no. September 2015, pp. 154–228, 2016, doi: 10.1016/j.pmatsci.2015.09.002.

[13] R. Osellame, G. Cerullo, and R. Ramponi, “Femtosecond Laser Micromachining: Photonic and Microfluidic Devices in Transparent Materials,” *Topics in Applied Physics*, vol. 123, pp. 265–292, 2012, doi: 10.1007/978-3-642-23366-1.

[14] C. B. Schaffer, A. Brodeur, and E. Mazur, “Laser-induced breakdown and damage in bulk transparent materials induced by tightly focused femtosecond laser pulses,” *Measurement Science and Technology*, vol. 12, no. 11, pp. 1784–1794, 2001, doi: 10.1088/0957-0233/12/11/305.

[15] R. R. Gattass and E. Mazur, “Femtosecond laser micromachining in transparent materials,” *Nature Photonics*, vol. 2, no. 4, pp. 219–225, Apr. 2008, doi: 10.1038/nphoton.2008.47.

[16] G. della Valle, R. Osellame, and P. Laporta, “Micromachining of photonic devices by femtosecond laser pulses,” *Journal of Optics A: Pure and Applied Optics*, vol. 11, no. 1, 2009, doi: 10.1088/1464-4258/11/1/013001.

[17] V. Tielen and Y. Bellouard, “Three-dimensional glass monolithic micro-flexure fabricated by femtosecond laser exposure and chemical etching,” *Micromachines*, vol. 5, no. 3, pp. 697–710, 2014, doi: 10.3390/mi5030697.

[18] G. della Valle, R. Osellame, and P. Laporta, “Micromachining of photonic devices by femtosecond laser pulses,” *Journal of Optics A: Pure and Applied Optics*, vol. 11, no. 1, 2009, doi: 10.1088/1464-4258/11/1/013001.

[19] K. Itoh, W. Watanabe, S. Nolte, and C. B. Schaffer, “Ultrafast processes for bulk modification of transparent materials,” *MRS Bulletin*, vol. 31, no. 8, pp. 620–625, 2006, doi: 10.1557/mrs2006.159.

[20] A. Szameit and S. Nolte, “Discrete optics in femtosecond-laserwritten photonic structures,” *Journal of Physics B: Atomic, Molecular and Optical Physics*, vol. 43, no. 16, 2010, doi: 10.1088/0953-4075/43/16/163001.

[21] R. R. Thomson and G. Cerullo, “Ultrafast laser inscription of photonic devices in bulk dielectrics,” in *Ultrafast Nonlinear Optics*, Springer International Publishing, 2013, pp. 323–350.

[22] M. Ams, G. D. Marshall, and M. J. Withford, “Study of the influence of femtosecond laser polarisation on direct writing of waveguides,” *Optics Express*, vol. 14, no. 26, p. 13158, 2006, doi: 10.1364/oe.14.013158.

[23] M. Haque and P. R. Herman, “Chemical-assisted femtosecond laser writing of optical resonator arrays,” *Laser and Photonics Reviews*, vol. 9, no. 6, pp. 656–665, 2015, doi: 10.1002/lpor.201500062.

[24] R. Osellame, H. J. W. M. Hoekstra, G. Cerullo, and M. Pollnau, “Femtosecond laser microstructuring: An enabling tool for optofluidic lab-on-chips,” *Laser and Photonics Reviews*, vol. 5, no. 3. pp. 442–463, May 2011, doi: 10.1002/lpor.201000031.

[25] J. Zhang, M. Gecevičius, M. Beresna, and P. G. Kazansky, “Seemingly unlimited lifetime data storage in nanostructured glass,” *Physical Review Letters*, vol. 112, no. 3, pp. 1–5, 2014, doi: 10.1103/PhysRevLett.112.033901.

[26] D. L. N. Kallepalli, A. M. Alshehri, D. T. Marquez, L. Andrzejewski, J. C. Scaiano, and R. Bhardwaj, “Ultra-high density optical data storage in common transparent plastics,” *Scientific Reports*, vol. 6, no. 1, pp. 1–10, 2016, doi: 10.1038/srep26163.

[27] A. Seri *et al.*, “Laser-written integrated platform for quantum storage of heralded single photons,” *Optica*, vol. 5, no. 8, p. 934, 2018, doi: 10.1364/optica.5.000934.

[28] S. M. Eaton *et al.*, “Transition from thermal diffusion to heat accumulation in high repetition rate femtosecond laser writing of buried optical waveguides,” *Optics Express*, vol. 16, no. 13, p. 9443, 2008, doi: 10.1364/oe.16.009443.

[29] C. Hnatovsky *et al.*, “Pulse duration dependence of femtosecond-laser-fabricated nanogratings in fused silica,” *Applied Physics Letters*, vol. 87, no. 1, 2005, doi: 10.1063/1.1991991.

[30] S. Richter, M. Heinrich, S. Döring, A. Tünnermann, S. Nolte, and U. Peschel, “Nanogratings in fused silica: Formation, control, and applications,” *Journal of Laser Applications*, vol. 24, no. 4, p. 042008, 2012, doi: 10.2351/1.4718561.

[31] Z. Wang, F. Shen, L. Song, X. Wang, and A. Wang, “Multiplexed fiber fabry-pérot interferometer sensors based on ultrashort bragg gratings,” *IEEE Photonics Technology Letters*, vol. 19, no. 8, pp. 622–624, Apr. 2007, doi: 10.1109/LPT.2007.894361.

[32] Y. Wang, J. Gong, B. Dong, D. Y. Wang, T. J. Shillig, and A. Wang, “A Large Serial Time-Division Multiplexed Fiber Bragg Grating Sensor Network,” *Journal of Lightwave Technology*, vol. 30, no. 17, pp. 2751–2756, 2012, doi: 10.1109/JLT.2012.2205897.

[33] A. Martinez, I. Y. Khrushchev, and I. Bennion, “Thermal properties of fibre Bragg gratings inscribed point-by-point by infrared femtosecond laser,” *Electronics Letters*, vol. 41, no. 4, pp. 176–178, Feb. 2005, doi: 10.1049/el:20057898.

[34] S. J. Mihailov *et al.*, “Extreme environment sensing using femtosecond laser-inscribed fiber bragg gratings,” *Sensors (Switzerland)*, vol. 17, no. 12, 2017, doi: 10.3390/s17122909.

[35] B. Guo, J. Sun, Y. Lu, and L. Jiang, "Ultrafast dynamics observation during femtosecond laser-material interaction," *International Journal of Extreme Manufacturing*, vol. 1, no. 3, p. 032004, 2019, doi: 10.1088/2631-7990/ab3a24.

[36] C. B. Schaffer, A. Brodeur, J. F. García, and E. Mazur, "Micromachining bulk glass by use of femtosecond laser pulses with nanojoule energy," *Optics Letters*, vol. 26, no. 2, p. 93, 2001, doi: 10.1364/ol.26.000093.

[37] D. Grobnic, C. W. Smelser, S. J. Mihailov, R. B. Walker, and P. Lu, "Fiber Bragg gratings with suppressed cladding modes made in SMF-28 with a femtosecond IR laser and a phase mask," *IEEE Photonics Technology Letters*, vol. 16, no. 8, pp. 1864–1866, 2004, doi: 10.1109/LPT.2004.831239.

[38] S. J. Mihailov *et al.*, "Fiber Bragg gratings (FBG) made with a phase mask and 800 nm femtosecond radiation," *Conference on Optical Fiber Communication, Technical Digest Series*, vol. 2003-Janua, no. 12, p. PD30.1-PD30.3, 2003, doi: 10.1109/OFC.2003.316135.

[39] R. J. Williams, R. G. Krämer, S. Nolte, and M. J. Withford, "Femtosecond direct-writing of low-loss fiber Bragg gratings using a continuous core-scanning technique," *Optics Letters*, vol. 38, no. 11, p. 1918, 2013, doi: 10.1364/ol.38.001918.

[40] P. Lu *et al.*, "Plane-by-Plane Inscription of Grating Structures in Optical Fibers," *Journal of Lightwave Technology*, vol. 36, no. 4, pp. 926–931, 2018, doi: 10.1109/JLT.2017.2750490.

[41] A. S. Chernikov, K. S. Khorkov, D. A. Kochuev, R. v. Chkalov, V. G. Prokoshev, and N. N. Davydov, "Line-by-line fiber Bragg grating fabrication by femtosecond laser radiation," in *Journal of Physics: Conference Series*, Mar. 2019, vol. 1164, no. 1, doi: 10.1088/1742-6596/1164/1/012015.

[42] Y. Lai, Y. Chen, and M. W. O. Cheong, "Low-loss, high reflectivity, first-order, pitch-by-pitch fiber Bragg grating fabrication in truly free-standing single-mode fiber," in *Journal of Physics: Conference Series*, Feb. 2016, vol. 679, no. 1, p. 012055, doi: 10.1088/1742-6596/679/1/012055.

[43] J. Thomas, C. Voigtländer, R. G. Becker, D. Richter, A. Tünnermann, and S. Nolte, "Femtosecond pulse written fiber gratings: A new avenue to integrated fiber technology," *Laser and Photonics Reviews*, vol. 6, no. 6, pp. 709–723, 2012, doi: 10.1002/lpor.201100033.

[44] D. Grobnic, C. Hnatovsky, and S. J. Mihailov, "Low loss Type II regenerative Bragg gratings made with ultrafast radiation," *Optics Express*, vol. 24, no. 25, p. 28704, 2016, doi: 10.1364/oe.24.028704.

[45] D. Grobnic, C. W. Smelser, S. J. Mihailov, and R. B. Walker, "Long-term thermal stability tests at 1000 °C of silica fibre Bragg gratings made with ultrafast laser radiation," *Measurement Science and Technology*, vol. 17, no. 5, pp. 1009–1013, 2006, doi: 10.1088/0957-0233/17/5/S12.

[46] C. Hnatovsky, D. Grobnic, and S. J. Mihailov, "High-temperature stable π-phase-shifted fiber Bragg gratings inscribed using infrared femtosecond pulses and a phase mask," *Optics Express*, vol. 26, no. 18, p. 23550, 2018, doi: 10.1364/oe.26.023550.

[47] M. A. S. M. A. S. Zaghloul *et al.*, "Radiation resistant fiber Bragg grating in random air-line fibers for sensing applications in nuclear reactor cores," *Optics Express*, vol. 26, no. 9, p. 11775, 2018, doi: 10.1364/oe.26.011775.

[48] S. E. Wei *et al.*, "Thermal stability of type II modifications by IR femtosecond laser in silica-based glasses," *Sensors (Switzerland)*, vol. 20, no. 3, 2020, doi: 10.3390/s20030762.

[49] E. Bricchi and P. G. Kazansky, "Extraordinary stability of anisotropic femtosecond direct-written structures embedded in silica glass," *Applied Physics Letters*, vol. 88, no. 11, pp. 2–4, 2006, doi: 10.1063/1.2185587.

[50] C. Hnatovsky, D. Grobnic, D. Coulas, M. Barnes, and S. J. Mihailov, "Self-organized nanostructure formation during femtosecond-laser inscription of fiber Bragg gratings," *Optics Letters*, vol. 42, no. 3, p. 399, 2017, doi: 10.1364/ol.42.000399.

[51] S. J. Mihailov, C. Hnatovsky, and D. Grobnic, "Novel type II bragg grating structures in silica fibers using femtosecond lasers and phase masks," *Journal of Lightwave Technology*, vol. 37, no. 11, pp. 2549–2556, 2019, doi: 10.1109/JLT.2018.2866784.

[52] Y. Lai, K. Zhou, K. Sugden, and I. Bennion, "Point-by-point inscription of first-order fiber Bragg grating for C-band applications," *Optics Express*, vol. 15, no. 26, p. 18318, Dec. 2007, doi: 10.1364/oe.15.018318.

[53] D. Grobnic, C. Hnatovsky, and S. J. Mihailov, "Thermally Stable Type II FBGs Written Through Polyimide Coatings of Silica-Based Optical Fiber," *IEEE Photonics Technology Letters*, vol. 29, no. 21, pp. 1780–1783, 2017, doi: 10.1109/LPT.2017.2752128.

[54] H. Y. Choi, K. S. Park, S. J. Park, U.-C. Paek, B. H. Lee, and E. S. Choi, "Miniature fiber-optic high temperature sensor based on a hybrid structured Fabry–Perot interferometer," *Optics Letters*, vol. 33, no. 21, p. 2455, 2008, doi: 10.1364/ol.33.002455.

[55] J. Wang, B. Dong, E. Lally, J. Gong, M. Han, and A. Wang, "Multiplexed high temperature sensing with sapphire fiber air gap-based extrinsic Fabry–Perot interferometers," *Optics Letters*, vol. 35, no. 5, p. 619, 2010, doi: 10.1364/ol.35.000619.

[56] Y. Zhang, L. Yuan, X. Lan, A. Kaur, J. Huang, and H. Xiao, "High-temperature fiber-optic Fabry–Perot interferometric pressure sensor fabricated by femtosecond laser: erratum," *Optics Letters*, vol. 39, no. 1, p. 17, 2014, doi: 10.1364/ol.39.000017.

[57] C. R. Liao, T. Y. Hu, and D. N. Wang, "Optical fiber Fabry-Perot interferometer cavity fabricated by femtosecond laser micromachining and fusion splicing for refractive index sensing," *Optics Express*, vol. 20, no. 20, p. 22813, 2012, doi: 10.1364/oe.20.022813.

[58] M. Wang, M. Yang, J. Cheng, G. Zhang, C. R. Liao, and D. N. Wang, "Fabry-pérot interferometer sensor fabricated by femtosecond laser for hydrogen sensing," *IEEE Photonics Technology Letters*, vol. 25, no. 8, pp. 713–716, 2013, doi: 10.1109/LPT.2013.2241421.

[59] T. Paixão, F. Araújo, and P. Antunes, "Highly sensitive fiber optic temperature and strain sensor based on an intrinsic Fabry–Perot interferometer fabricated by a femtosecond laser," *Optics Letters*, vol. 44, no. 19, p. 4833, 2019, doi: 10.1364/ol.44.004833.

[60] Y.-J. Rao, M. Deng, D.-W. Duan, X.-C. Yang, T. Zhu, and G.-H. Cheng, "Micro Fabry-Perot interferometers in silica fibers machined by femtosecond laser," *Optics Express*, vol. 15, no. 21, p. 14123, 2007, doi: 10.1364/oe.15.014123.

[61] T. Wei, Y. Han, H.-L. Tsai, and H. Xiao, "Miniaturized fiber inline Fabry-Perot interferometer fabricated with a femtosecond laser," *Optics Letters*, vol. 33, no. 6, p. 536, 2008, doi: 10.1364/ol.33.000536.

[62] P. Zhou, C. Liao, Z. Li, S. Liu, and Y. Wang, "In-Fiber Cascaded FPI Fabricated by Chemical-Assisted Femtosecond Laser Micromachining for Micro-Fluidic Sensing Applications," *Journal of Lightwave Technology*, vol. 37, no. 13, pp. 3214–3221, 2019, doi: 10.1109/JLT.2019.2912835.

[63] Z. Wang, F. Shen, L. Song, X. Wang, and A. Wang, "Multiplexed fiber fabry-pérot interferometer sensors based on ultrashort bragg gratings," *IEEE Photonics Technology Letters*, vol. 19, no. 8, pp. 622–624, Apr. 2007, doi: 10.1109/LPT.2007.894361.

[64] Z. Chen, L. Yuan, G. Hefferman, and T. Wei, "Ultraweak intrinsic Fabry–Perot cavity array for distributed sensing," *Optics Letters*, vol. 40, no. 3, p. 320, Feb. 2015, doi: 10.1364/ol.40.000320.

[65] L. Cerami, E. Mazur, S. Nolte, and C. B. Schaffer, "Femtosecond laser micromachining," in *Ultrafast Nonlinear Optics*, Springer International Publishing, 2013, pp. 287–321.

[66] Z. Chen, L. Yuan, G. Hefferman, and T. Wei, "Ultraweak intrinsic Fabry–Perot cavity array for distributed sensing," *Optics Letters*, vol. 40, no. 3, p. 320, 2015, doi: 10.1364/ol.40.000320.

[67] Y. Yang, M. Wang, Q. Yu, and K. P. Chen, "Intrinsic Fabry-Perot Interferometer for Vibration Measurement by Enhanced Rayleigh Backscattering Dots Fabricated by Femtosecond Laser Inscription," 2019, doi: 10.1109/IPCon.2019.8908419.

[68] J. Deng and D. N. Wang, "Construction of cascaded Fabry–Perot interferometers by four in-fiber mirrors for high-temperature sensing," *Optics Letters*, vol. 44, no. 5, p. 1289, 2019, doi: 10.1364/ol.44.001289.

[69] J. Deng, D. N. Wang, and H. Zhang, "Femtosecond Laser Inscribed Multiple In-Fiber Reflection Mirrors for High-Temperature Sensing," *Journal of Lightwave Technology*, vol. 37, no. 21, pp. 5537–5541, 2019, doi: 10.1109/JLT.2019.2935460.

[70] X. L. Cui, H. Zhang, and D. N. Wang, “Parallel structured optical fiber in-line Fabry–Perot interferometers for high temperature sensing,” *Optics Letters*, vol. 45, no. 3, p. 726, 2020, doi: 10.1364/ol.384594.

[71] W. Wang, D. Ding, N. Chen, F. Pang, and T. Wang, “Quasi-distributed IFPI sensing system demultiplexed with FFT-based wavelength tracking method,” *IEEE Sensors Journal*, vol. 12, no. 9, pp. 2875–2880, 2012, doi: 10.1109/JSEN.2012.2204247.

[72] T. Paixão, F. Araújo, and P. Antunes, “Highly sensitive fiber optic temperature and strain sensor based on an intrinsic Fabry–Perot interferometer fabricated by a femtosecond laser,” *Optics Letters*, vol. 44, no. 19, p. 4833, 2019, doi: 10.1364/ol.44.004833.

[73] M. Wang *et al.*, “Multiplexable high-temperature stable and low-loss intrinsic Fabry-Perot in-fiber sensors through nanograting engineering,” *Optics Express*, vol. 28, no. 14, p. 20225, 2020, doi: 10.1364/oe.395382.

[74] R. Cao *et al.*, “Multiplexable intrinsic Fabry-Perot interferometric fiber sensors for multipoint hydrogen gas monitoring,” *Optics Letters*, vol. 45, no. 11, 2020, doi: 10.1364/OL.389433.

[75] S. Richter, M. Heinrich, S. Döring, A. Tünnermann, and S. Nolte, “Formation of femtosecond laser-induced nanogratings at high repetition rates,” *Applied Physics A: Materials Science and Processing*, vol. 104, no. 2, pp. 503–507, 2011, doi: 10.1007/s00339-011-6489-7.

[76] Y. Yang, E. Wang, K. Chen, Z. Yu, and Q. Yu, “Fiber-Optic Fabry-Perot Sensor for Simultaneous Measurement of Tilt Angle and Vibration Acceleration,” *IEEE Sensors Journal*, vol. 19, no. 6, pp. 2162–2169, Mar. 2019, doi: 10.1109/JSEN.2018.2885220.

[77] Y. Yang, M. Wang, Z. Yu, Q. Yu, and K. P. Chen, “Multiplexable intrinsic Fabry – Pé rot interferometer fabricated by femtosecond lasers for dynamic strain and vibration measurements,” 2019.

[78] A. Othonos, “Fiber Bragg gratings,” *Review of Scientific Instruments*, vol. 68, no. 12, pp. 4309–4341, 1997, doi: 10.1063/1.1148392.

[79] Z. Yu and A. Wang, “Fast Demodulation Algorithm for Multiplexed Low-Finesse Fabry-Pérot Interferometers,” *Journal of Lightwave Technology*, vol. 34, no. 3, pp. 1015–1019, Feb. 2016, doi: 10.1109/JLT.2016.2515943.

[80] Z. Yu and A. Wang, “Fast White Light Interferometry Demodulation Algorithm for Low-Finesse Fabry-Pérot Sensors,” *IEEE Photonics Technology Letters*, vol. 27, no. 8, pp. 817–820, Apr. 2015, doi: 10.1109/LPT.2015.2391912.

[81] F. Zimmermann *et al.*, “Femtosecond laser written nanostructures in Ge-doped glasses,” *Optics Letters*, vol. 41, no. 6, p. 1161, 2016, doi: 10.1364/ol.41.001161.

[82] T. Wang, L.-Y. Shao, J. Canning, and K. Cook, “Temperature and strain characterization of regenerated gratings,” *Optics Letters*, vol. 38, no. 3, p. 247, Feb. 2013, doi: 10.1364/ol.38.000247.

[83] R. Chen *et al.*, “Regenerated distributed Bragg reflector fiber lasers for high-temperature operation,” *Optics Letters*, vol. 38, no. 14, p. 2490, Jul. 2013, doi: 10.1364/ol.38.002490.

[84] S. T. Kreger, A. K. Sang, D. K. Gifford, and M. E. Froggatt, “Distributed strain and temperature sensing in plastic optical fiber using Rayleigh scatter,” *Fiber Optic Sensors and Applications VI*, vol. 7316, no. May, p. 73160A, 2009, doi: 10.1117/12.821353.

[85] B. J. Soller, D. K. Gifford, M. S. Wolfe, and M. E. Froggatt, “High resolution optical frequency domain reflectometry for characterization of components and assemblies,” *Optics Express*, vol. 13, no. 2, p. 666, 2005, doi: 10.1364/opex.13.000666.

[86] P. Lu *et al.*, “Distributed optical fiber sensing: Review and perspective,” *Applied Physics Reviews*, vol. 6, no. 4. American Institute of Physics Inc., p. 41302, Dec. 01, 2019, doi: 10.1063/1.5113955.

[87] X. Bao and L. Chen, “Recent Progress in Distributed Fiber Optic Sensors,” *Sensors*, vol. 12, no. 7, pp. 8601–8639, Jun. 2012, doi: 10.3390/s120708601.

[88] M. K. Barnoski, M. D. Rourke, S. M. Jensen, and R. T. Melville, “Optical time domain reflectometer,” *Applied Optics*, vol. 16, no. 9, p. 2375, Sep. 1977, doi: 10.1364/AO.16.002375.

[89] M. Froggatt and J. Moore, “High-spatial-resolution distributed strain measurement in optical fiber with Rayleigh scatter,” *Applied Optics*, vol. 37, no. 10, pp. 1735–1740, Apr. 1998, doi: 10.1364/AO.37.001735.

[90] S. Loranger, M. Gagné, V. Lambin-Iezzi, and R. Kashyap, “Rayleigh scatter based order of magnitude increase in distributed temperature and strain sensing by simple UV exposure of optical fibre,” *Scientific Reports*, vol. 5, no. March, pp. 1–7, 2015, doi: 10.1038/srep11177.

[91] S. Loranger, F. Parent, V. Lambin-Iezzi, and R. Kashyap, “Enhancement of Rayleigh scatter in optical fiber by simple UV treatment: an order of magnitude increase in distributed sensing sensitivity,” *Optical Components and Materials XIII*, vol. 9744, no. March, p. 97440E, 2016, doi: 10.1117/12.2208896.

[92] F. Monet, S. Loranger, V. Lambin-Iezzi, A. Drouin, S. Kadoury, and R. Kashyap, “The ROGUE: a novel, noise-generated random grating,” *Optics Express*, vol. 27, no. 10, p. 13895, 2019, doi: 10.1364/oe.27.013895.

[93] P. Lu, S. J. Mihailov, D. Coulas, H. Ding, and X. Bao, “Low-Loss Random Fiber Gratings Made with an fs-IR Laser for Distributed Fiber Sensing,” *Journal of Lightwave Technology*, vol. 37, no. 18, pp. 4697–4702, 2019, doi: 10.1109/JLT.2019.2917389.

[94] Y. Xu *et al.*, "Optical fiber random grating-based multiparameter sensor," *Optics Letters*, vol. 40, no. 23, p. 5514, 2015, doi: 10.1364/ol.40.005514.

[95] A. Rudenko, J. P. Colombier, and T. E. Itina, "Nanopore-mediated ultrashort laser-induced formation and erasure of volume nanogratings in glass," *Physical Chemistry Chemical Physics*, vol. 20, no. 8, pp. 5887–5899, Feb. 2018, doi: 10.1039/c7cp07603g.

[96] R. Desmarchelier, B. Poumellec, F. Brisset, S. Mazerat, and M. Lancry, "In the Heart of Femtosecond Laser Induced Nanogratings: From Porous Nanoplanes to Form Birefringence," *World Journal of Nano Science and Engineering*, vol. 05, no. 04, pp. 115–125, 2015, doi: 10.4236/wjnse.2015.54014.

[97] A. Yan *et al.*, "Distributed Optical Fiber Sensors with Ultrafast Laser Enhanced Rayleigh Backscattering Profiles for Real-Time Monitoring of Solid Oxide Fuel Cell Operations," *Scientific Reports*, vol. 7, no. 1, pp. 1–9, 2017, doi: 10.1038/s41598-017-09934-3.

[98] P. G. Kazansky *et al.*, "Anomalous anisotropic light scattering in ge-doped silica glass," *Physical Review Letters*, vol. 82, no. 10, pp. 2199–2202, 1999, doi: 10.1103/PhysRevLett.82.2199.

[99] S. M. Eaton *et al.*, "Spectral loss characterization of femtosecond laser written waveguides in glass with application to demultiplexing of 1300 and 1550 nm wavelengths," *Journal of Lightwave Technology*, vol. 27, no. 9, pp. 1079–1085, May 2009, doi: 10.1109/JLT.2008.2005117.

[100] V. A. Amorim, J. M. Maia, D. Viveiros, and P. V. S. Marques, "Loss Mechanisms of Optical Waveguides Inscribed in Fused Silica by Femtosecond Laser Direct Writing," *Journal of Lightwave Technology*, vol. 37, no. 10, pp. 2240–2245, 2019, doi: 10.1109/JLT.2019.2900913.

[101] M. L. Åslund *et al.*, "Optical loss mechanisms in femtosecond laser-written point-by-point fibre Bragg gratings," *Optics Express*, vol. 16, no. 18, p. 14248, 2008, doi: 10.1364/oe.16.014248.

[102] B. J. Soller, D. K. Gifford, M. S. Wolfe, and M. E. Froggatt, "High resolution optical frequency domain reflectometry for characterization of components and assemblies," *Optics Express*, vol. 13, no. 2, p. 666, 2005, doi: 10.1364/opex.13.000666.

[103] M. Wang *et al.*, "Reel-to-Reel Fabrication of In-Fiber Low-Loss and Higherature Stable Rayleigh Scattering Centers for Distributed Sensing," *IEEE Sensors Journal*, vol. 20, no. 19, pp. 11335–11341, 2020, doi: 10.1109/JSEN.2020.2995606.

[104] B. J. Soller, M. Wolfe, and M. E. Froggatt, "Polarization resolved measurement of rayleigh backscatter in fiber-optic components," *Optics InfoBase Conference Papers*, pp. 1–6, 2005.

[105] A. Yan *et al.*, "Distributed Optical Fiber Sensors with Ultrafast Laser Enhanced Rayleigh Backscattering Profiles for Real-Time Monitoring of Solid Oxide Fuel Cell Operations," *Scientific Reports*, vol. 7, no. 1, Dec. 2017, doi: 10.1038/s41598-017-09934-3.

[106] L. A. Fernandes, J. R. Grenier, P. R. Herman, J. S. Aitchison, and P. V. S. Marques, "Stress induced birefringence tuning in femtosecond laser fabricated waveguides in fused silica," *Optics Express*, vol. 20, no. 22, p. 24103, Oct. 2012, doi: 10.1364/oe.20.024103.

[107] L. A. Fernandes, J. R. Grenier, P. V. S. Marques, J. Stewart Aitchison, and P. R. Herman, "Strong birefringence tuning of optical waveguides with femtosecond laser irradiation of bulk fused silica and single mode fibers," *Journal of Lightwave Technology*, vol. 31, no. 22, pp. 3563–3569, 2013, doi: 10.1109/JLT.2013.2284240.

[108] D. K. Gifford, B. J. Soller, M. S. Wolfe, and M. E. Froggatt, "Distributed fiber-optic temperature sensing using Rayleigh backscatter," *IET Conference Publications*, vol. 2005, no. CP502, pp. 511–512, 2005, doi: 10.1049/cp:20050584.

[109] S. T. Kreger, D. K. Gifford, M. E. Froggatt, B. J. Soller, and M. S. Wolfe, "High resolution distributed strain or temperature measurements in single- and multi-mode fiber using swept-wavelength interferometry," *Optics InfoBase Conference Papers*, 2006, doi: 10.1364/ofs.2006.the42.

[110] M. A. S. Zaghloul *et al.*, "Radiation resistant fiber Bragg grating in random air-line fibers for sensing applications in nuclear reactor cores," *Optics Express*, vol. 26, no. 9, p. 11775, Apr. 2018, doi: 10.1364/oe.26.011775.

[111] M. Wang *et al.*, "Reel-to-Reel Fabrication of In-Fiber Low-Loss and Higherature Stable Rayleigh Scattering Centers for Distributed Sensing," *IEEE Sensors Journal*, vol. 20, no. 19, pp. 11335–11341, Oct. 2020, doi: 10.1109/JSEN.2020.2995606.

[112] R. Cao, J. Wu, G. Liang, P. R. Ohodnicki, and K. P. Chen, "Functionalized PdAu Alloy on Nanocones Fabricated on Optical Fibers for Hydrogen Sensing," *IEEE Sensors Journal*, vol. 20, no. 4, pp. 1922–1927, Feb. 2020, doi: 10.1109/JSEN.2019.2950505.

[113] M. A. S. Zaghloul, A. M. Hassan, D. Carpenter, P. Calderoni, J. Daw, and K. P. Chen, "Optical Sensor Behavior Prediction using LSTM Neural Network," *2019 IEEE Photonics Conference, IPC 2019 - Proceedings*, pp. 2019–2020, 2019, doi: 10.1109/IPCon.2019.8908337.

[114] J. Wu *et al.*, "Fabrication of Ultra-Weak Fiber Bragg Grating (UWFBG) in Single-Mode Fibers through Ti-Doped Silica Outer Cladding for Distributed Acoustic Sensing," in *Optics InfoBase Conference Papers*, Jun. 2019, vol. Part F172-ES 2019, p. ETh1A.4, doi: 10.1364/es.2019.eth1a.4.

[115] Q. Guo *et al.*, "Femtosecond laser inscribed sapphire fiber bragg grating for high temperature and strain sensing," *IEEE Transactions on Nanotechnology*, vol. 18, pp. 208–211, 2019, doi: 10.1109/TNANO.2018.2888536.

[116] M. Hörstmann-Jungemann, “Nano- and Microstructuring of SiO2 and Sapphire with Fs-laser Induced Selective Etching,” *Journal of Laser Micro/Nanoengineering*, vol. 4, no. 2, pp. 135–140, 2009, doi: 10.2961/jlmn.2009.02.0011.

[117] Q. K. Li *et al.*, “Sapphire-Based Fresnel Zone Plate Fabricated by Femtosecond Laser Direct Writing and Wet Etching,” *IEEE Photonics Technology Letters*, vol. 28, no. 12, pp. 1290–1293, 2016, doi: 10.1109/LPT.2016.2538270.

[118] B. A. Wilson and T. E. Blue, “Creation of an Internal Cladding in Sapphire Optical Fiber Using the 6Li(n, α)3H Reaction,” *IEEE Sensors Journal*, vol. 17, no. 22, pp. 7433–7439, 2017, doi: 10.1109/JSEN.2017.2756448.

[119] T. Ozawa *et al.*, “Topological photonics,” *Reviews of Modern Physics*, vol. 91, no. 1, 2019, doi: 10.1103/RevModPhys.91.015006.

[120] L. Lu, J. D. Joannopoulos, and M. Soljačić, “Topological photonics,” *Nature Photonics*, vol. 8, no. 11, pp. 821–829, 2014, doi: 10.1038/nphoton.2014.248.

[121] M. C. Rechtsman *et al.*, “Photonic Floquet topological insulators,” *Nature*, vol. 496, no. 7444, pp. 196–200, 2013, doi: 10.1038/nature12066.

[122] S. Mukherjee and M. C. Rechtsman, “Observation of Floquet solitons in a topological bandgap,” *Science*, vol. 368, no. 6493, pp. 856–859, 2020, doi: 10.1126/science.aba8725.

[123] S. Mukherjee *et al.*, “Observation of a Localized Flat-Band State in a Photonic Lieb Lattice,” *Physical Review Letters*, vol. 114, no. 24, pp. 1–5, 2015, doi: 10.1103/PhysRevLett.114.245504.

[124] R. Osellame *et al.*, “Femtosecond writing of active optical waveguides with astigmatically shaped beams,” *Journal of the Optical Society of America B*, vol. 20, no. 7, p. 1559, Jul. 2003, doi: 10.1364/josab.20.001559.

[125] P. S. Salter *et al.*, “Adaptive slit beam shaping for direct laser written waveguides,” *Optics Letters*, vol. 37, no. 4, p. 470, Feb. 2012, doi: 10.1364/ol.37.000470.

[126] M. Ams, G. D. Marshall, D. J. Spence, and M. J. Withford, “Slit beam shaping method for femtosecond laser direct-write fabrication of symmetric waveguides in bulk glasses,” *Optics Express*, vol. 13, no. 15, p. 5676, 2005, doi: 10.1364/opex.13.005676.

[127] W. Yang, C. Corbari, P. G. Kazansky, K. Sakaguchi, and I. C. Carvalho, “Low loss photonic components in high index bismuth borate glass by femtosecond laser direct writing,” *Optics Express*, vol. 16, no. 20, p. 16215, 2008, doi: 10.1364/oe.16.016215.

[128] Y. Nasu, M. Kohtoku, and Y. Hibino, “Low-loss waveguides written with a femtosecond laser for flexible interconnection in a planar light-wave circuit,” *Optics Letters*, vol. 30, no. 7, p. 723, Apr. 2005, doi: 10.1364/ol.30.000723.

[129] S. M. Eaton, M. L. Ng, R. Osellame, and P. R. Herman, "High refractive index contrast in fused silica waveguides by tightly focused, high-repetition rate femtosecond laser," *Journal of Non-Crystalline Solids*, vol. 357, no. 11–13, pp. 2387–2391, 2011, doi: 10.1016/j.jnoncrysol.2010.11.082.

[130] S. Huang, M. Li, K. C.-F. G. E. Thin, and undefined 2017, "Guided-Wave Photonics in Flexible Glass," *Wiley Online Library*, Accessed: Sep. 30, 2020. [Online]. Available: https://onlinelibrary.wiley.com/doi/pdf/10.1002/9781118946404#page=297.

[131] M. Belt, M. L. Davenport, J. E. Bowers, and D. J. Blumenthal, "Ultra-low-loss Ta_2O_5-core/SiO_2-clad planar waveguides on Si substrates," *Optica*, vol. 4, no. 5, p. 532, May 2017, doi: 10.1364/optica.4.000532.

[132] A. Peczek, C. Mai, G. Winzer, and L. Zimmermann, "Comparison of cut-back method and optical backscatter reflectometry for wafer level waveguide characterization," in *IEEE International Conference on Microelectronic Test Structures*, May 2020, vol. 2020-May, doi: 10.1109/ICMTS48187.2020.9107905.

[133] A. Roberts *et al.*, "Refractive-index profiling of optical fibers with axial symmetry by use of quantitative phase microscopy," *Optics Letters*, vol. 27, no. 23, p. 2061, Dec. 2002, doi: 10.1364/ol.27.002061.

[134] A. Jesacher, P. S. Salter, and M. J. Booth, "Refractive index profiling of direct laser written waveguides: tomographic phase imaging," *Optical Materials Express*, vol. 3, no. 9, p. 1223, Sep. 2013, doi: 10.1364/ome.3.001223.

[135] A. Alberucci, C. P. Jisha, and S. Nolte, "Determining the waveguide profile using the overlap integral," Jun. 2019, doi: 10.1109/CLEOE-EQEC.2019.8872199.

[136] S. Nolte, M. Will, J. Burghoff, and A. Tuennermann, "Femtosecond waveguide writing: A new avenue to three-dimensional integrated optics," *Applied Physics A: Materials Science and Processing*, vol. 77, no. 1, pp. 109–111, 2003, doi: 10.1007/s00339-003-2088-6.

[137] P. S. Salter and M. J. Booth, "Adaptive optics in laser processing," *Light: Science and Applications*, vol. 8, no. 1, pp. 1–16, 2019, doi: 10.1038/s41377-019-0215-1.

[138] R. Osellame *et al.*, "Femtosecond laser writing of waveguides in periodically poled lithium niobate preserving the nonlinear coefficient," *Applied Physics Letters*, vol. 90, no. 24, 2007, doi: 10.1063/1.2748328.

[139] J. Noh *et al.*, "Braiding photonic topological zero modes," *Nature Physics*, vol. 16, no. 9, pp. 989–993, 2020, doi: 10.1038/s41567-020-1007-5.

[140] A. Cerjan, S. Huang, M. Wang, K. P. Chen, and M. C. Rechtsman, "Thouless Pumping in Disordered Photonic Systems," *Light: Science & Applications*, p. FM1A.6, 2020, doi: 10.1364/cleo_qels.2020.fm1a.6.

[141] A. Cerjan, M. Wang, S. Huang, K. P. Chen, and M. C. Rechtsman, “Thouless pumping in disordered photonic systems,” *Light: Science and Applications*, vol. 9, no. 1, 2020, doi: 10.1038/s41377-020-00408-2.

[142] W. A. Benalcazar, J. Noh, M. Wang, S. Huang, K. P. Chen, and M. C. Rechtsman, “Higher-order topological pumping,” vol. 1, pp. 1–10, 2020, [Online]. Available: http://arxiv.org/abs/2006.13242.

[143] J. Noh *et al.*, “Topological protection of photonic mid-gap defect modes,” *Nature Photonics*, vol. 12, no. 7, pp. 408–415, 2018, doi: 10.1038/s41566-018-0179-3.

[144] W. A. Benalcazar, J. Noh, M. Wang, S. Huang, K. P. Chen, and M. C. Rechtsman, “Higher-order topological pumping,” Jun. 2020, Accessed: Nov. 05, 2020. [Online]. Available: http://arxiv.org/abs/2006.13242.

[145] C. Jauregui, S. Böhme, G. Wenetiadis, J. Limpert, and A. Tünnermann, “Side-pump combiner for all-fiber monolithic fiber lasers and amplifiers,” *Journal of the Optical Society of America B*, vol. 27, no. 5, p. 1011, May 2010, doi: 10.1364/josab.27.001011.

[146] D. J. Ripin and L. Goldberg, “High efficiency side-coupling of light into optical fibres using imbedded v-grooves,” *Electronics Letters*, vol. 31, no. 25, pp. 2204–2205, Dec. 1995, doi: 10.1049/el:19951429.

[147] Q. Xiao, P. Yan, H. Ren, X. Chen, and M. Gong, “A side-pump coupler with refractive index valley configuration for fiber lasers and amplifiers,” *Journal of Lightwave Technology*, vol. 31, no. 16, pp. 2715–2722, 2013, doi: 10.1109/JLT.2013.2271910.